HELICOPTER AUTONOMOUS SHIP LANDING SYSTEM

A Thesis

by

BOCHAN LEE

Submitted to the Office of Graduate and Professional Studies of
Texas A&M University
in partial fulfillment of the requirements for the degree of

MASTER OF SCIENCE

Chair of Committee,	Moble Benedict
Committee Members,	John Valasek
	Sivakumar Rathinam
Head of Department,	Rodney Bowersox

August 2018

Major Subject: Aerospace Engineering

ABSTRACT

This research focuses on developing a helicopter autonomous ship landing algorithm based on the real helicopter ship landing procedure which is already proven and currently used by Navy pilots. It encompasses the entire ship landing procedure from approach to landing using a pilot-inspired vision-based navigation system. The present thesis focuses on the first step towards achieving this overarching objective, which involves modeling the flight dynamics and control of a helicopter and some preliminary simulations of a UH-60 (Blackhawk) helicopter landing on a ship.

The airframe of the helicopter is modeled as a rigid body along with rotating articulated blades that can undergo flap, lag and pitch motions about the root. A UH-60 helicopter is used for a representative model due to its ample simulation and flight test data. Modeling a UH-60 helicopter is based on Blade Element Momentum Theory (BEMT), rotor aerodynamics with the Pitt-Peters linear inflow model, empennage aerodynamics and rigid body dynamics for fuselage. For the blade dynamics, the cyclic (1/rev) and collective pitch motions are prescribed and the blade (1/rev) flap and lag motions are obtained as a response to the aerodynamic and inertial forces. The helicopter control inputs and translational and attitude dynamics obtained from the model are validated with flight test data at various speeds and attitude.

A linearized model is extracted based on a first-order Taylor series expansion of the nonlinear system about an equilibrium point for the purpose of determining the stability of the dynamic system, investigating sensitivity to gusts, and designing a model-based flight control system. Combined vision-based navigation and Linear Quadratic Regulator (LQR) for set-point tracking is used for disturbance rejection and tracking states. A rotatable camera is used for identifying the relative position of the helicopter with respect to the ship. Based on the position, a corresponding trajectory is computed. Considering the trade-off between transient responses and control efforts, gains for the LQR controller are chosen carefully and realistically.

A fully autonomous flight is simulated from approach to landing on a ship. It consists of initial

descent, steady forward flight, steady coordinated turn, deceleration, and final landing. Corresponding to the each maneuver, relevant linearized model is used and gains are tuned. By using X-plane flight simulator program, the simulation data which include fuselage attitude and position at each time step are visualized with a single flight deck ship.

This method allows an aircraft to land on a ship autonomously while maintaining high level of safety and accuracy without the need to capture the ship deck motions, however, by using a camera, and any other additional sensors, which will provide the accurate location of the ship relative to the helicopter. This method is not only relevant for a particular helicopter, but for any types of VTOL aircraft, manned or unmanned. Hence, it can improve the level of safety by preventing human errors that may occur during landing on a ship.

DEDICATION

To my parents Byungkyun Lee and Okhwa Lee, for giving me wings,

and to my wife Sunhye Lee and my little one Jaeho Lee, for flying with me.

ACKNOWLEDGMENTS

First and foremost, I owe a large debt of gratitude to Dr. Moble Benedict. Without his careful guidance and supervision, development of the system presented in this thesis would have been nearly impossible. Every time I lost the way to go, he always shed light on the path to follow. He always listened to my opinions with open mind and shared great insights with me. Every moment I spent with him was a great pleasure and made me open eyes to the new world.

I also would like to express my sincere gratitude to Dr. Ananth Sridharan at the University of Maryland for the guidance and support in modeling and control system design. He always answered my questions and his feedback played an important role in my work. I am also thankful to my committee members, Dr. John Valasek and Dr. Sivakumar Rathinam, for giving me precious feedback and showing me visions.

I am also grateful to all the friends that I met here at Texas A&M University, Vinicius Goecks, Niladri Das, Roshan Suresh, Kookjin Sung, Utkarsh Mishra, Sunsoo Kim, and Dipanjan Saha for their help and sharing ideas.

I owe my deepest thanks to my family - my father, Byungkyun Lee, my mother, Okhwa Lee, and my sister Younhye Lee, who have always stood by me and supported me through my career. My wife, Sunhye Lee has sacrificed many things in her life and beared with my busy life. I promise that I will pay back my debts in the rest of life. My little one, Jaeho Lee is my reason for life. He motivated me to become a father he can be proud of. I always love you as you are.

It is impossible to remember all, and I apologize to those I have inadvertently left out.

CONTRIBUTORS AND FUNDING SOURCES

Contributors

This work was supported by a thesis committee consisting of Professor Moble Benedict and John Valasek of the Department of Aerospace Engineering and Professor Sivakumar Rathinam of the Department of Mechanical Engineering. Also, Dr. Ananth Sridharan at the University of Maryland gave guidance for the mathematical modeling of a UH-60 helicopter.

All work for the dissertation was completed independently by the student.

Funding Sources

Graduate study was supported by a fellowship from Republic of Korea Navy and a thesis research scholarship from Vertical Flight Foundation.

NOMENCLATURE

a	Lift-curve slope
A	Acceleration vector
A	State matrix
B	Control matrix
c	Blade section chord length
c_l, c_d, c_m	Blade section lift, drag and pitching moment coefficients
E	Young's Modulus, acceleration coupling matrix
e	Hinge offset of main rotor blade
g	Acceleration due to gravity
G	Shear modulus
H	Hermite interpolation polynomials
i_B, j_B, k_B	Unit vectors of body-fixed frame
i_F, j_F, k_F	Unit vectors of blade flapped frame
i_G, j_G, k_G	Unit vectors of earth-fixed frame
i_{NR}, j_{NR}, k_{NR}	Unit vectors of blade non-rotating frame
i_R, j_R, k_R	Unit vectors of blade rotating frame
i_L, j_L, k_L	Unit vectors of blade lagged frame
i_{TPP}, j_{TPP}, k_{TPP}	Unit vectors of Tip path plane frame
I_b	Mass flapping moment of inertia
I_{xx}, I_{yy}, I_{zz}	Aircraft mass moments of inertia about body axes
I_{xy}, I_{xz}, I_{yz}	Aircraft products of inertia
K	Linear portion of stiffness matrix
L, M, N	Components of total applied moments about body axes

m_b	Blade mass per unit length
M	Linear portion of mass matrix
N_b	Number of blades
p	Roll rate of aircraft
q	Pitch rate of aircraft, Dynamic pressure
r	Yaw rate of aircraft
R	Main rotor radius, Position vector
t	Time (sec)
T_{BG}	Transformation matrix from earth-fixed frame to body-fixed frame
T_{GB}	Transformation matrix from body-fixed frame to earth-fixed frame
T_{NB}	Transformation matrix from body-fixed frame to blade non-rotating frame
T_{RN}	Transformation matrix from blade non-rotating frame to blade rotating frame
T_{FR}	Transformation matrix from blade rotating frame to blade flapped frame
T_{LF}	Transformation matrix from blade flapped frame to blade lagged frame
T_{TN}	Transformation matrix from blade non-rotating frame to tip path plane frame
u	Forward speed of the aircraft, Control vector
v	Lateral speed of the aircraft
V	Velocity vector
w	Vertical speed of the aircraft, angular rates vector
X, Y, Z	Components of total applied forces along body axes
x	Trim vector

y	State vector
α_F	Aircraft angle of attack
α_s	Longitudinal shaft tilt angle
β_F	Fuselage sideslip angle
β_S	Lateral shaft tilt angle
β_o	Blade coning angle
β_{1c}, β_{1s}	Longitudinal and lateral blade flapping coefficient
Λ	Tail rotor cant angle
γ	Flight path angle
ζ_o	Blade mean lagging angle
ζ_{1c}, ζ_{1s}	Longitudinal and lateral blade lagging coefficient
θ	Aircraft pitch attitude Euler angle, blade pitch angles associated with geometric rotation
θ_o, θ_{1c}, θ_{1s}, θ_{TR}	Collective, lateral, longitudinal cyclic, and tail rotor control stick angle
θ_{tw}	Built-in blade twist
λ_o, λ_{1c}, λ_{1s}	Steady, cosine and sine portions of main rotor inflow
λ_{tr}	Tail rotor inflow
μ	Main rotor advance ratio
ρ	Air density
ϕ	Aircraft roll attitude Euler angle
ϕ_F	Fuselage roll angle
χ	Wake skew angle
	Aircraft yaw attitude Euler angle, blade azimuth angle
Ω	Main rotor speed
BEMT	Blade Element Momentum Theory

DGPS	Differential Global Positioning System
FAA	Federal Aviation Administration
FDR	Flight Data Recorder
FHD	Full High Definition
GPS	Global Positioning System
HAFOV	Horizontal Angular Field of View
HOSTAC	Helicopter Operations from Ships other Than Aircraft Carriers
IR	Infrared Radiation
JPALS	Joint Precision Approach and Landing System
LQR	Linear Quadratic Regulator
LTI	Linear Time Invariant
MAP	Missed Approach Point
NATO	North Atlantic Treaty Organization
ODE	Ordinary Differential Equation
PDE	Partial Differential Equation
RGB	Red, Green, Blue
TPP	Tip Path Plane
UAV	Unmanned Aerial Vehicle
VAFOV	Vertical Angular Field of View
VTOL	Vertical Takeoff and Landing

TABLE OF CONTENTS

Page

LIST OF FIGURES

FIGURE Page

LIST OF TABLES

TABLE Page

1. INTRODUCTION

1.1 MOTIVATION

During my 7 years of experience as a Navy UH-60 helicopter pilot, I have occasionally heard of or witnessed a number of aircraft accidents including UAVs. Naturally, I have always been thinking how to reduce the number of aircraft accidents and what needs to be done for enhancing the level of aviation safety.

Many accidents are occurred while attempting to land on a ship. Fundamentally, Landing on a ship is a highly demanding job mainly due to ship motions, and limited space. It is even more difficult to conduct ship landings under severe weather conditions or at night.

In particular, according to FAA unmanned aircraft accident/incident data, a list of 239 U.S. Navy unmanned aircraft Pioneer accidents was categorized into principle causes. 68 accidents out of 239 were caused by human factors and the largest percentage(68%) of them was occurred while landing on a ship.

It convinces me that landing on a ship for UAVs has to be done autonomously rather than remotely controlled and it can also be work as a backup system for conventional helicopters to improve its safety level significantly.

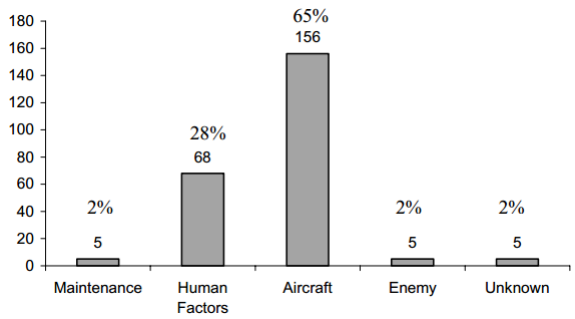

Figure 1.1: U.S. Navy Pioneer UA accident causal factors [35]

Issue	Number	Percent
Aircrew Coordination	9	13%
Landing Error	46	68%
Take-off Error	7	10%
Weather	6	9%

Table 1.1: Breakdown of human factors issues for Pioneer accidents [35]

1.2 HELICOPTER SHIP LANDING

Landing on a ship is one of the most demanding tasks for a Navy pilot due to many factors such as ship motions, limited space, less visual references for pilots, lack of alternative landing spots, and so on. In order to prevent spatial disorientation, a pilot only refers to the horizon bar to maintain desired attitude during landing on a ship. A gyro-stabilized horizon bar is the only reliable reference object since it does not move depending on ship motions, but always maintains horizontal position.

There are three mandatory equipment which are deck status lights, overhead floodlights, and horizon bar. They are regulated by Helicopter Operations from Ships other Than Aircraft Carriers (HOSTAC). HOSTAC is a military international standardization program between over 50 navies and coast guards to conduct ship landing operations safely. Each participant registers up-to-date deck information and approach procedure charts. Individual ship has its own chart, but they have key things in common such as an approaching course is set within the range of 30 degrees from a ship sailing upwind and a missed approach point is approximately at 0.5 nm from a ship. It also specifies the relative distance and altitude at initial approach point (IAP), final approach point (FAP), and missed approach point (MAP). Once a pilot fails in identifying a ship visually at the missed approach point, it is required to abort landing and commence missed approach procedures.

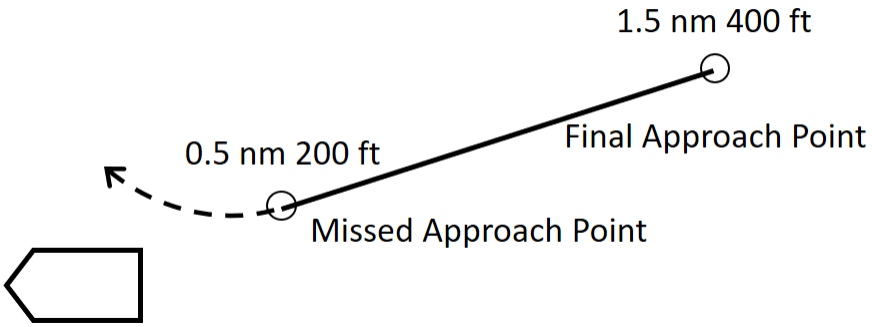

Figure 1.2: Example Ship Approach Chart

1.3 LITERATURE SURVEY

This section presents a survey of several publications that are relevant to the current study. There has been studies regarding shipboard UAV autonomous landing system and developed mostly in two ways. One is to utilize more advanced GPS system for precise guidance, and the other is to apply vision-based navigation system. However, approaches using GPS are not feasible in GPS-denied environment. Although the other approaches using vision-based navigation are effective in GPS-denied environment, their application associated with a camera raises an issue to track ship motions accurately which is highly uncertain and complicated due to sea states and ship maneuvers. Inevitably, it leads to utilize a large array of powerful sensors and complex algorithms to capture motions of the ship deck.

1.3.1 GPS-BASED SHIP LANDING

There has been studies which aims to make ship landings by using GPS signals. Since the altitude measurement from the GPS is not accurate, so additional sensors such as a radar altimeter or a barometric pressure sensor are also used in conjunction with GPS. Typically, combined GPS and Inertial Navigation Sensors (INS) systems are suitable for long range and low precision flights, however, not suitable for precise and close proximity flights. Thus, this method is being developed to integrate these systems for better accuracy and reliability.

Category	Mode	Horizontal Accuracy
Stand-Alone	Civilian receiver, SA on (historical)	100 m
Stand-Alone	Civilian receiver, SA off (current)	5 - 8 m
Stand-Alone	Military receiver, (dual frequency)	3 - 5 m
Differential	Code differential	1 - 3 m
Differential	Carrier-smoothed code differential	0.1 - 1 m
Differential	Precise carrier-phase (kinematic)	1 - 2 cm
Differential	Precise carrier-phase	1 - 2 mm

Table 1.2: Typical GPS Accuracy [6]

Particularly, Conducting a ship landing based on Joint Precision Approach and Landing System (JPALS) has been developed by the Department of the Navy [2], Jason Rife [3], Greg Johnson [1], and Boris Pervan et. al.[5] Briefly introducing a JPALS, for making an approach and landing on a ship, it is required to know the orientation of the landing spot with respect to the earth-fixed frame so it can command its own attitude to the same orientation. In addition, since the GPS sensors are not located on the landing spot, it has to relocate the GPS measurements to the exact landing point, which requires a precise knowledge of the vector from the GPS sensor location on a ship to the center of the landing point. Unique to the ship landing is the fact that the flight deck is constantly changing its orientation with respect to the earth-fixed frame. This increases uncertainty or error into the guidance quality of the ship landing operations, where clearly the operational restrictions apply more than land operations. Thus, Placing the GPS sensors in relative locations so that all three rotation axes have observability and that they are placed far apart on a ship can greatly increase the accuracy. It can determine an accurate path for the aircraft to approach and land. This method can be used in zero-visibility conditions and has good precision in approach and landing. However, it is developed for aircraft carrier, which has larger deck, and requires multiple GPS antennas on a ship. Also, it needs to be reprogrammed for a designated ship due to the GPS antenna placement. Above all, it cannot be used when the GPS signals are lost.

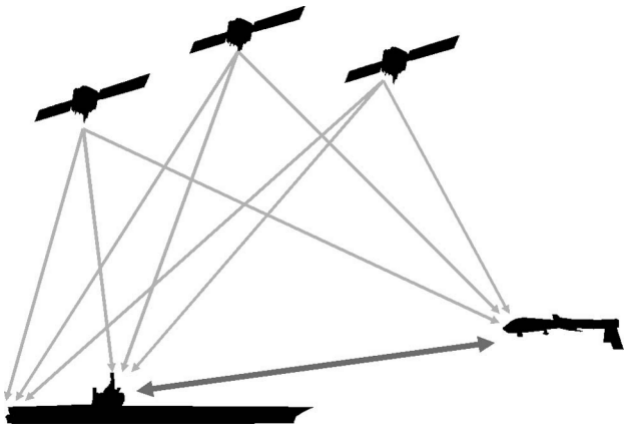

Figure 1.3: JPALS navigation signals include GPS broadcasts and a ship-based communication link [3]

In the case of conducting a ship landing on a small flight deck by using GPS, there are also relevant studies and experiments. In 2012, research conducted by Mark Hardesty [7] demonstrates the flight tests of an autonomous landing on a moving platform. This application requires continuously precise and accurate relative positioning of the helicopter and the ship. Real time kinematic (RTK) algorithms solve for the relative position vector from the base to the rover receiver on a helicopter. By using this method, relative position can be computed precisely because the distance between the base and rover is short. However, it requires constant communication between the rover and the base, as well as maintaining enough common satellites during the landing maneuvers as the helicopter approaches the ship deck. In addition, related works which utilize GPS can be categorized based on a controller and an aircraft.

Ref.	Controller	Aircraft	System Details
[13], [14]	PID [13], PD with fuzzy logic [14]	VTOL	6 DOF simulations Pitch, roll and altitude control
[15], [16] [17]	Nonlinear Feedback Linearization	Fixed Wing [15], [17], VTOL [16]	3 DOF aircraft model Ground effect
[18]	Sliding Mode Control	Fixed Wing	6 DOF Nonlinear Model Comparison with PID controller Lyapunov stability criteria
[16], [20] [21]	Backstepping and Neural Networks	Fixed Wing [16], VTOL [20], [21]	6 DOF Model Flapping correction and servo dynamics
[22]	Hybrid Control	General UAV	Landing as a sequence of tasks Switching strategy between controllers Design correctness analyzed by a reachability computation

Table 1.3: Comparison of landing methods using GPS [33]

Consequently, These approaches require a high accuracy of GPS for guiding an aircraft to a landing spot and they have been developed by advancing GPS utilization. Nevertheless, Its applications are not able to be extended to the GPS-denied environment.

1.3.2 VISION-BASED SHIP LANDING

Vision-based ship landing system is particular point of interest in this research. Computer vision is used in the feedback control loop of an autonomous landing system. It is suitable for particular problems where the landing spot is in a random location or moving (the deck of a ship). There have been many studies regarding the vision-based control techniques for detection, tracking and landing.

Daquan and Hongyue [31] proposed a vision-based navigation algorithm using extended Kalman filter (EKF) to estimate the attitude of an aircraft. This method uses parameters such as image gradients of centerline and threshold bar of runway lighting, longitudinal and lateral mean of the image coordinates of observed airport lights. Even if its method is designed for landing on a runway, it offers possible ideas can be applied to ship landing.

G. Xu, Y. Zhang et al.[12] proposed a method to detect an object by using infrared images. Hence, based on the temperature difference between the target and background, it detects the target object. In order to detect the object, a high emissivity black powder is spread on the object. It shows the utilization of infrared images which is in effective especially at night, however, it can be used only in the proximity of a ship since it captures the "T" mark on a landing spot.

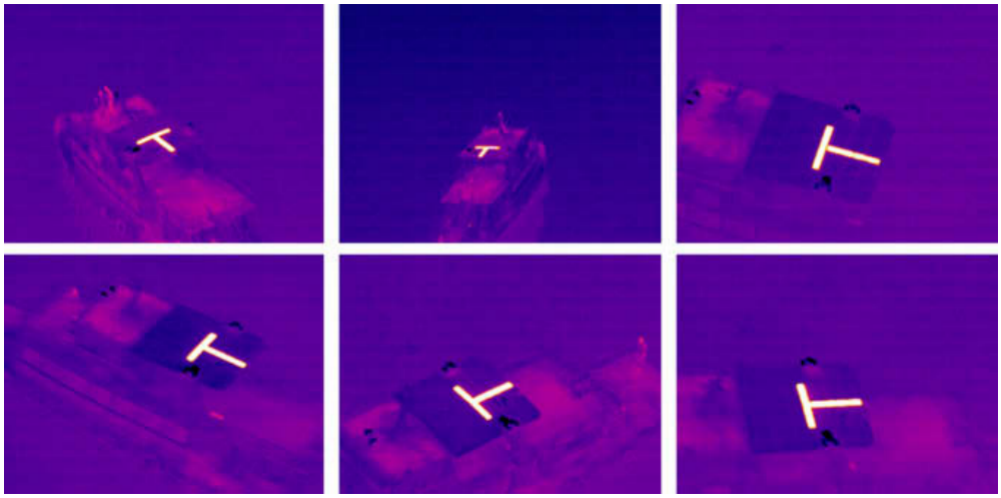

Figure 1.4: Infrared images of the cooperative object [12]

Sereewattana and Ruchanurucks [30] proposed depth estimation of markers for landing control by using a single camera. It is used to capture two consecutive ground images to simulate a pair of images. The markers, which are composed of four circles in different colors, are used to estimate the relative distance between the UAV and the markers. However, the accuracy is not considered high and it can be applied only to vertical landing part.

Miller et al. [32] proposed a method to land using image registration. They used information about the terrain surrounding the runway from different scales and distances instead of the visual features of the runway itself. Geometric features are obtained which are approximately linear indicators of the quantities to be measured. The course deviation of the UAV can be estimated from the camera model and registered image is used as an input to a linear feedback control loop. Even if it is developed for landing on a runway, the process of measuring the geometric properties from the image can be applied to the ship landing.

In addition, related works which utilize vision-based can be categorized as below.

Ref.	Aircraft	Equipment	Details
[23], [24]	VTOL VTOL	Downward CCD camera Ultrasonic sonar and INS	Invariant moments Kalman filter based tracking
[25], [26]	MAV [25], VTOL [26]	Optic flow sensor IMU, GPS Barometric pressure sensor	Optic flow and barometric altimeter based HAG estimation
[27]	VTOL	CCD Camera mounted on a PTU Accelerometer and angular rate gyros	Contour extraction Kalman filter fusion
[28]	Not specified	Treatment on an object Infrared thermal imager GPS and INS	Recognition from infrared images Affine moment invariants
[29], [30], [31]	Not specified	Two Cameras	Monocular, stereo, machine vision EKF, Hough transform Vanishing geometry RANSAC algorithm

Table 1.4: Comparison of Vision-based landing methods [33]

Although there are the decent amount of related works, they are independently developed from the actual helicopter ship landing procedure. In these previous studies, a camera is used in common for capturing markings on a ship deck in the most cases. Based on the information obtained from a camera, an aircraft determines its attitude and conduct a ship landing. This process requires high precision of camera and complex algorithms due to the uncertainty of ship motions. Taking into account real helicopter ship landing procedure, it is developed in exactly the opposite direction because helicopter pilots are trained not to refer to the ship motions but the horizon bar instead. In addition, tracking markings on a ship deck with a downward looking camera can only cover the vertical landing part. It implies it needs different approach to this matter.

1.4 OBJECTIVES OF THE RESEARCH

This research develops a novel vision-based autonomous ship landing system based on the actual helicopter ship landing procedure. Unlike the previous vision-based approaches which capture and track a mark on a flight deck, the proposed approach utilizes a gyro-stabilized horizon reference bar which is already equipped in most modern navy ships (mandatory equipment regulated by NATO). By using the bar, which can easily be seen from the direction of approaching and always maintains the horizon regardless of ship motions, it can cover the whole flight maneuvers from approach to land on a ship. Also, it has relatively simple algorithm as well as maintaining the high level of safety since it does not require to consider ship motions. The range of applications is not limited to one particular ship. This method can be applied for most navy, coast guard, and government ships which follows NATO regulations. Hence, this research is conducted with the following objectives :

- Mathematically modeling and Validating a UH-60 helicopter
- Develop an autonomous ship landing system covers completely from MAP to landing
- Develop an autonomous ship landing system fully operational in GPS-denied environments
- Design a robust control system which can track a desired trajectory realistically

- Simulate and Visualize the entire flight done by the proposed ship landing system

In chapter 2, the methodology of building a UH-60 helicopter mathematical model is described. Coordinate systems, governing equations, the helicopter dynamics and aerodynamics are included. In chapter 3, it shows the trim calculation of the helicopter and comparison with flight test data. Also, it includes the linearized model extraction method. In chapter 4, vision-based algorithm and LQR control design method are explained. Corresponding simulation and visualization results are also presented. In chapter 5, the summary and conclusion of the work is outlined. It discusses the key lessons learned and further study.

2. MATHEMATICAL MODEL

The purpose of this chapter is to describe explicitly the methodology of building a UH-60 helicopter mathematical model. It is composed of coordinate systems, helicopter dynamics and aerodynamics which consist of subsections such as a main rotor, tail rotor, and empennage. The first section explains the governing equations of the system in state-space form. The second section includes coordinate systems which are used in this study. The last section describes force and moment contributions from the components of the helicopter.

2.1 GOVERNING EQUATIONS

The governing equations of the system are formulated in state-space form as a system of first-order nonlinear coupled ODEs :

$$f(y, \dot{y}, u, t) = \epsilon = 0 \tag{2.1}$$

y is a vector of system states, $\dot{y}$ is time derivatives of *y*, *u* is a vector of control inputs, and t is the current time in seconds. Numerical solutions of these equations with zero body-axis accelerations for trim are used to study vehicle performance in steady flight. The state vector consists of the following components

$$y \quad = \quad \{ \quad y_F^T \quad y_\lambda^T \quad y_{rotor}^T \quad \}^T \tag{2.2}$$

- y_F represents the vector of the 9 airframe rigid-body states
- y_λ represents the induced inflow coefficients for main rotor and tail rotor
- y_{rotor} represents the vector of rotor deflection states for all blades

$$u \quad = \quad \{ \quad \delta_o \quad \delta_{lat} \quad \delta_{lon} \quad \delta_{ped} \quad \}^T \tag{2.3}$$

The controls are manipulable by the helicopter pilot and represent, in order, the positions of the collective lever, lateral and longitudinal cyclic stick, and the foot pedal.

2.2 COORDINATE SYSTEMS

Various reference frames are used in dynamic simulations, depending on the component being analyzed. Earth-fixed axes to track a trajectory in inertial frame, body axes for force and moment equilibrium equations, hub-fixed axes for hub loads and rotating axes for blade deflections are some examples. Displacements and loads must be transferred from one axis system to another through coordinate transformations to use in the governing equations for each component. Mathematically, this rotation can be expressed as the pre-multiplication of a vector (X, Y, Z components) with a rotation matrix. A rotation from one coordinate system to another is performed in "3(ψ) - 2(θ) - 1(ϕ)" Euler angle sequence. The rotations are positive in the anti-clockwise sense. Although it has a singularity at a rotation angle of $\pm 90^{\circ}$, this does not happen in general helicopter maneuver. The rotation matrices for the yaw, pitch and roll rotations are given below.

$$T_{\psi} = \begin{bmatrix} \cos\psi & \sin\psi & 0 \\ -\sin\psi & \cos\psi & 0 \\ 0 & 0 & 1 \end{bmatrix}$$

$$T_{\theta} = \begin{bmatrix} \cos\theta & 0 & -\sin\theta \\ 0 & 1 & 0 \\ \sin\theta & 0 & \cos\theta \end{bmatrix}$$

$$T_{\phi} = \begin{bmatrix} 1 & 0 & 0 \\ 0 & \cos\phi & \sin\phi \\ 0 & -\sin\phi & \cos\phi \end{bmatrix}$$

Since the sequence occurs in the order Z $\rightarrow$ Y $\rightarrow$ X, the rotation matrices must be premultiplied in this order. Thus, the final rotation matrix from the earth-fixed coordinate system "G" to the

body-fixed coordinate system "B" through angles (ψ,θ,ϕ) is

$$T_{BG} \quad = \quad T_\phi \ T_\theta \ T_\psi \quad = \quad R(\psi, \theta, \phi)$$

The subscript "BG" means transformation from ground(earth-fixed inertial frame) to body-fixed frame. The reverse rotation from frame "B" to "G" follows the exact opposite sequence in reverse, i.e. angles ($-\psi$,$-\theta$,$-\phi$) about the (X,Y,Z) axes. In this case, the rotation matrix is given by

$$T_{GB} \quad = \quad T_{-\phi} \ T_{-\theta} \ T_{-\psi}$$

The rotation from "B" to "G" can be simplified to

$$T_{GB} \quad = \quad T_\phi^T \ T_\theta^T \ T_\psi^T$$

Using the matrix property

$$T_{GB} \quad = \quad (T_\phi \ T_\theta \ T_\psi)^T \quad = \quad T_{BG}^T$$

2.2.1 EARTH-FIXED FRAME

The earth-fixed axes coordinates represent an inertial reference system used to track the motion of objects in space. The origin of this axis system is a fixed point on the ground. The unit vectors along the earth-fixed axes are represented by (i_G, j_G, k_G). The earth-fixed axes are oriented so that i_G points North, j_G points East and k_G points towards the ground. The position vector of the helicopter CG in space is given by

$$r_{CG} \quad = \quad x_{CG}\, i_G \quad + \quad y_{CG}\, j_G \quad + \quad z_{CG}\, k_G \tag{2.4}$$

2.2.2 HELICOPTER BODY-FIXED FRAME

The body axes of the helicopter, shown in Fig. 2.1, are obtained from the earth-fixed coordinates using three transformation to shift the origin to the helicopter center of gravity, followed by "3(ψ) - 2(θ) - 1(ϕ)" Euler angle rotations. It is positive for nose-right, pitch-up and roll-right motions respectively. The unit vectors along the body axes are calculated by

$$\begin{bmatrix} i_B \\ j_B \\ k_B \end{bmatrix} = T_{BG} \begin{bmatrix} i_G \\ j_G \\ k_G \end{bmatrix} \tag{2.5}$$

The rotation matrix from inertial to helicopter body axes is given by

$$T_{BG} = \begin{bmatrix} 1 & 0 & 0 \\ 0 & \cos\phi_F & \sin\phi_F \\ 0 & 0 & 0 \end{bmatrix} \begin{bmatrix} \cos\theta_F & 0 & -\sin\theta_F \\ 0 & 1 & 0 \\ \sin\theta_F & 0 & \cos\theta_F \end{bmatrix} \begin{bmatrix} \cos\psi_F & \sin\psi_F & 0 \\ -\sin\psi_F & \cos\psi_F & 0 \\ 0 & 0 & 1 \end{bmatrix}$$

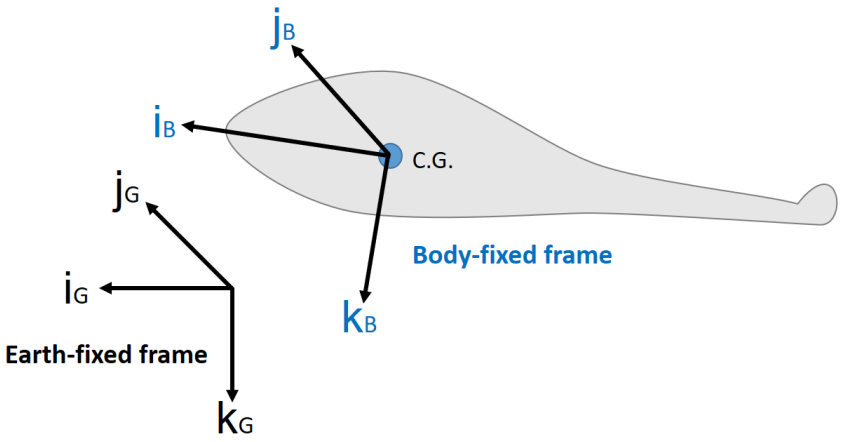

Figure 2.1: Earth-fixed frame and helicopter body-fixed frame

2.2.3 BLADE NON-ROTATING FRAME

The blade non-rotating axes, shown in Fig. 2.2, is transformed from the helicopter body frame, followed by two Euler rotations α_s which is a shaft longitudinal tilt angle, β_s which is a shaft lateral tilt angle in the order Y $\rightarrow$ X, followed by a 180° rotation about the intermediate Y-axis. The first two rotations are positive when the shaft tilt causes the hub to move aft and starboard, respectively. The new origin of this axis system is at the center of the hub. In case of UH-60, the shaft tilts 3° forward and has no lateral tilt angle. The unit vectors along the blade non-rotating frame are

$$\begin{bmatrix} i_{NR} \\ j_{NR} \\ k_{NR} \end{bmatrix} = T_{NB} \begin{bmatrix} i_B \\ j_B \\ k_B \end{bmatrix} \tag{2.6}$$

The rotation matrix from the helicopter body frame to the blade non-rotating frame is

$$T_{NB} = \begin{bmatrix} -1 & 0 & 0 \\ 0 & 1 & 0 \\ 0 & 0 & -1 \end{bmatrix} \begin{bmatrix} 1 & 0 & 0 \\ 0 & \cos\beta_s & \sin\beta_s \\ 0 & -\sin\beta_s & \cos\beta_s \end{bmatrix} \begin{bmatrix} \cos\alpha_s & 0 & -\sin\alpha_s \\ 0 & 1 & 0 \\ \sin\alpha_s & 0 & \cos\alpha_s \end{bmatrix}$$

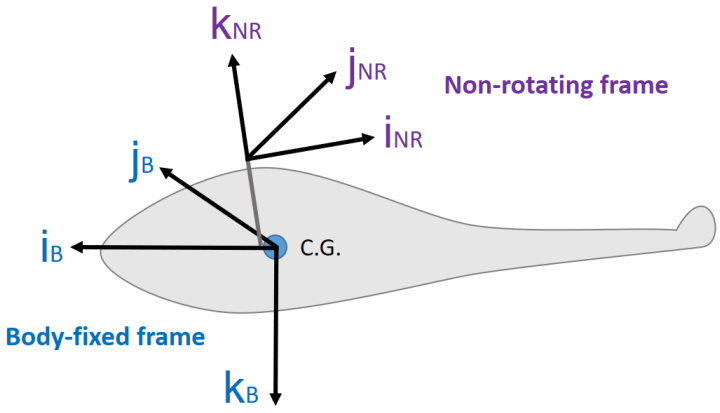

Figure 2.2: Blade non-rotating frame

2.2.4 BLADE ROTATING FRAME

The blade rotating frame, shown in Fig. 2.3, is obtained from the blade non-rotating frame using one rotation ψ_n about the blade non-rotating Z-axis k_H. The origin of the blade rotating frame is at the center of the hub which is identical to the origin of the blade non-rotating frame. The ψ_n is the azimuth angle of the n^{th} blade, zero when the blade passes over the tail boom, positive in counter-clockwise direction and is given by $\psi_n = \Omega_{MR}\, t + \frac{2\pi}{N_b}(n - 1)$. The unit vectors along the blade rotating frame are given by

$$\begin{bmatrix} i_R \\ j_R \\ k_R \end{bmatrix} = T_{RN} \begin{bmatrix} i_{NR} \\ j_{NR} \\ k_{NR} \end{bmatrix} \tag{2.7}$$

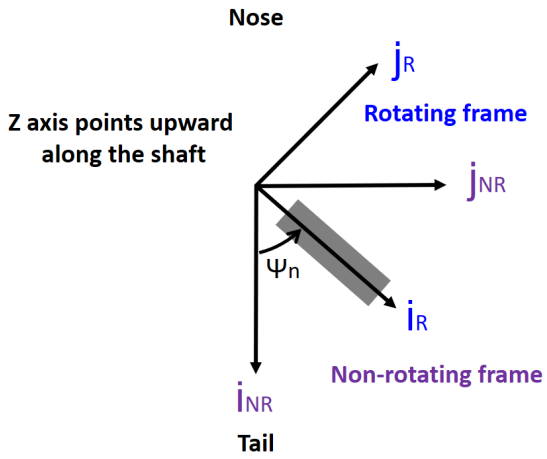

Figure 2.3: Blade rotating frame

The rotation matrix from the blade non-rotating frame to the blade rotating frame is

$$T_{RN} = \begin{bmatrix} \cos\psi_n & \sin\psi_n & 0 \\ -\sin\psi_n & \cos\psi_n & 0 \\ 0 & 0 & 1 \end{bmatrix}$$

2.2.5 BLADE FLAPPED FRAME

The blade flapped frame, shown in Fig.2.4, is obtained from the blade rotating frame using one rotation through an angle -β_n about the j_R blade rotating axis, and is positive for vertically upward motion of the blade tip. The value of an angle β_n depends on the azimuthal location of the n^{th} blade. The origin of the blade flapped frame is identical to the origin of the blade rotating frame. The unit vectors along the blade flapped frame are given by

$$\begin{bmatrix} i_F \\ j_F \\ k_F \end{bmatrix} = T_{FR} \begin{bmatrix} i_R \\ j_R \\ k_R \end{bmatrix} \tag{2.8}$$

The rotation matrix from the blade rotating axes to the blade flapped axes is given by

$$T_{FR} = \begin{bmatrix} \cos\beta_n & 0 & \sin\beta_n \\ 0 & 1 & 0 \\ -\sin\beta_n & 0 & \cos\beta_n \end{bmatrix}$$

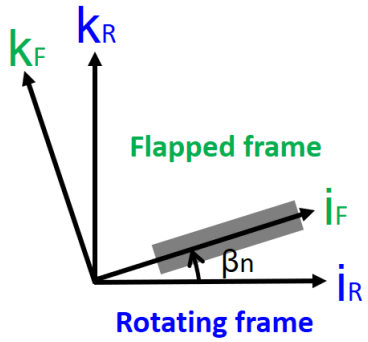

Figure 2.4: Blade flapped frame

2.2.6 BLADE LAGGED FRAME

The blade lagged frame, shown in Fig.2.5, is obtained from the blade flapped frame using one rotation through an angle -ζ_n about the k_F blade flapped frame, and is positive for horizontally forward (lead) motion of the counter-clockwise rotating n^{th} blade tip. The origin of the blade lagged frame is identical to the origin of the blade flapped frame. The unit vectors along the blade lagged frame are given by

$$\begin{bmatrix} i_L \\ j_L \\ k_L \end{bmatrix} = T_{LF} \begin{bmatrix} i_F \\ j_F \\ k_F \end{bmatrix} \tag{2.9}$$

The rotation matrix from the blade flapped frame to the blade lagged frame is given by

$$T_{LF} = \begin{bmatrix} \cos\zeta_n & -\sin\zeta_n & 0 \\ \sin\zeta_n & \cos\zeta_n & 0 \\ 0 & 0 & 1 \end{bmatrix}$$

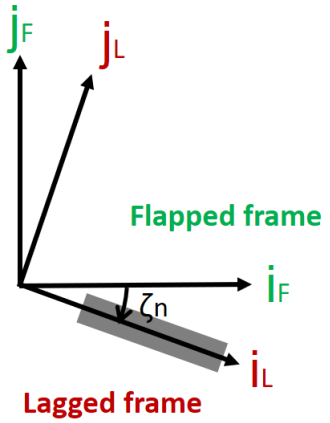

Figure 2.5: Blade lagged frame

2.2.7 TIP PATH PLANE

It is convenient to define Tip Path Plane (TPP) since the incoming airflow is perpendicular to TPP. The tip path plane is the plane that contains the path described by the blade tips, assuming that the blade motion is first harmonic only (1/rev). An observer on the tip path plane will see only the coning angle β_o. Hence, the rotor blade flapping is not a function of blade azimuth if it is defined with respect to the TPP. However, the blade pitch angle θ will be a function of ψ. The TPP frame, shown in Fig.2.6, is obtained from the blade rotating frame using rotations through an angle β_{1s} about the i_{NR} blade non-rotating axis and through an angle -β_{1s} about the $j_{TPP,I}$ TPP intermediate axis. The unit vectors along the TPP frame are given by

$$\begin{bmatrix} i_{TPP} \\ j_{TPP} \\ k_{TPP} \end{bmatrix} = T_{TN} \begin{bmatrix} i_{NR} \\ j_{NR} \\ k_{NR} \end{bmatrix} \tag{2.10}$$

The rotation matrix from the blade non-rotating axes to the TPP axes is given by

$$T_{TN} = \begin{bmatrix} \cos\beta_{1c} & 0 & \sin\beta_{1c} \\ 0 & 1 & 0 \\ \sin\beta_{1c} & 0 & \cos\beta_{1c} \end{bmatrix} \begin{bmatrix} 1 & 0 & 0 \\ 0 & \cos\beta_{1s} & \sin\beta_{1s} \\ 0 & -\sin\beta_{1s} & \cos\beta_{1s} \end{bmatrix}$$

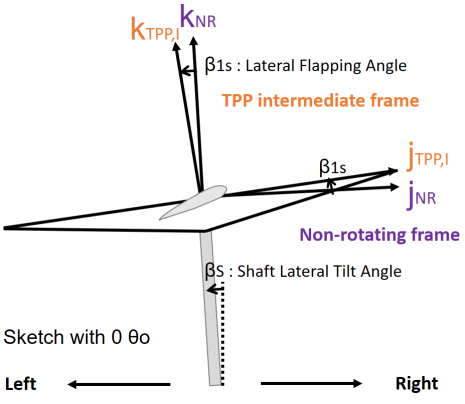

Figure 2.6: Geometry of the TPP in rear view

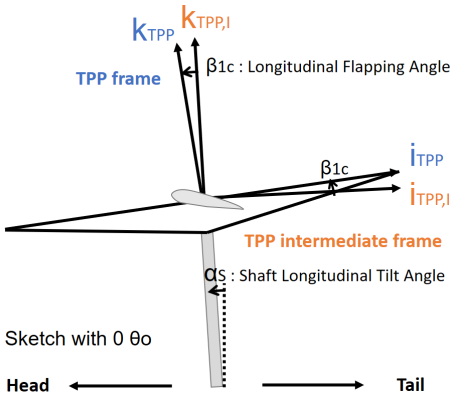

Figure 2.7: Geometry of the TPP in side view

2.3 RIGID BODY DYNAMICS

The helicopter fuselage is assumed to be rigid, and the inertial loads can be computed from the body-axis components of the airframe linear and angular velocities. These components are obtained from the partition of the system state vector that contains the fuselage states, given by

$$y_F \quad = \quad \{ \;\; u_F \;\; v_F \;\; w_F \;\; p_F \;\; q_F \;\; r_F \;\; \phi_F \;\; \theta_F \;\; \psi_F \;\; \}^T$$

The terms (u_F, v_F, w_F, p_F, q_F, r_F) are the linear velocities and angular velocities of the helicopter along and about body-fixed frame and (ϕ_F, θ_F, ψ_F) are the Euler angles which define the fuselage orientation with respect to the earth-fixed frame. Since the fuselage is rigid, the position and orientation of the lifting surfaces (main rotor, tail rotor, horizontal stabilator, and vertical fin) remain constant in the body-fixed frame. Furthermore, the moments of inertia of a rigid object stay the same in the body-fixed frame. Hence, it is convenient to formulate force and moment equilibrium equations along the helicopter fuselage body-fixed frame. The force equilibrium equations are

$$X = m_F(\dot{u_F} + q_F w_F - r_F v_F + g \sin\theta_F) \tag{2.11}$$

$$Y = m_F(\dot{v_F} + r_F u_F - p_F w_F - g \sin\phi_F \cos\theta_F) \tag{2.12}$$

$$Z = m_F(\dot{w_F} + p_F v_F - q_F u_F - g \cos\phi_F \cos\theta_F) \tag{2.13}$$

p_F, q_F, and r_F can be expressed in terms of the euler angles (ϕ_F, θ_F, ψ_F) and their time derivatives as

$$p_F = \dot{\phi_F} - \dot{\psi_F} \sin\theta_F \tag{2.14}$$

$$q_F = \dot{\theta_F} \cos phi_F + \dot{\psi_F} \cos\theta_F \sin\phi_F \tag{2.15}$$

$$r_F = -\dot{\theta_F} \sin phi_F + \dot{\psi_F} \cos\theta_F \cos\phi_F \tag{2.16}$$

The moment equilibrium equations are

$$L = I_{xx}\dot{p_F} - I_{xy}(\dot{q_F} - p_F r_F) - I_{xz}(\dot{r_F} - p_F q_F) - I_{yz}(q_F^2 - r_F^2) - (I_{yy} - I_{zz})q_F r_F \quad (2.17)$$

$$M = I_{yy}\dot{q_F} - I_{yz}(\dot{r_F} - q_F p_F) - I_{yx}(\dot{p_F} - q_F r_F) - I_{zx}(r_F^2 - p_F^2) - (I_{zz} - I_{xx})r_F p_F \quad (2.18)$$

$$N = I_{zz}\dot{r_F} - I_{zx}(\dot{p_F} - r_F q_F) - I_{zy}(\dot{q_F} - r_F p_F) - I_{xy}(p_F^2 - q_F^2) - (I_{xx} - I_{yy})p_F q_F \quad (2.19)$$

The terms on the left hand side of Eqs. (2.10) - (2.12) and (2.16) - (2.18) which are (X, Y, Z) and (L, M, N) represent the cumulative forces and moments about the center of gravity, respectively, exerted by airframe aerodynamics, main rotor loads, tail rotor loads, and empennage aerodynamics, and are given by

$$\begin{aligned}
X &= X_{MR} + X_{TR} + X_H + X_V + X_F \\
Y &= Y_{MR} + Y_{TR} + Y_H + Y_V + Y_F \\
Z &= Z_{MR} + Z_{TR} + Z_H + Z_V + Z_F \\
L &= L_{MR} + L_{TR} + L_H + L_V + L_F \\
M &= M_{MR} + M_{TR} + M_H + M_V + M_F \\
N &= N_{MR} + N_{TR} + N_H + N_V + N_F
\end{aligned}$$

The mathematical models for loads generated by each of these components are described in the following sections. The computations of forces and moments from the main rotor, tail rotor, empennage, and fuselage aerodynamics are included.

2.4 FUSELAGE

The aerodynamic forces and moments acting on the body of the fuselage are computed based on the flow velocity components at a "reference point" on the fuselage, given by

$$\begin{aligned} u_{ref} &= u_F + y_{ref} r_F - z_{ref} q_F + u_{in,F} \\ v_{ref} &= v_F + z_{ref} p_F - x_{ref} r_F + v_{in,F} \\ w_{ref} &= w_F + x_{ref} q_F - y_{ref} r_F + w_{in,F} \end{aligned}$$

The position vector of the fuselage reference point relative to the vehicle center of gravity is given by

$$r_{ref} = x_{ref} i_B + y_{ref} j_B + z_{ref} k_B$$

($u_{in,F}$, $v_{in,F}$, $w_{in,F}$) are interference velocity components along body axes, and are computed from the average main rotor downwash $\lambda_o \Omega_{MR} R$, nose-down tilt of the rotor tip path plane β_{1c} and wake skew angle χ as

$$\begin{aligned} u_{in,F} &= \lambda_o \Omega_{MR} R v_x(\beta_{1c}, \chi) \\ v_{in,F} &= 0 \\ w_{in,F} &= \lambda_o \Omega_{MR} R v_z(\beta_{1c}, \chi) \end{aligned}$$

The functions $v_x(\beta_{1c}, \chi)$ and $v_z(\beta_{1c}, \chi)$ are obtained from look-up tables, and the wake skew angle is obtained from the free-stream velocity components along shaft axes (u_s, v_s, w_s) as

$$
\begin{aligned}
\chi &= \tan^{-1}\frac{u_s}{\lambda\Omega_{MR}R - w_s} + \beta_{1c} \\
\alpha_F &= \tan^{-1}\frac{w_F}{u_F} \\
\beta_F &= \tan^{-1}\frac{v_F}{\sqrt{u_F^2 + w_F^2}}
\end{aligned}
$$

The longitudinal flow incidence angle α_F is positive when the fuselage is tilted nose-up with respect to the free-stream flow, and the lateral flow incidence angle β_F is is positive when the starboard side is facing the free-stream flow. Using these two flow angles and the dynamic pressure at the fuselage reference point q_F, the aerodynamic coefficients in the wind-axes system are obtained using a table look-up procedure based on wind-tunnel measurements, and transformed to the body axes. Representing the body-axes fuselage forces and moments at the fuselage reference point by F_F and M_F, respectively, the loads at the vehicle center of gravity are given by

$$
\begin{aligned}
\begin{bmatrix} X \\ Y \\ Z \end{bmatrix}_F &= q_F \begin{bmatrix} C_X \\ C_Y \\ C_Z \end{bmatrix}_F \\
\begin{bmatrix} L \\ M \\ N \end{bmatrix}_F &= q_F \begin{bmatrix} C_L \\ C_M \\ C_N \end{bmatrix}_F + r_{ref} \times F_F \\
q_F &= \frac{1}{2}\,\rho\,(u_F^2 + v_F^2 + w_F^2)
\end{aligned}
$$

2.5 MAIN ROTOR

This section covers description of the mathematical model of the main rotor system. The main rotor blades are individually analyzed. Forces and moments from each blade are translated to the body-fixed frame. Each blade experiences flap and lead-lag motions which are angle β and ζ, respectively. The flap and lead-lag hinge with its own spring and damper are placed at the same

position. The blade equations of motion are nonlinear, coupled, partial differential equations with periodic coefficients. In this research, the inertial and aerodynamic load vectors are calculated numerically with the assumption of the first harmonic blade motion. A blade is descretized to 100 finite elements and travels with 1° step displacement in azimuth. In addition, the negative twist rate of 18° is considered in the computation of elemental angle of attack. The summation of the loads on each blade element is collected and transformed to the body-fixed frame.

2.5.1 INERTIAL LOADS

In the formulation of the main rotor equations of motion, the distributed loads due to blade inertia are required. These inertia loads depend on the absolute acceleration of a point on the rotor blade, A_P. Taking into account the helicopter hub accelerations, an arbitrary point "P" on a blade is expressed in mixed coordinate systems as

$$R_P \quad = \quad R_{cg} \quad + \quad R_{hub} \quad + \quad R_b \tag{2.20}$$

R_{cg} represents the position of the CG from the earth-fixed frame origin. R_{hub} represents the position of the hub from the CG. R_b represents the position of an arbitrary point on a blade with consideration for the hinge offset.

$$\begin{aligned}
R_{cg,B} &= T_{BG} \;\; R_{cg,G} \\
R_{hub,B} &= T_{BN} \;\; R_{hub,NR} \\
R_{b,B} &= T_{BL} \;\; R_{b,L} \\
&= T_{BN} \;\; T_{NR} \;\; T_{RF} \;\; T_{FL} \;\; R_{b,L} \\
R_{P,B} &= R_{cg,B} \quad + \quad R_{hub,B} \quad + \quad R_{b,B}
\end{aligned}$$

The velocity and acceleration of a generic point of the blade in the body-fixed frame need to be calculated. Based on the transport theorem, the velocity $V_{P,B}$ of the point P is calculated by

$$
\begin{aligned}
V_{P,B} &= \frac{dR_{P,B}}{dt} = \frac{\partial R_P}{\partial t} + W \times R_P \\
&= \frac{\partial R_{cg,B}}{\partial t} + \frac{\partial R_{b,L}}{\partial t} + (W_{B\leftarrow NR} + W_{NR\leftarrow R} + W_{R\leftarrow F} + W_{F\leftarrow L}) \times R_{b,L}
\end{aligned} \tag{2.21}
$$

Terms $\frac{\partial R_{cg,B}}{\partial t}$ and $\frac{\partial R_{b,L}}{\partial t}$ are the velocity of the CG in the body-fixed frame and the the velocity of the point P on a blade in the blade lagged frame, respectively. The time derivative of the hub in the body-fixed frame is zero since it is constant with respect to time. The other term $W \times R_{b,L}$ is taking into account the transformation of coordinate systems and the fact that the blade is rotating. The subscripts of W describe the transformation from one frame to another frame. In order to show the transform sequence from the lagged frame to the body-fixed frame, W is separated out step by step. In a similar manner, the acceleration $A_{P,B}$ of the point P is calculated by

$$
\begin{aligned}
A_{P,B} &= \frac{dV_{P,B}}{dt} = \frac{\partial V_P}{\partial t} + W \times V_P \\
&= \frac{\partial V_{cg,B}}{\partial t} + \frac{\partial V_{b,L}}{\partial t} + (W_{B\leftarrow NR} + W_{NR\leftarrow R} + W_{R\leftarrow F} + W_{F\leftarrow L}) \times V_{b,L}
\end{aligned} \tag{2.22}
$$

The total inertial force in the body-fixed frame are obtained by integrating along the blade and along the azimuth as

$$
F_{I,B} = \frac{Nb}{2\pi} \int_0^{2\pi} \int_{eR}^{R} m_b \; A_{P,B} \; dr d\psi
$$

N_b is the number of blades, m_b is the blade mass per unit length, and eR is the hinge offset distance from the hub. By adding a hinge, the sum of applied moments about the hinge have to be zero. First, inertial moment about the hinge for a blade M_I is calculated by

$$
M_I = \int_{eR}^{R} m_b \; (R_{b,L} \times A_{P,L}) \; dr
$$

2.5.2 AERODYNAMIC LOADS

A key ingredient for the calculation of the aerodynamic forces and moments is the absolute velocity of a point on the blade in the blade lagged frame, which is the derivative with respect to time of the position vector of a point on the blade relative to a fixed point. The total velocity V_T of the point on a blade is given by

$$V_T = V_P - V_I \tag{2.23}$$

where V_I is the velocity induced at the point on blade by the rotor wake. In the blade flapped frame, the components of the velocity V_P can be written in the form

$$V_P = V_{i,F}\ \ i_F + V_{j,F}\ \ j_F + V_{k,F}\ \ k_F \tag{2.24}$$

i_F, j_F, and k_F are the unit vectors of the blade flapped frame and $V_{x,F}$, $V_{y,F}$, and $V_{z,F}$ are the velocity components in each of these directions.

$$V_I = \lambda_i\ \ i_F + \lambda_j\ \ j_F + \lambda_k\ \ k_F \tag{2.25}$$

λ_i, λ_j, and λ_k are the i, j, and k components in the blade flapped frame of the induced velocity. With the dynamic inflow model, only the k component of the induced velocity is available. Including only the k component of the induced velocity, the total velocity is

$$V_T = V_{i,F}\ \ i_F + V_{j,F}\ \ j_F + (V_{k,F} - \lambda_k)\ \ k_F \tag{2.26}$$

$$= V_{x,F}\ \ i_F + V_{y,F}\ \ j_F + V_{z,F}\ \ k_F \tag{2.27}$$

V_x, V_y, and V_z are the velocity components in the blade flapped frame. Using the coordinate transformation, which takes into account the lead-lag angles of the blade, this total velocity can be

expressed in terms of the airflow velocity components in the blade lagged frame.

$$V_T = U_R \ i_L + U_T \ j_L + U_P \ k_L \tag{2.28}$$

V_T is the resultant velocity of the airflow at the quarter-chord location. The U_T and U_R components follow the sign conventions by which U_T is positive for an airflow coming toward the leading edge of the airfoil and U_R is positive for an outboard flow. The component U_P is defined as positive for a flow going downward.

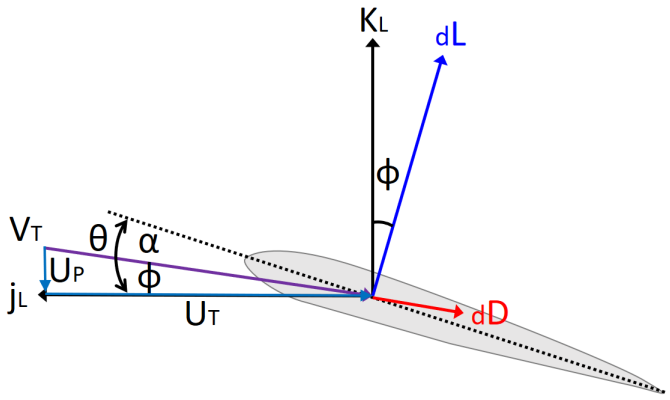

Figure 2.8: Blade elemental lift and drag

The body-fixed linear velocity components, which are u, v, and w along the i_B, j_B, and k_B, respectively, can be related to the fuselage angles and the total velocity V_T as

$$u = V_T \ \cos\alpha_F \ \cos\beta_F$$

$$v = V_T \ \sin\beta_F$$

$$w = V_T \ \sin\alpha_F \ \cos\beta_F$$

The elemental lift dL, drag dD, and force along the lagged frame are, respectively

$$\begin{aligned} dL &= \frac{1}{2}\ \rho\ V_T^2\ c_l\ c\ dr \\ dD &= \frac{1}{2}\ \rho\ V_T^2\ c_d\ c\ dr \\ dF_L &= (dL\cos\phi - dDsin_\phi)\ k_L\ -\ (dL\sin\phi + dD\cos\phi)\ j_L \end{aligned}$$

ρ is the air density, *c* is the chord length, and *dr* is the blade element of span. By assuming linear incompressible aerodynamics, c_l can be a function of the lift slope and angle of attack(c_l = *a* α). *a* is the lift slope and α is the angle of attack. c_d is assumed constant. These are reasonable under the linear range of c_l and c_d with respect to the angle of attack. The aerodynamic angle of the cross section α is given by

$$\alpha \quad = \quad \theta\ -\ \phi \quad = \quad \theta\ -\ \tan^{-1}\frac{U_P}{U_T}$$

The local geometric pitch at each radial station θ, defined as

$$\theta \quad = \quad \theta_o\ +\ \theta_{1c}\cos\psi_n\ +\ \theta_{1s}\sin\psi_n\ +\ \theta_{tw}$$

θ_o is the collective pitch, θ_{1c} is the lateral cyclic, θ_{1s} is the longitudinal cyclic, and θ_{tw} is the the built-in twist. Thus, *dL* can be re-written as

$$\begin{aligned} dL &= \frac{1}{2}\ \rho\ V_T^2\ a\ \alpha\ c\ dr \\ &= \frac{1}{2}\ \rho\ U_T^2\ a\ (\theta\ -\ \frac{U_P}{U_T})\ c\ dr \\ &= \frac{1}{2}\ \rho\ a\ (\theta\ U_T^2\ -\ U_P\ U_T)\ c\ dr \end{aligned}$$

Integrating over the blade span and along the azimuth yields the total aerodynamic forces as

$$\begin{aligned} F_{A,L} &= \frac{Nb}{2\pi} \int_0^{2\pi} \int_{eR}^{R} dF_{P,L} \; dr d\psi \\ F_{A,B} &= T_{BL} \; F_{A,L} \end{aligned}$$

Aerodynamic flap moment M_A about the hinge is computed by

$$\begin{aligned} M_A &= \int_{eR}^{R} r \times dL \; dr \\ &= \frac{1}{2} \; \rho \; a \int_{eR}^{R} (\theta \; U_T^2 - U_P \; U_T) \; c \; dr \\ &= \frac{\gamma}{2} \; \Omega^2 \; I_b \int_{eR}^{R} \left[\theta \; (\frac{U_T}{\Omega R})^2 - (\frac{U_P}{\Omega R}) \; (\frac{U_T}{\Omega R}) \right] \; dr \end{aligned}$$

where the lock number γ, the mass flapping moment of inertia I_b are

$$\begin{aligned} \gamma &= \frac{\rho \; a \; c \; R^4}{I_b} \\ I_b &= \int_{eR}^{R} m_b \; (r - eR)^2 \; dr \end{aligned}$$

Since M_A has the blade tip speed term in common, it is convenient to define advance ratio μ and inflow ratio λ with respect to the blade tip speed as

$$\begin{aligned} \mu &= \frac{V_T \; \cos\alpha}{\Omega R} \\ \lambda &= \frac{v}{\Omega R} \\ &= \frac{v_i - V_T \; \sin\alpha_F \; \cos\beta_F}{\Omega R} \\ &= \frac{v_i - w}{\Omega R} \end{aligned}$$

where v is the inflow velocity and v_i is the induced velocity which are normal to TPP.

2.5.3 HUB LOADS

The forces and moments transmitted to the hub are obtained by integrating the loads along the span and summing the contributions from each of the blades. The force components along the blade rotating frame from the n^{th} blade are

$$\begin{aligned} X_{MR,R}(n) &= \int_{eR}^{R} dX_{MR,R} dr \\ Y_{MR,R}(n) &= \int_{eR}^{R} dY_{MR,R} dr \\ Z_{MR,R}(n) &= \int_{eR}^{R} dZ_{MR,R} dr \end{aligned}$$

$dX_{MR,R}$, $dY_{MR,R}$, and $dZ_{MR,R}$ represent the moment components per unit span along the blade rotating frame which contain the sum of inertial and aerodynamic loads. The hub loads are obtained by resolving the blade loads along the blade non-rotating frame and summing the contributions from individual blades. The hub force and moment components are

$$\begin{bmatrix} X_{MR} \\ Y_{MR} \\ Z_{MR} \end{bmatrix}_{NR} = \sum_{n=1}^{Nb} T_{NL} \begin{bmatrix} X_{MR}(n) \\ Y_{MR}(n) \\ Z_{MR}(n) \end{bmatrix}_{L}$$

$$\begin{bmatrix} L_{MR} \\ M_{MR} \\ N_{MR} \end{bmatrix}_{NR} = \sum_{n=1}^{Nb} T_{NL} \begin{bmatrix} L_{MR}(n) \\ M_{MR}(n) \\ N_{MR}(n) \end{bmatrix}_{L}$$

The hub loads are converted to the helicopter body-fixed frame using the transformation matrix T_{BN} which are the main rotor contributions to the helicopter force and moment equilibrium as

$$\begin{bmatrix} X_{MR} \\ Y_{MR} \\ Z_{MR} \end{bmatrix}_B = T_{BN} \begin{bmatrix} X_{MR} \\ Y_{MR} \\ Z_{MR} \end{bmatrix}_{NR}$$

$$\begin{bmatrix} L_{MR} \\ M_{MR} \\ N_{MR} \end{bmatrix}_B = T_{BN} \begin{bmatrix} L_{MR} \\ M_{MR} \\ N_{MR} \end{bmatrix}_{NR} + \begin{bmatrix} y_{hub}Z_{MR,B} - z_{hub}Y_{MR,B} \\ z_{hub}X_{MR,B} - x_{hub}Z_{MR,B} \\ x_{hub}Y_{MR,B} - y_{hub}X_{MR,B} \end{bmatrix}$$

2.5.4 BLADE FLAPPING AND LAGGING DYNAMICS

2.5.4.1 EQUILIBRIUM ABOUT FLAPPING HINGE

The equilibrium position of the blade is determined by the balance of inertial, aerodynamic, and centrifugal forces (CF). The flapping angle can be assumed small due to the fact that the centrifugal force is larger than the aerodynamic force. Moment equilibrium about the flapping hinge is expressed as

$$M_{I,F} + M_{CF,F} + M_{A,F} = 0$$

$$\int_{eR}^{R} m_b(y - eR)^2 \ddot{\beta} dy + \int_{eR}^{R} m_b \Omega^2 y(y - eR)\beta dy - \int_{eR}^{R} L(y - eR)dy = 0$$

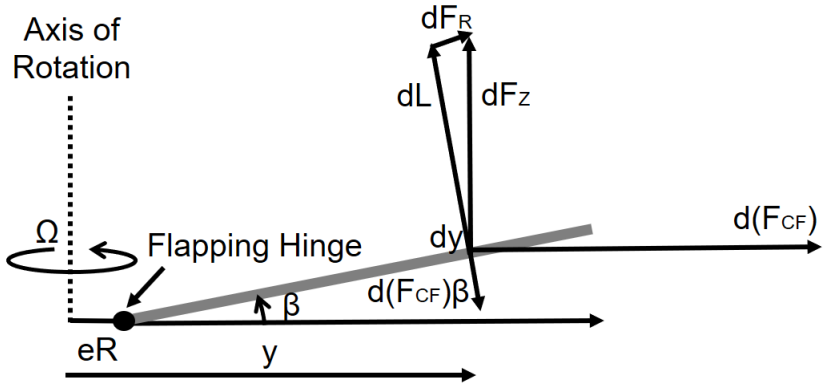

Figure 2.9: Geometry of Blade Flapping Equilibrium

Integrating along the blade and dividing by Ω^2 yields

$$\begin{aligned} I_b(\overset{**}{\beta} + v_\beta^2\beta) &= \frac{1}{\Omega^2}\int_{eR}^{R} L(y - eR)dy \\ v_\beta^2 &= 1 + \frac{eR\int_{eR}^{R} m_b(y - eR)dy}{I_b} \\ v_\beta &= \omega_n = \sqrt{1 + \frac{3e}{2(1-e)}} \end{aligned}$$

where v_β is the non-dimensional flapping frequency in terms of the rotational speed and it can also be considered as the undamped natural frequency in a spring-mass-damper system. Hence, the flapping equation can be expressed by

$$\overset{**}{\beta} + v_\beta^2\beta = \gamma M_{A,F} \tag{2.29}$$

Generally, the value of e varies from 4 to 6% for an articulated blade, so that the natural frequency of the rotor is slightly greater than Ω or 1/rev. This also means that the phase lag between the forcing and the rotor flapping response has to be less than 90° and the flapping displacements also now depend on aerodynamic damping. After expanding all terms in the aerodynamic flapping moment M_A, it can be re-expressed as

$$M_{A,F} = \frac{1}{2}\rho ac\Omega^2 R^4(M_\theta\theta + M_\lambda\lambda + M_{\overset{*}{\beta}}\overset{*}{\beta} + M_\beta\beta + M_p\frac{p}{\Omega} + M_q\frac{q}{\Omega}) \tag{2.30}$$

The flap damping term is the coefficient $M_{\overset{*}{\beta}}$ and it is associated with lock number. Investigating hover case, the damping is approximately 50% which means the blade flapping motion is stable and well damped. Assuming the blade flapping motion is the first harmonic only, it can be expressed as a function of the blade azimuth ψ_n by

$$\beta_{\psi_n} = \beta_o + \beta_{1c}\cos\psi_n + \beta_{1s}\sin\psi_n \tag{2.31}$$

By replacing flapping terms to constant and periodic terms on both sides of the flapping equation flapping angels can be related to control angles (θ_o, θ_{1c}, θ_{1s}).

2.5.4.2 EQUILIBRIUM ABOUT LEAD-LAG HINGE

The equilibrium of the blade about the lead-lag hinge is determined by a balance of centrifugal and aerodynamic moments. The aerodynamic moments are generated by the aerodynamic drag of the blade as it rotates. Moment equilibrium about the lead-lag hinge is expressed as

$$\begin{aligned} M_{I,L} \quad + \quad M_{CF,L} \quad + \quad M_{A,L} \quad &= \quad 0 \\ -\int_{eR}^{R} m_b(y-eR)^2\ddot{\zeta}dy \; + \; \int_{eR}^{R} m_b\Omega^2 y(y-eR)\frac{eR}{y}\zeta dy \; + \; \int_{eR}^{R} D(y-eR)dy \quad &= \quad 0 \end{aligned}$$

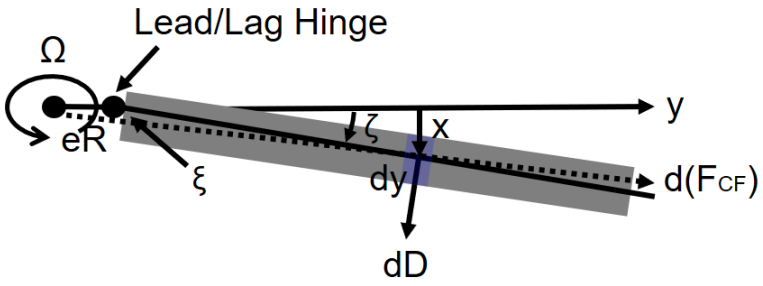

Figure 2.10: Geometry of Blade Lagging Equilibrium

Integrating along the blade and dividing by Ω^2 yields

$$\begin{aligned} I_\zeta(\overset{**}{\zeta} \; + \; v_\zeta^2\zeta) \quad &= \quad \frac{1}{\Omega^2}\int_{eR}^{R} D(y \; - \; eR)dy \\ v_\zeta^2 \quad &= \quad \frac{eR\int_{eR}^{R} m_b(y \; - \; eR)dy}{I_\zeta} \\ v_\zeta \quad &= \quad \sqrt{\frac{3}{2}(\frac{eR}{R \; - \; eR})} \\ (\; I_\zeta \quad &= \quad \int_{eR}^{R} m_b(y \; - \; eR)^2 dy \;) \end{aligned}$$

I_ζ is the mass moment of inertia about the lead-lag hinge, v_ζ is the non-dimensional lag frequency. The centrifugal restoring moment about the lag hinge is much smaller than in flapping, the corresponding uncoupled natural frequency of the lag motion is much smaller. For articulated rotors such as UH-60 rotors, the uncoupled rotating lag frequency varies from about 0.2 to 0.3Ω. The lead-lag displacements about the hinge are small and aerodynamic forces are produced by changes in velocity and dynamic pressure normal to the leading edge of the blade. However, it is much smaller than the aerodynamic forces which are produced through flapping motion by changes in angle of attack. Furthermore, the drag forces acting on the blades are also much smaller than the life forces.

2.5.5 INFLOW DYNAMICS

In this study, a linear inflow distribution is assumed, thus it is expressed with respect to the blade azimuth ψ_n as

$$\lambda \quad = \quad \lambda_o \; + \; \lambda_{1c}\frac{r}{R}\cos\psi_n \; + \; \lambda_{1s}\frac{r}{R}\sin\psi_n$$

Basically, modeling a linear inflow distribution is to estimate the values of λ_o, λ_{1c}, and λ_{1s}. For this mathematical UH-60 helicopter model, the Pitt-Peters linear inflow model is used.

$$[M] \begin{bmatrix} \dot{\lambda_o} \\ \dot{\lambda_{1c}} \\ \dot{\lambda_{1s}} \end{bmatrix} + [L]^{-1} \begin{bmatrix} \lambda_o \\ \lambda_{1c} \\ \lambda_{1s} \end{bmatrix} = \begin{bmatrix} C_T \\ -C_{M_y} \\ C_{M_x} \end{bmatrix}$$

These dynamic inflow components are related to the forces on the rotor disk which are the rotor thrust coefficient C_T, pitching moment coefficient C_{M_y}, and rolling moment coefficient C_{M_x}. The matrix size of M and L is 3 by 3 which are given by

$$[L] = \frac{1}{C_V}\begin{bmatrix} \frac{1}{2} & 0 & \frac{15\pi}{64}\sqrt{\frac{1-\sin\alpha}{1+\sin\alpha}} \\ 0 & \frac{-4}{1+\sin\alpha} & 0 \\ \frac{15\pi}{64}\sqrt{\frac{1-\sin\alpha}{1+\sin\alpha}} & 0 & \frac{4}{1+\sin\alpha} \end{bmatrix}$$

$$[M] = \begin{bmatrix} \frac{128}{75\pi} & 0 & 0 \\ 0 & -\frac{16}{45\pi} & 0 \\ 0 & 0 & -\frac{16}{45\pi} \end{bmatrix}$$

where α is the rotor disk tilt angle with respect to the free stream and C_V is the mass-flow parameter which can be computed by

$$C_V = \frac{\mu^2 + \lambda(\lambda + \lambda_i)}{\sqrt{\mu^2 + \lambda^2}}$$

For dynamic analysis of the blade, the dynamic inflow components are treated as additional degrees of freedom. It is formulated on the basis of experimental results or more advanced vortex theories and it is well suited for helicopter rotor aerodynamics, aeroelasticity, and flight dynamics.

2.6 TAIL ROTOR

2.6.1 TAIL ROTOR AERODYNAMICS

The tail rotor model is based on a simplified implementation of the closed-form solution given by F. J. Bailey [34], which relates the free-stream velocity to the rotor thrust, torque and induced inflow. The velocity at the tail rotor reference point (hub) is

$$V_{TR} \quad = \quad V_b \quad + \quad \omega \times r_{TR} \quad + \quad V_{in,TR}$$

$V_{in,TR}$ represents the induced velocity at the tail rotor reference point due by the wake of the main rotor and fuselage, given by

$$V_{in,TR} \quad = \quad \lambda_o \Omega_{MR} R \Big[v_{x_{TR}}(\beta_{1c}, \chi) i_B \quad + \quad v_{z_{TR}}(\beta_{1c}, \chi) k_B \Big]$$

The functions $v_{x,TR}$, $v_{z,TR}$ are obtained from look-up tables based on the wake skew angle χ and the tip-path plane tilt β_{1c} with respect to the fuselage. The velocity V_{TR} at the tail rotor reference point r_{TR} is resolved into components along the tail rotor axes. The tail rotor axes system are obtained using two rotations in the sequence Z $\rightarrow$ Y through angles (Γ_{TR}, Λ_{TR}) starting from the helicopter body axes. The rotation matrix from fuselage body axes to tail rotor axes is given by

$$T_{TR,B} \quad = \quad \begin{bmatrix} \cos\Lambda_{TR} & 0 & -\sin\Lambda_{TR} \\ 0 & 1 & 0 \\ \sin\Lambda_{TR} & 0 & \cos\Lambda_{TR} \end{bmatrix} \quad \begin{bmatrix} \cos\Gamma_{TR} & \sin\Gamma_{TR} & 0 \\ -\sin\Gamma_{TR} & \cos\Gamma_{TR} & 0 \\ 0 & 0 & 1 \end{bmatrix}$$

The velocity components in the tail rotor reference frame are

$$\begin{bmatrix} u \\ v \\ w \end{bmatrix}_{TR} \quad = \quad T_{TR,B} \;\; V_{TR} \cdot \begin{bmatrix} i_B \\ j_B \\ k_B \end{bmatrix}$$

The tail rotor thrust (assumed to act along the shaft direction) is

$$\begin{aligned} T_{TR} &= \pi\ R_{TR}^4\ \Omega_{TR}^2\ |V|_{TR}\ v_{i,TR}\ K_{TR} \\ v_{i,TR} &= \lambda_{TR}\Omega_{TR}R_{TR} \\ |V|_{TR} &= \sqrt{u_{TR}^2\ +\ v_{TR}^2\ +\ (w_{TR}^2\ -\ \lambda_{TR}\Omega_{TR}R_{TR})^2} \end{aligned}$$

$v_{i,TR}$ is the average induced velocity of the tail rotor, K_{TR} accounts for blockage effects of the vertical fin, and $|V|_{TR}$ is the magnitude of the total velocity (including induced inflow) at the tail rotor. The tail rotor torque due to induced and profile drag is

$$Q_{TR} = C_{Q_{TR}}\ \rho\ \pi\ \Omega_{TR}^2\ R_{TR}^5$$

The forces and moment components in fuselage body axes exerted by the tail rotor on the airframe center of gravity are obtained using a coordinate transformation

$$\begin{bmatrix} X \\ Y \\ Z \end{bmatrix}_{TR} = T_{TR,B}^T \begin{bmatrix} 0 \\ -T_{TR} \\ 0 \end{bmatrix}$$

$$\begin{bmatrix} L \\ M \\ N \end{bmatrix}_{TR} = T_{TR,B}^T \begin{bmatrix} 0 \\ -Q_{TR} \\ 0 \end{bmatrix} + r_{TR} \times (X_{TR}i_B\ +\ Y_{TR}j_B\ +\ Z_{TR}k_B)$$

2.6.2 TAIL ROTOR DYNAMIC INFLOW

The induced inflow of the tail rotor is assumed to be uniform over the disk, and is represented using a 1-state Pitt-Peters dynamic inflow model. The ODE governing the inflow dynamics is

$$\frac{4R_{TR}}{2\pi|V_{TR}|}\dot{\lambda}_{TR} + \lambda_{TR} = \frac{C_{T_{TR}}\Omega_{TR}R_{TR}}{2|V_{TR}|}$$

2.7 EMPENNAGE

The aerodynamic loads acting on the horizontal stabilator and vertical fin are computed using a procedure similar to that followed for the fuselage. The velocity at the reference point for each lifting surface is computed from the fuselage translation velocity V_b, angular velocity w_b and the position of the reference points with respect to the vehicle center of gravity r_H, r_V as

$$\begin{aligned} V_H &= K_H V_b + \omega \times r_H + V_{in,H} \\ V_V &= K_V V_b + \omega \times r_V + V_{in,V} \end{aligned}$$

K_H and K_H are used to empirically model the dynamic pressure loss at the tail surfaces, which occurs as a result of operating in the wake of the airframe. $V_{in,H}$ and $V_{in,V}$ represent the velocities at the tail surfaces induced by the main rotor wake, obtained from wind-tunnel tests as

$$\begin{aligned} V_{in,H} &= \lambda_o \Omega_{MR} R \Big[v_{x_H}(\beta_{1c}, \chi) i_B + v_{z_H}(\beta_{1c}, \chi) k_B \Big] \\ V_{in,V} &= \lambda_o \Omega_{MR} R \Big[v_{x_V}(\beta_{1c}, \chi) i_B + v_{z_V}(\beta_{1c}, \chi) k_B \Big] \end{aligned}$$

The functions $v_{x_H}, v_{z_H}, v_{x_V}, v_{z_V}$ are obtained from look-up tables based on the wake skew angle χ and the tip-path plane tilt β_{1c} with respect to the fuselage. Using (u_H, v_H, w_H) and (u_V, v_V, w_V) to represent the velocity components at the horizontal stabilator and vertical fin, respectively, along vehicle body axes, the angles of attack and sideslip at the tail surfaces are computed as

$$\begin{aligned} \alpha_H &= \tan^{-1} \frac{w_H}{u_H} + \theta_H \\ \beta_H &= \tan^{-1} \frac{v_H}{\sqrt{u_H^2 + w_H^2}} \\ \alpha_V &= \tan^{-1} \frac{w_V}{u_V} \\ \beta_V &= \tan^{-1} \frac{u_V}{\sqrt{u_V^2 + w_V^2}} \end{aligned}$$

The pitch of the horizontal stabilator θ_H is scheduled to change with the fuselage speed in a prescribed manner. An approach similar to that followed for the fuselage aerodynamics is utilized for computing the forces on the horizontal stabilator and vertical fin. Using the incidence angles α and β for each surface and the dynamic pressure at the reference points, the aerodynamic lift and drag coefficients are obtained using a table look-up procedure based on wind-tunnel measurements, and transformed to the helicopter body axes. Using (F_H, F_V) and (M_H, M_V) to represent the body-axes forces and moments, respectively, at the reference points, the loads at the vehicle center of gravity are given by

$$\begin{bmatrix} X \\ Y \\ Z \end{bmatrix}_{EM} = q_H \begin{bmatrix} C_X \\ C_Y \\ C_Z \end{bmatrix}_H + q_V \begin{bmatrix} C_X \\ C_Y \\ C_Z \end{bmatrix}_V$$

$$\begin{bmatrix} L \\ M \\ N \end{bmatrix}_{EM} = r_H \times F_H + r_V \times F_V$$

The dynamic pressures are given by

$$q_H = \frac{1}{2} \rho \, V_H \cdot V_H$$

$$q_V = \frac{1}{2} \rho \, V_V \cdot V_V$$

3. TRIM SOLUTION AND LINEARIZED MODEL EXTRACTION

This chapter describes the numerical solutions to solve the governing equations of a UH-60 helicopter. The first section details how to compute trim values and compares the results with flight test data. The second section explains how to extract linearized models about equilibrium points which are effective for stability analysis and modern control system design. UH-60 parameters which are specified in Table A.1 are used in this study.

3.1 TRIM SOLUTION

The term "trim" refers to a steady flight condition that the linear accelerations along the body axes and angular accelerations about the body axes are zero. The trim unknowns "X" are

$$
\begin{aligned}
X &= [\ X_C\ \ X_F\ \ X_R\ \ X_I\ ]^T \\
X_C &= [\ \theta_o\ \ \theta_{1c}\ \ \theta_{1s}\ \ \theta_{TR}\ ]^T \\
X_F &= [\ \alpha_F\ \ \beta_F\ \ \phi_F\ \ \theta_F\ ]^T \\
X_R &= [\ \beta_o\ \ \beta_{1c}\ \ \beta_{1s}\ \ \zeta_o\ \ \zeta_{1c}\ \ \zeta_{1s}\ ]^T \\
X_I &= [\ \lambda_o\ \ \lambda_{1c}\ \ \lambda_{1s}\ \ \lambda_{TR}\ ]^T
\end{aligned}
$$

X_C contains control angles, X_F contains fuselage angles, X_R contains flap and lead-lag angles, and X_I contains inflow angles. Trim unknowns which meet the trim condition are calculated under several flight conditions. The flight condition is defined by the velocity V along the trajectory, the flight path angle γ(positive for climbing), and the rate of turn $\dot{\psi}$(positive for a right turn).

3.1.1 TRIM IN HOVER AND STEADY FORWARD FLIGHT

Straight and level flight is a particular case in which both the flight path angle and the rate of turn are zero. Hover is a particular case in which the velocity is also zero. The following results presented here are simulated with a gross weight of 16,000 lbs at an altitude of 5,250 feet. First of all, main rotor power along the forward flight speed is investigated and compared to flight test

data. Other than the given condition, additional power comparisons are conducted under the other condition, which has a gross weight of 16,360 lbs at an altitude of 5,250 feet due to its ample flight test data.

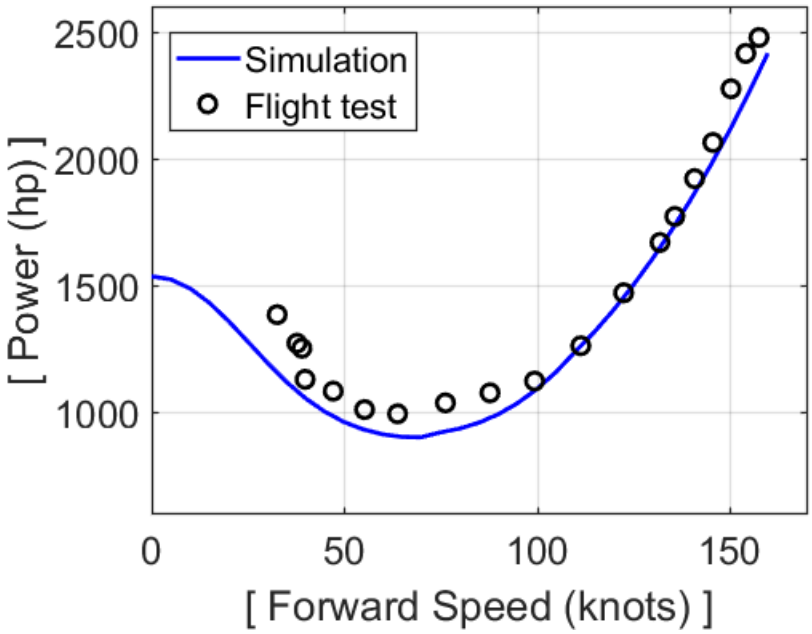

Figure 3.1: Main Rotor Power vs. Forward Flight Speed (16,360 lbs at 3,670 feet)

Figure 3.1 shows the comparison of predicted (simulated) main rotor power with flight test data from hover to 160 knots. In this comparison, the gross weight is 16,360 lbs and the density altitude is 3,670 feet. The comparisons show good agreement at speeds above 40 knots. At low speeds (below 30 knots), the simulated power curve under-predicts the power due to the linear inflow assumption. It can be enhanced by using an inflow model which captures rotor-wake interference. Typically, rotor-wake interference is stronger at $\mu < 0.1$. Thus, it requires more power at low speeds.

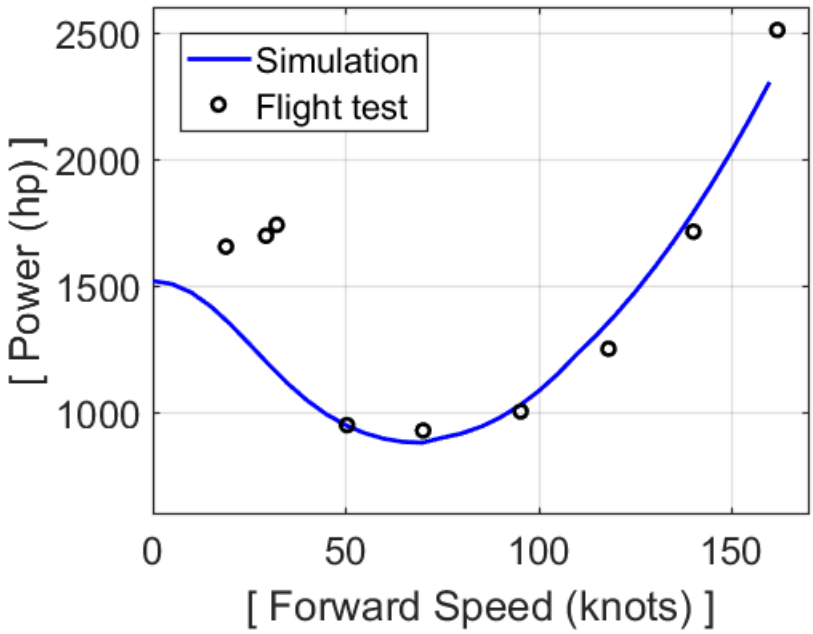

Figure 3.2: Fuselage Angle vs. Forward Flight Speed (16,000 lbs at 5,250 feet)

Figure 3.2 shows the additional comparison of predicted (simulated) main rotor power with flight test data from hover to 160 knots as well. In this comparison, the gross weight is 16,000 lbs and the density altitude is 5,250 feet. The comparison results are similar to the previous one in Figure 3.1. It also shows good agreement at speeds above 50 knots. However, at low speeds (below 30 knots), the simulated power curve under-predicts the power due to the linear inflow assumption due to the same reason. Analyzing the power curves which are obtained from different conditions, the mathematical model with the linear inflow assumption has good agreement at higher speed. Considering the results by Ananth Sridharan [36] and Maria Ribera [37], the free-vortex wake model can improve the power curve at lower speed.

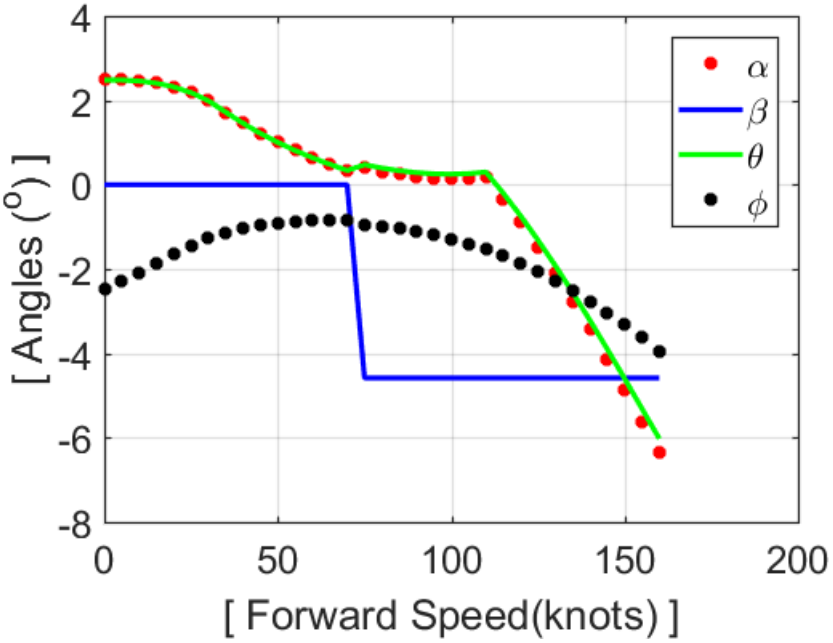

Figure 3.3: Fuselage Angle vs. Forward Flight Speed (16,000 lbs at 5,250 feet)

Figure 3.3 shows the fuselage angles along the forward speed from hover to 160 knots. The simulation results presented here are conducted with a gross weight of 16,000 lbs at an altitude of 5,250 feet. α is the flow Angle of Attack (AOA) with respect to TPP. β is the side slip angle of the fuselage. θ is the pitch angle of the fuselage. ϕ is the roll angle of the fuselage. It is natural that the nose of the helicopter goes down as it increases the forward speed. It indicates that the helicopter pitch angle at hover has positive value which means nose up. In reality, this is also true. These angles describe the helicopter trim attitude at various forward flight speed. Fuselage pitch angle and roll angle are also validated with flight test date in Figure 3.4 and Figure 3.5. Considering the magnitude of the angles, those angles show great agreement with the flgit test data.

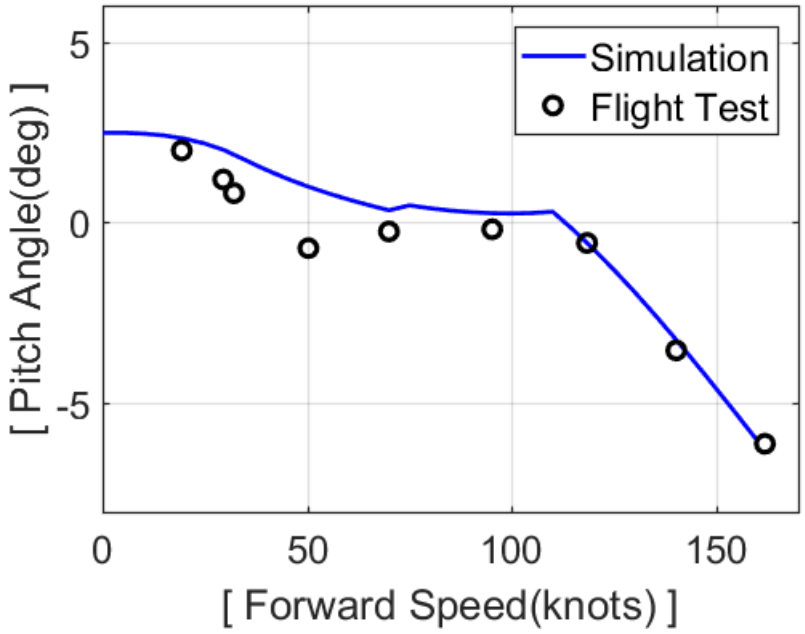

Figure 3.4: Fuselage Pitch Angle vs. Forward Flight Speed (16,000 lbs at 5,250 feet)

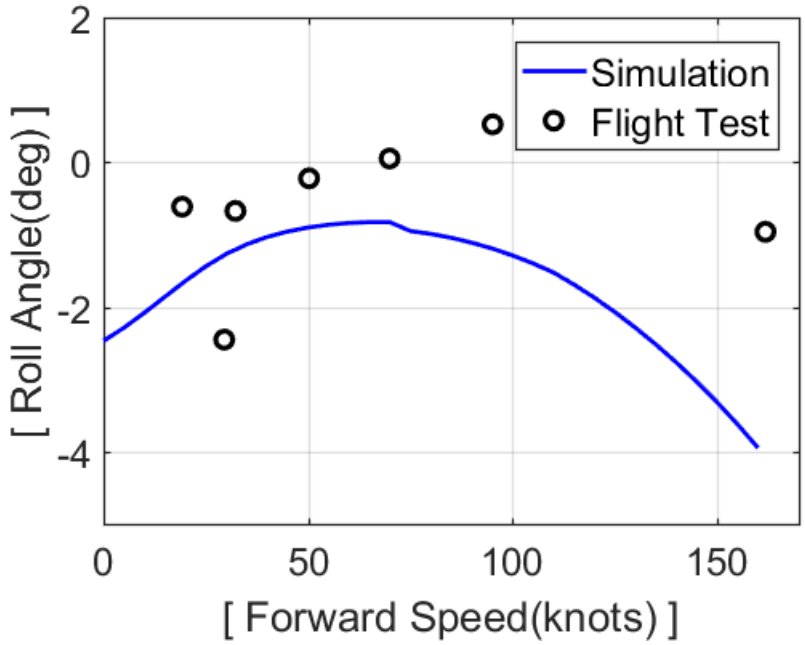

Figure 3.5: Fuselage Roll Angle vs. Forward Flight Speed (16,000 lbs at 5,250 feet)

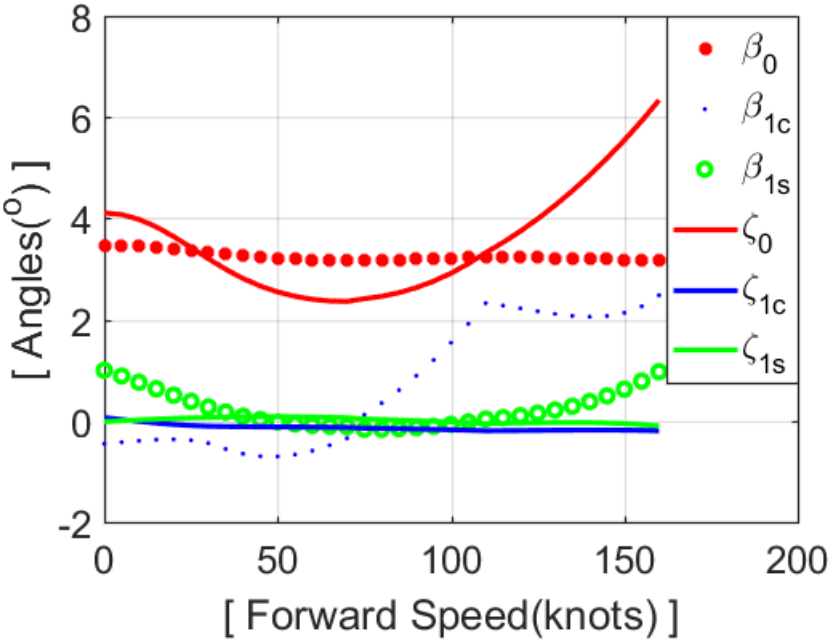

Figure 3.6: Flap and Lead-Lag Angle vs. Forward Flight Speed (16,000 lbs at 5,250 feet)

Figure 3.6 shows the trim values of flap angles and lead-lag angles at various forward speed. The angles are obtained by assuming the first harmonic (1/rev) flap and lead-lag motions. Coning angle β_o is the mean part of the flapping motion which is independent from time or blade azimuth. β_{1c} is the longitudinal flapping angle which represents the amplitude of the pure cosine flapping motion. β_{1s} is the lateral flapping angle which represents the amplitude of the pure sine flapping motion. Lead-lag motion is also separated by ζ_o, ζ_{1c}, and ζ_{1s} in the same manner. ζ_o represents the mean lagging motion. ζ_{1c} is the longitudinal lagging angle which represents the amplitude of the pure cosine lagging motion. β_{1s} is the lateral lagging angle which represents the amplitude of the pure sine lagging motion.

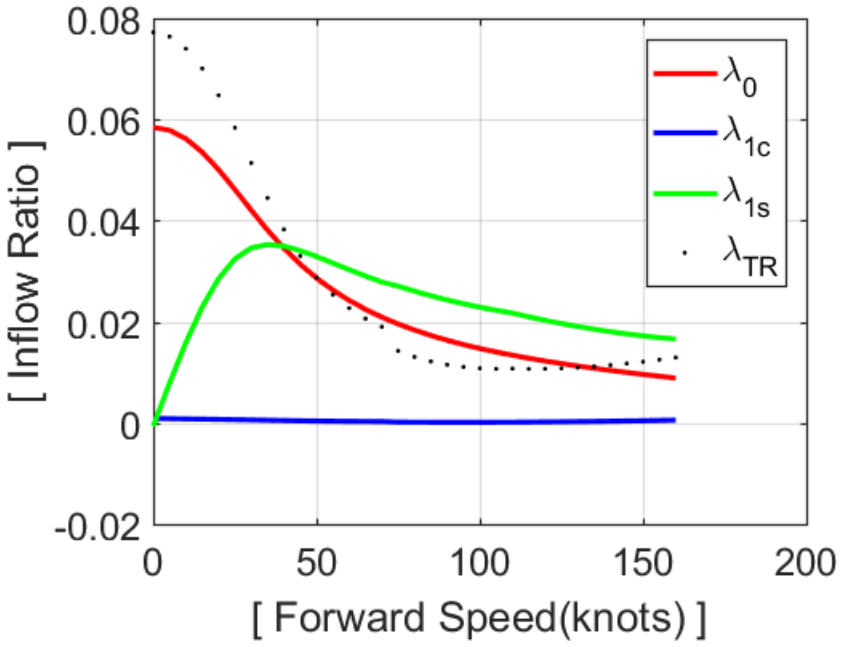

Figure 3.7: Inflow Ratio vs. Forward Flight Speed (16,000 lbs at 5,250 feet)

Figure 3.7 shows the trim values of inflow ratios at various forward speed. Dividing inflow velocities which are perpendicular to TPP by rotor tip speed, inflow ratios can be calculated. The main rotor inflow ratios are obtained by using the Pitt-peter linear inflow dynamic model. Tail rotor inflow ratio is obtained by assuming an uniform inflow due to its relatively small contribution to the entire system. λ_o is the mean part of the main rotor inflow ratio which is independent from time or blade azimuth. λ_{1c} is the longitudinal main rotor inflow ratio. λ_{1s} is the lateral main rotor inflow ratio. λ_{TR} is the tail rotor uniform inflow ratio. In addition, corresponding control inputs are also validated with flight test data in the following figures.

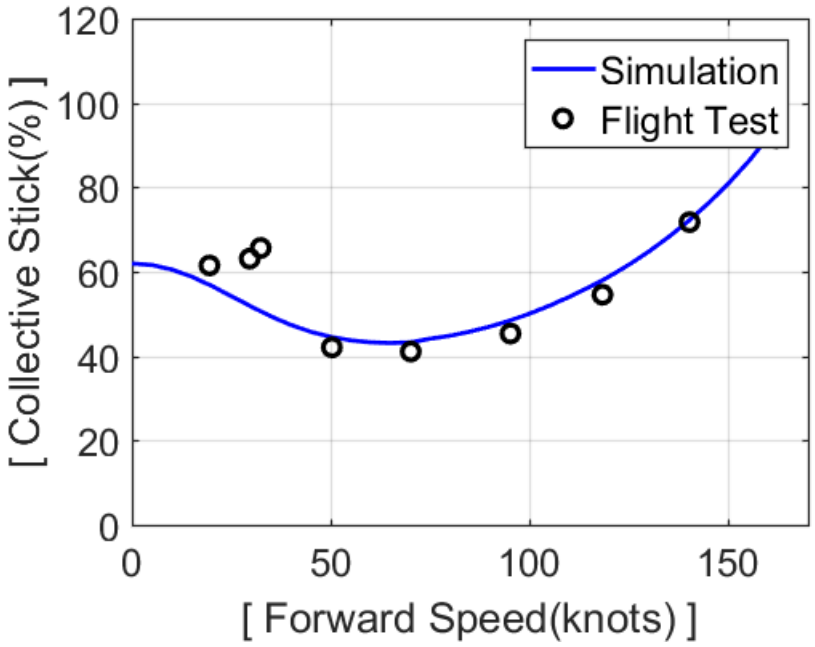

Figure 3.8: Collective Stick vs. Forward Flight Speed (16,000 lbs at 5,250 feet)

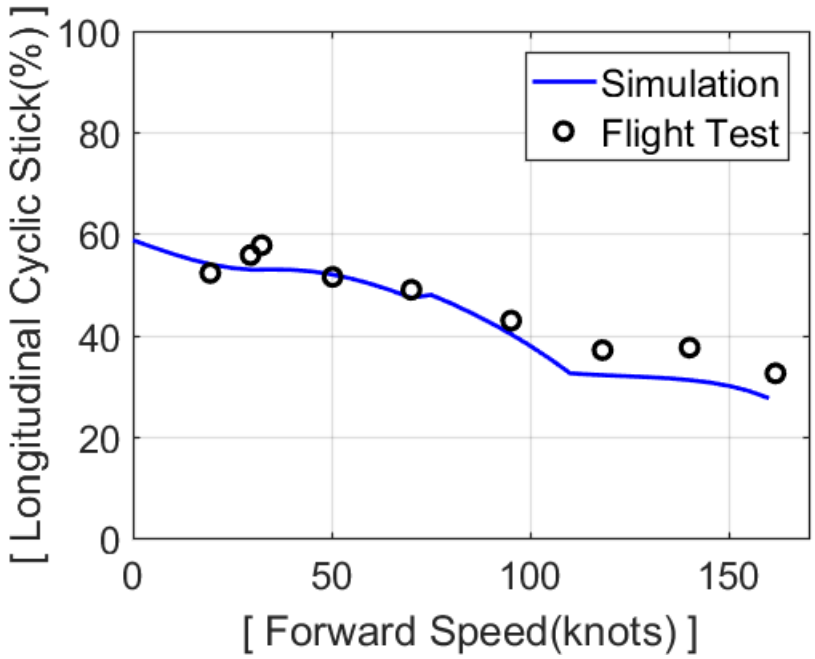

Figure 3.9: Longitudinal Cyclic vs. Forward Flight Speed (16,000 lbs at 5,250 feet)

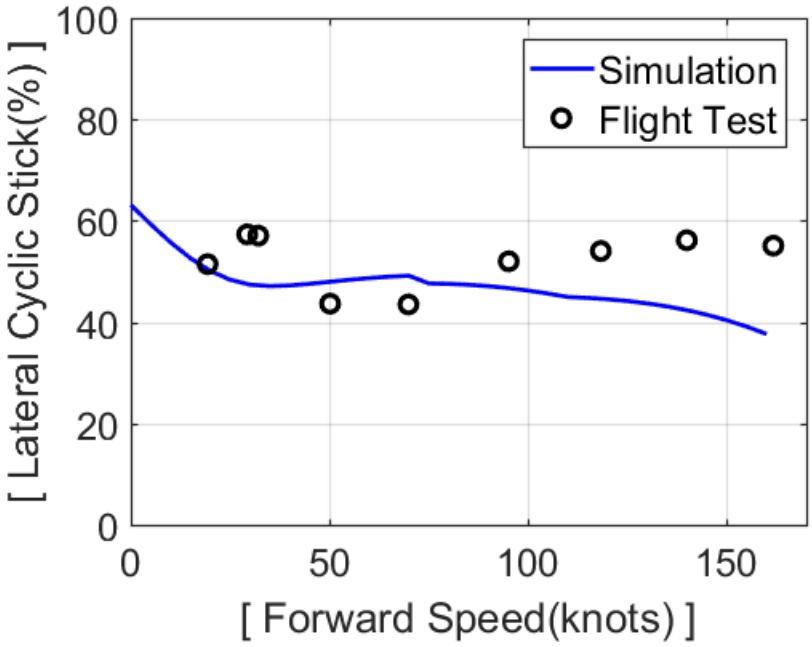

Figure 3.10: Lateral Cyclic vs. Forward Flight Speed (16,000 lbs at 5,250 feet)

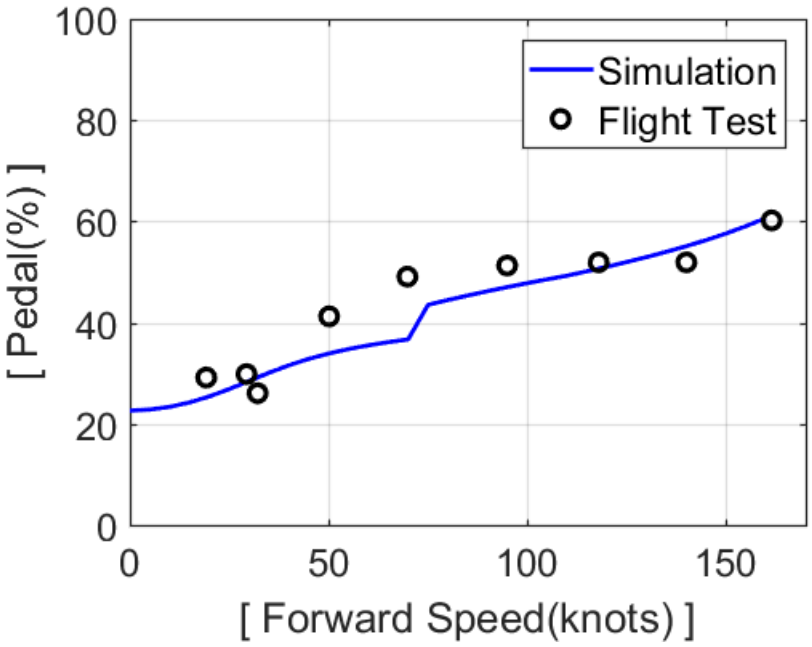

Figure 3.11: Pedal vs. Forward Flight Speed (16,000 lbs at 5,250 feet)

The comparison of predicted (simulated) four control inputs with flight test data are presented in Figure 3.8, 3.9, 3.10, and 3.11. The results have good agreement with the flight test data.

3.1.2 TRIM IN CLIMBING AND DESCENDING FLIGHT

In climbing and descending flight, it is also simulated with a gross weight of 16,000 lbs at an altitude of 5,250 feet. The following results are investigated with 60 knots forward flight speed at the flight path angle range from -20° to 25°.

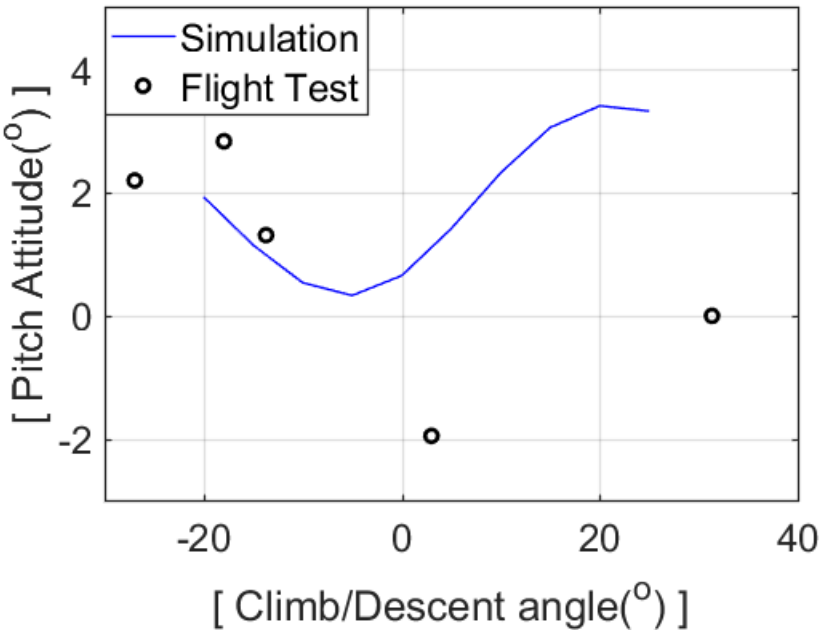

Figure 3.12: Fuselage Pitch Angle vs. Climb/Descent Angle (16,000 lbs at 5,250 feet)

Figure 3.12 shows fuselage pitch angle along the flight path (climb and descent) angle. Considering the tendency and magnitude, the prediction (simulation) is still in the reasonable range. It is also hard to investigate in this case since flight test data has only 5 data points.

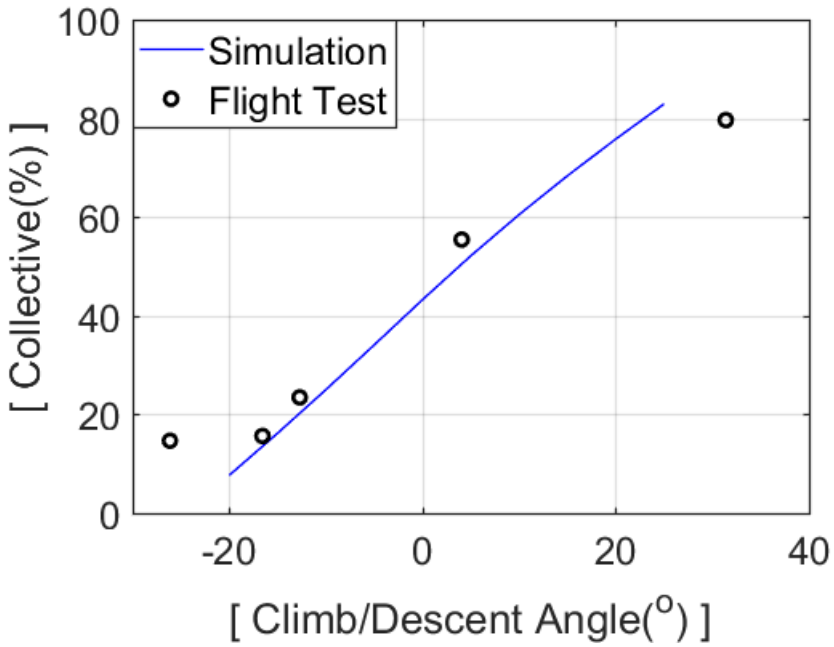

Figure 3.13: Collective Stick vs. Climb/Descent Angle (16,000 lbs at 5,250 feet)

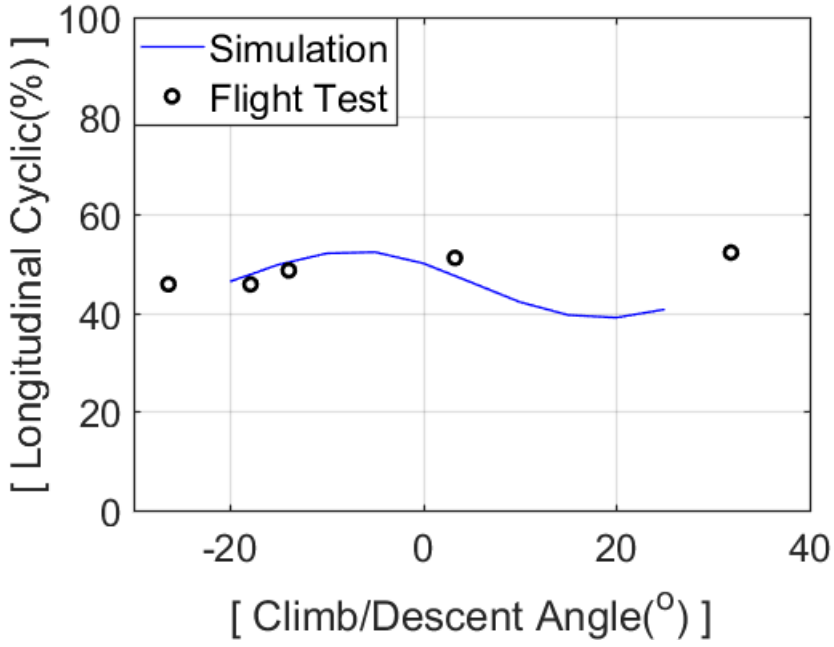

Figure 3.14: Longitudinal Cyclic vs. Climb/Descent Angle (16,000 lbs at 5,250 feet)

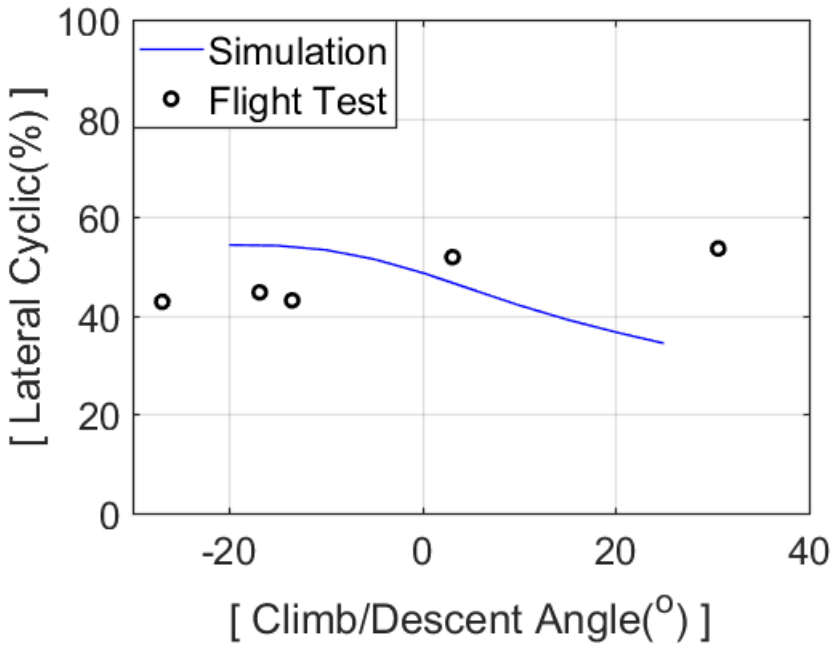

Figure 3.15: Lateral Cyclic vs. Climb/Descent Angle (16,000 lbs at 5,250 feet)

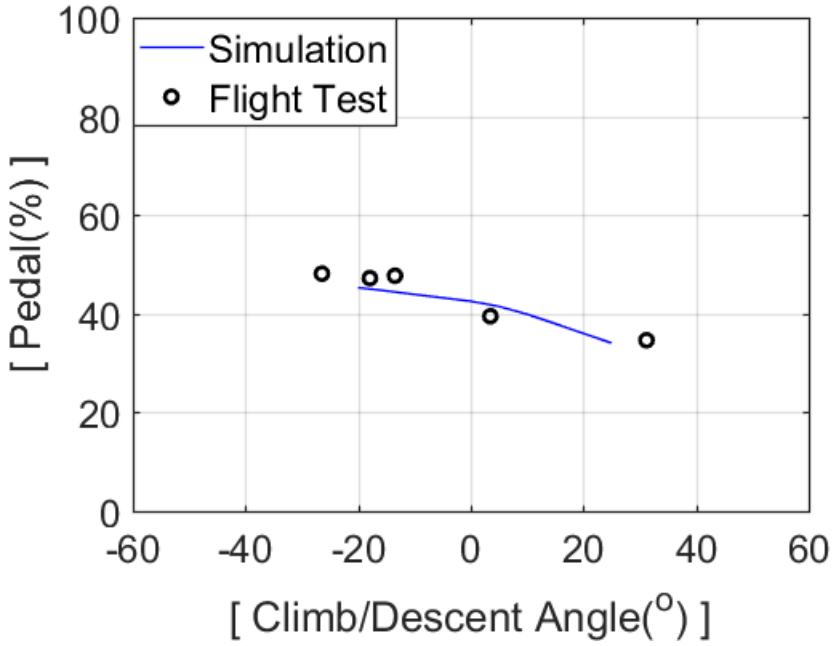

Figure 3.16: Pedal vs. Climb/Descent Angle (16,000 lbs at 5,250 feet)

The comparison of predicted (simulated) four control inputs with flight test data are presented in Figure 3.13, 3.14, 3.15, and 3.16. The results have good agreement with the flight test data.

3.1.3 TRIM IN STEADY TURNING FLIGHT

In turning flight, the turn rate is nonzero. Since flight test data are obtained with respect to the roll angle, the relation between the turn rate and roll angle is investigated first. Steady turning is also simulated with a gross weight of 16,000 lbs at an altitude of 5,250 feet. The range of turn rates is from -25 to 25 ($^\circ/sec$).

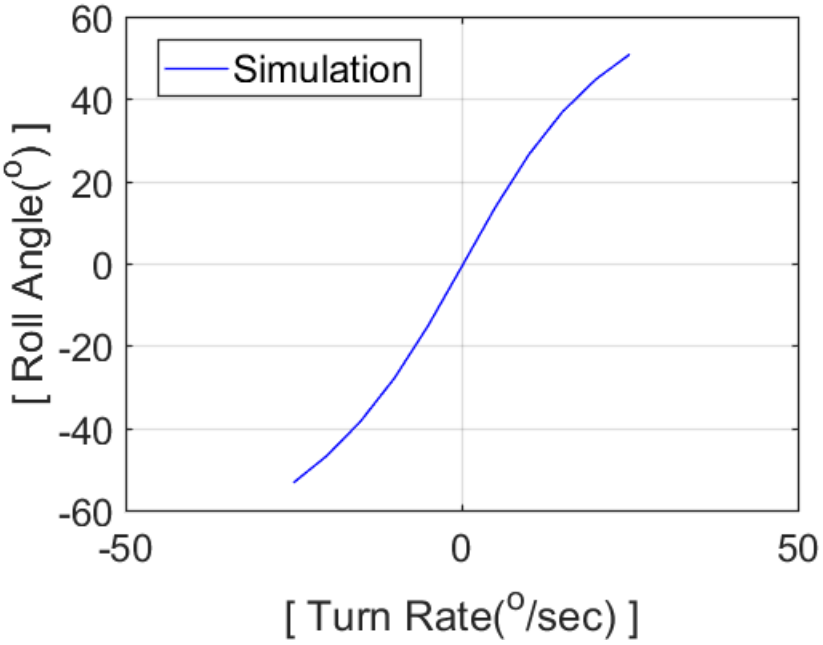

Figure 3.17: Fuselage Roll Angle vs. Turn Rate (16,000 lbs at 5,250 feet)

Fuselage roll angles corresponding to the turn rates are investigated in Figure 3.17. By doing so, it can relate fuselage pitch angels and control inputs to fuselage roll angles. The flight test data also exists as a function of roll angles, so that the comparison results in the following plots.

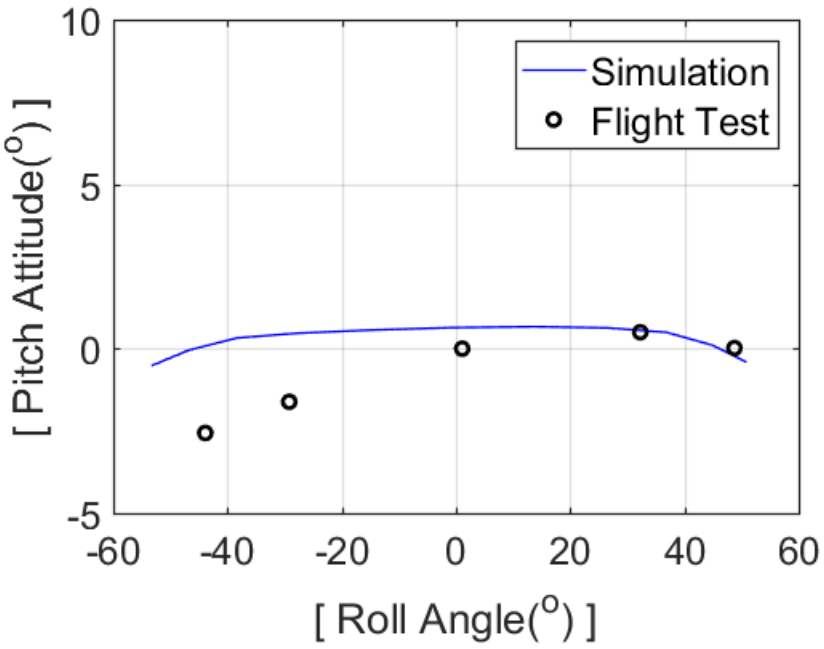

Figure 3.18: Fuselage Pitch Angle vs. Turn Rate (16,000 lbs at 5,250 feet)

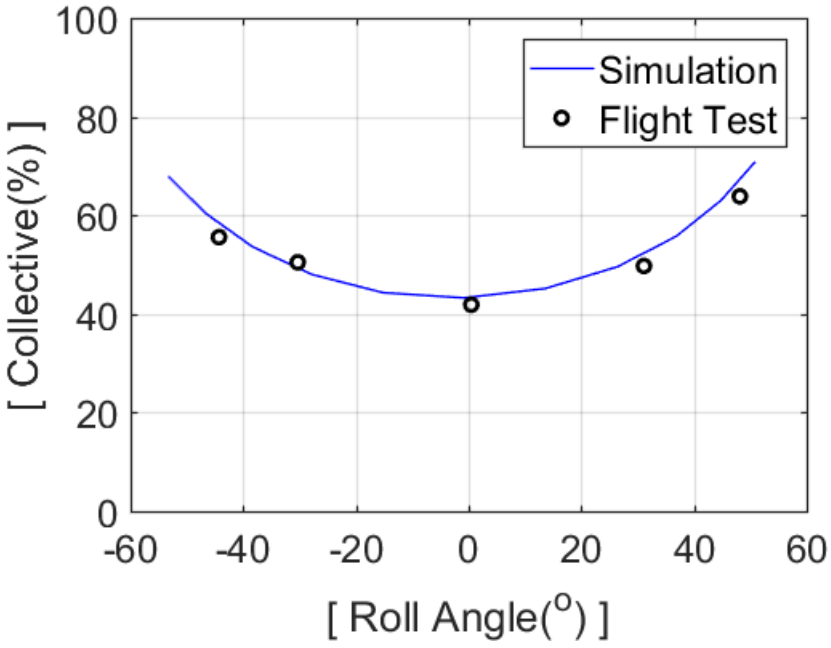

Figure 3.19: Collective Stick vs. Roll Angle (16,000 lbs at 5,250 feet)

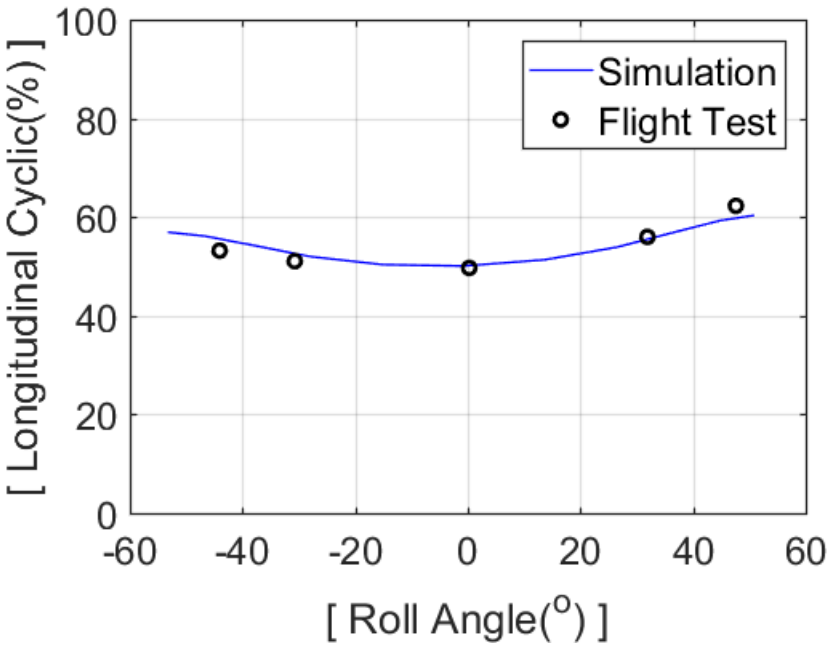

Figure 3.20: Longitudinal Cyclic vs. Roll Angle (16,000 lbs at 5,250 feet)

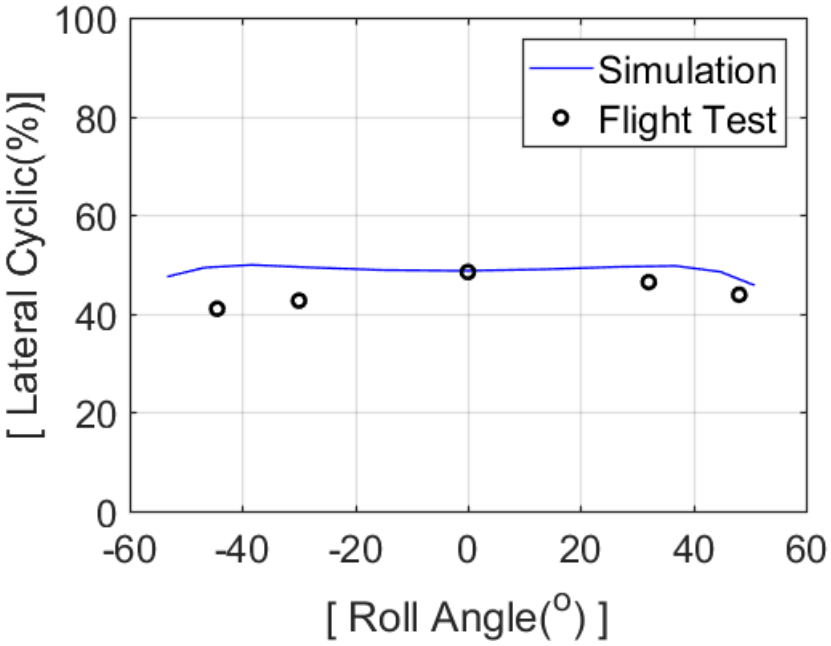

Figure 3.21: Lateral Cyclic vs. Roll Angle (16,000 lbs at 5,250 feet)

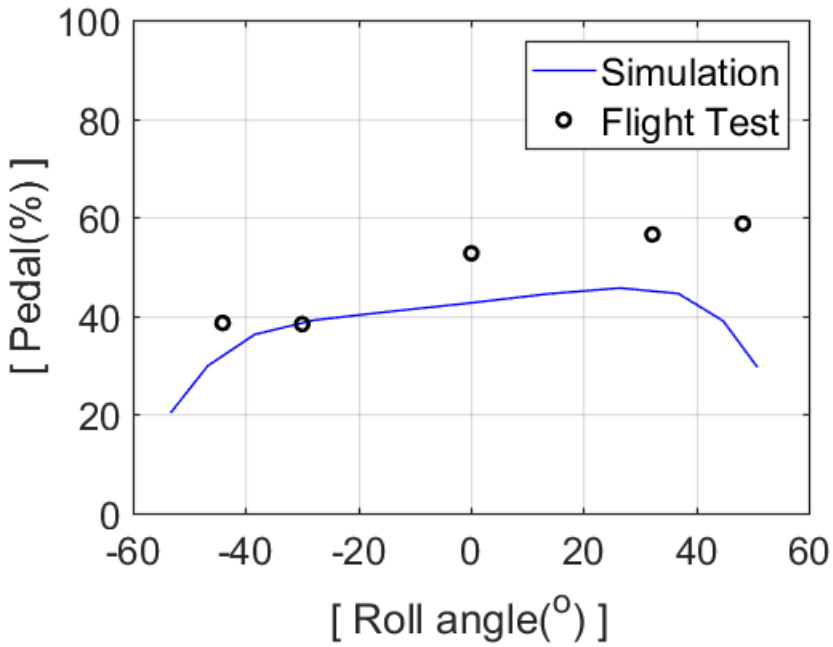

Figure 3.22: Pedal vs. Roll Angle (16,000 lbs at 5,250 feet)

Figure 3.18, 3.19, 3.20, 3.21, and 3.22 show good agreement between the prediction (simulation) and flight test data.

3.2 LINEARIZED MODEL EXTRACTION

A linearized model is extracted based on a first-order Taylor series expansion of the nonlinear system about an equilibrium (trim) point. By expanding the left hand side of the Eqn. 2.1 in a Taylor series, it yields

$$f \quad + \quad \frac{\partial f}{\partial \dot{y}}\Delta\dot{y} \quad + \quad \frac{\partial f}{\partial y}\Delta y \quad + \quad \frac{\partial f}{\partial u}\Delta u \quad + \quad \cdots \quad = \quad \epsilon \tag{3.1}$$

At equilibrium(f = $\epsilon \stackrel{def}{=} 0$), the Jacobian matrices are

$$E = \frac{\partial \epsilon}{\partial \dot{y}}\Big|_{trim}, \qquad F = \frac{\partial \epsilon}{\partial y}\Big|_{trim}, \qquad G = \frac{\partial \epsilon}{\partial u}\Big|_{trim}$$

Neglecting the higher-order terms, it yields the linearized system dynamics about equilibrium as

$$E\Delta\dot{y} \quad + \quad F\Delta y \quad + \quad G\Delta u \quad = \quad 0$$

By rearranging the above equation with respect to $\Delta\dot{y}$, it yields

$$\begin{aligned} \Delta\dot{y} \quad &= \quad A\Delta y \quad + \quad B\Delta u \\ A \quad &= \quad -E^{-1}F \\ B \quad &= \quad -E^{-1}G \end{aligned} \tag{3.2}$$

A and B matrix are extracted at a given flight condition which defines the specific model(i.e. 60 knots forward flight model). By using Eqn. 3.2 and a state-to-output conversion matrix C, transfer functions between pilot inputs and system outputs for the relevant physical quantities can be constructed as

$$H(s) \quad = \quad C(sI \quad - \quad A)^{-1}B \quad + \quad D$$

D matrix represents the direct influence of the inputs on the outputs. The nature of the aerodynamics and rotor dynamics introduces time delays between application of input and establishment of steady-state response. The control inputs influence the force distributions over the rotor disks, modifying the rotor and airframe accelerations. These accelerations, integrated over time, manifest as changes in the positions and velocities which are the system states and outputs. Therefore, the matrix D is identically zero.

4. CONTROL SYSTEM DESIGN

This chapter describes the vision-based navigation algorithm and the trajectory tracking Linear Quadratic Regulator (LQR) control system. The objective of this method is to automate the current helicopter landing procedures which are reliable and already proven. By using this method, human errors may occur during landing on a ship are effectively removed. In addition, this method covers entire ship landing maneuvers from approach to landing on a ship.

4.1 VISION-BASED NAVIGATION

This section explains how to process the images from the camera to acquire the desired data, how to calculate the relative position of the aircraft, and how to generate the trajectory. In order to maintain mission completeness, the autonomous ship landing method has to be fully operational under the GPS-denied environment. Particularly, there is a high chance that GPS is jammed during military operations. Hence, vision-based navigation is proposed to make an approach and landing on a ship without using GPS at all. A camera, gyro-stabilized horizon bar on a ship, and radar altimeter are required to implement the vision-based navigation system. A camera which is attached to the nose of the helicopter and able to rotate rotate with respect to vertical and horizontal axis. A gyro-stabilized horizon bar is the key equipment which is equipped with most modern navy ships. It is one of the three mandatory equipment for helicopter operations on a ship which is enacted by the North Atlantic Treaty Organization (NATO). A radar altimeter is used as a primary sensor to measure helicopter altitude.

4.1.1 DETECTION AND POSITIONING

In this section, the methodology to sort out a desired information from an image, and relative positioning algorithm are described. External camera is attached to the nose of a helicopter and it can rotate with respect to vertical and horizontal axis. There are lots of cameras available for this purpose and it does not need to be limited for a certain camera, however, an example camera in this study has characteristics of compactness, modifiability to Infrared Radiation (IR) camera,

and linear view mode. More specifically, its compactness allows a camera to fit with a bracket and to be placed at a desired position easily. The modifiability to IR camera enables this method to be effective even by using IR lights. The linear view mode corrects for the fisheye distortion of camera lenses. It straightens horizons and verticals and narrows the perspective. It makes the algorithm simple due to the straightforward calculation of length per pixel.

In the beginning, a helicopter is flying steady forward at 30 knots, 0.5 nm away from a ship position, and initial altitude is 200 ft. A ship is moving forward at 10 knots. This initial flight condition simulates an usual missed approach point (MAP) closely. The lateral direction of the camera is aligned with the ship's course and longitudinal direction maintains the horizon in the earth-fixed frame. The gyro-stabilized horizon bar is always parallel to the horizon in the earth-fixed frame regardless of ship motions.

Only information required from an image is a bar position and bar length in pixels. The horizon bar has a green light which is distinct from the background. Thus, undesired information is filtered out effectively by using RGB data of an each pixel. First, it sets a particular RGB range of interest. Second, pixels outside the range set to zero for RGB which is black. Third, pixels inside the range which are the components of the horizon bar set to 255 for RGB. Finally, it reconstructs an image with only white color bar and black color background. Customized RGB filter works well with the real picture as long as the bar is distinct from the background, however, example image is constructed and used in order to locate a ship exactly at desired initial position.

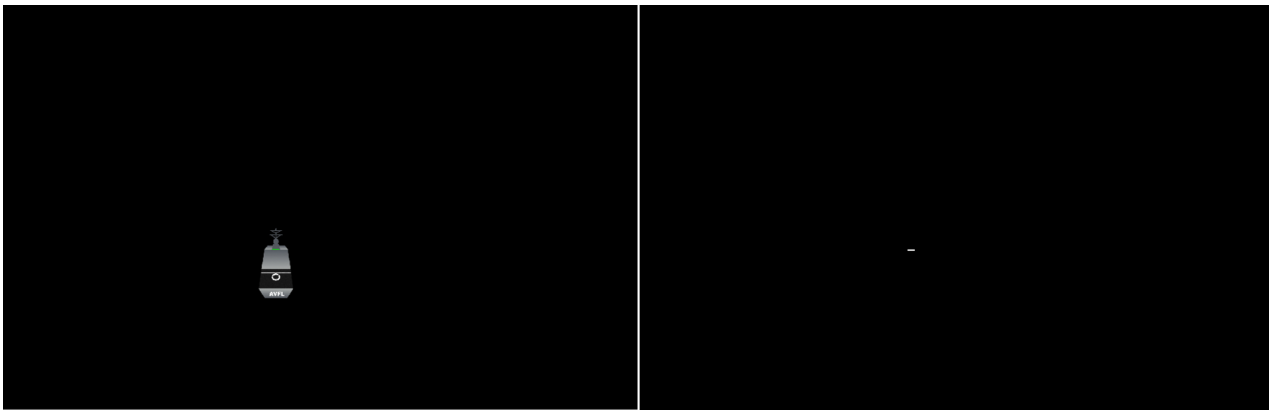

Figure 4.1: Example Ship Image(Left) and Filtered Image(Right)

From the detected image, the mid-point of the bar and the relative distance along the earth-fixed axes can be computed with the following information. The actual length of the horizon bar is known as 4 meters and the camera has a full high definition (FHD) resolution of 1920 x 1080 (width x height) pixels in a 16:9 aspect ratio. It has the horizontal angular field of view (HAFOV) of 85.5° and the vertical angular field of view (VAFOV) of 55.2°. In addition, linear view mode automatically calibrates fisheye distortion of the image, thus one pixel in the same plane which has the same distance from the camera indicates the same displacement. By using simple trigonometry and actual length per pixel, relative distance is computed by

$$\text{Length(m)/Pixel} = 4/P_d \ \text{(m/pix)}$$

$$\text{HAFOV(m)} = 1920 \times \text{Length(m)/Pixel}$$

$$\text{X(m)} = \frac{1}{2}\ \text{HAFOV(m)} \times (\tan\frac{85.5^\circ}{2})^{-1}$$

$$\text{Y(m)} = M_d \times \text{Length(m)/Pixel}$$

$$\text{Z(m)} = \text{Obtain from radar altimeter}$$

P_d is the number of pixels which belongs to the detected bar, and M_d is the number of pixels which counts from the center of horizon to the mid-point of the bar.

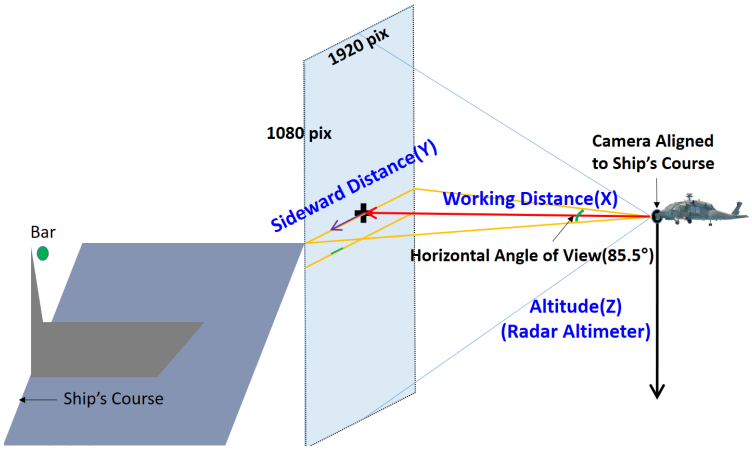

Figure 4.2: Overview of Detection and Positioning

4.1.2 TRAJECTORY GENERATION

Once a helicopter relative position from a target ship is identified, corresponding trajectory from MAP to landing is generated. The trajectory is designed to simulate real helicopter ship landing closely. It consists of several different maneuvers which are initial descent, steady forward flight, steady coordinated turn, deceleration, and final landing. UH-60 Helicopter linearized model responses with LQR control system are investigated first to determine the trajectory. They are described explicitly in the next section. The results yield the required time to complete each maneuver and the lead/lag time for the next maneuver is determined based on the required time. In this research, in order to ensure the robustness of this method, initial position is intentionally set more closer to a ship than MAP. MAP is originally defined at a point which is 926 meters (0.5 nm) away from a ship, however, initial point is at 680 meters away from a ship which is measured from the detected horizon bar image. Finally, the reference trajectory is computed. A helicopter relative position is updated periodically by the positioning algorithm and the deviation from the reference trajectory can give feedback to get back on track. In this current study, it is performed without disturbances to purely show the implementation of the proposed method.

4.2 LQR CONTROL DESIGN FOR SET-POINT TRACKING

LQR for set-point tracking method is used to track prescribed vehicle motions and obtain the control inputs required to fly a desired trajectory. In order to obtain the feedback gains K from the linearized dynamics, the Linear Quadratic Regulator (LQR) provides a methodology to stabilize and control a linear system by minimizing a quadratic cost function in the state deviations from targets and the control inputs. For an LTI system with dynamics given by Eqn. 3.2, the infinite-horizon continuous-time LQR controller yields state feedback gains K to minimize the quadratic cost function

$$J = \int_0^\infty (x^T Q x + \Delta u^T R \Delta u) dt \tag{4.1}$$

$$(\text{ where } \quad x \quad = \quad y \quad - \quad y_{target} \ )$$

Computing the steady-state values of the states and the control inputs result in zero output error and then force them to take these values. If the desired final values of the states and control inputs are x_{ss} and u_{ss} respectively, then the new control formula should be

$$\Delta u = u_{ss} - K(x - x_{ss}) \tag{4.2}$$

Plugging it in the standard form yields

$$\dot{x} = Ax + B(u_{ss} - Kx + Kx_{ss}) \tag{4.3}$$

$$y = Cx \tag{4.4}$$

when x = x_{ss}(no error), and u = u_{ss}, it is expressed as

$$O = Ax_{ss} + Bu_{ss} \tag{4.5}$$

$$y_{ss} = Cx_{ss} \tag{4.6}$$

It can be re-arranged in matrix form as

$$\begin{bmatrix} x_{ss} \\ u_{ss} \end{bmatrix} = \begin{bmatrix} A & B \\ Cs & Ds \end{bmatrix}^{-1} \begin{bmatrix} O \\ y_{ss} \end{bmatrix} \tag{4.7}$$

In order to make it feasible, the matrix consists of A, B, Cs, and Ds components has to be invertible. Hence, Cs and Ds are selected to meet the size of the matrix. In this control system, the number of rows in Cs has to be the same as the number of control inputs which is 4. In other words, it is able to give 4 non-zero reference states to track and the other states are regulated to zero at the same time.

4.3 SIMULATION RESULTS

In this section, helicopter states and the corresponding trajectory of the CG are described. The simulation is conducted for 3 minutes without disturbances. For initial conditions, a helicopter is flying forward with 30 knots at the height of 200 ft (60.96 m), and its initial position is defined as (0, 0, -60.96) in the earth-fixed frame. A target ship is moving forward with 10 knots. The horizon bar position represents the position of a target ship and its initial position is at (679.7285, -88, -5) in the earth-fixed frame. All units are in meters and in order to demonstrate the trajectory more intuitively, the sign of the Z-axis component in the earth-fixed frame is swapped in the following plots (positive upwards). In the entire trajectory plots, red marker represents the ship trajectory and blue line represents the helicopter trajectory.

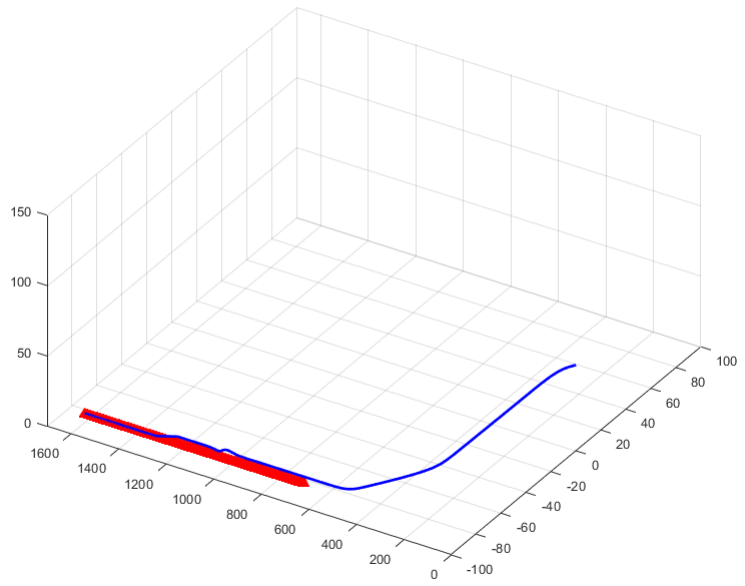

Figure 4.3: Entire Trajectory in diagonal view

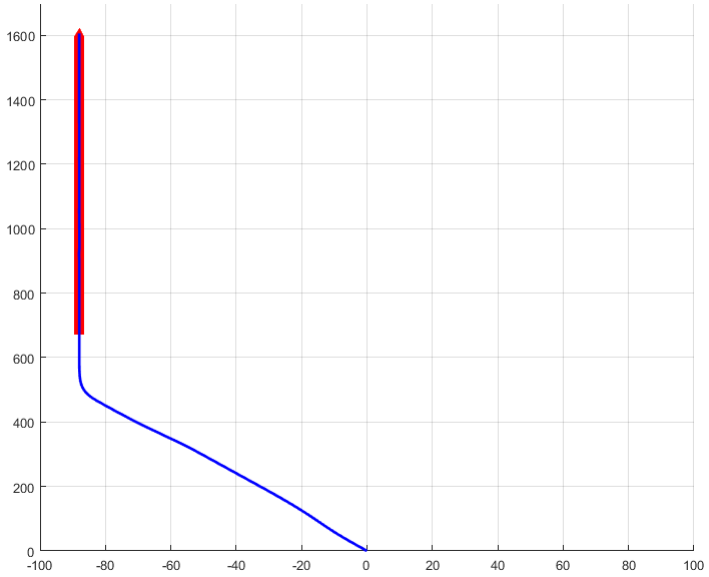

Figure 4.4: Entire Trajectory in top view

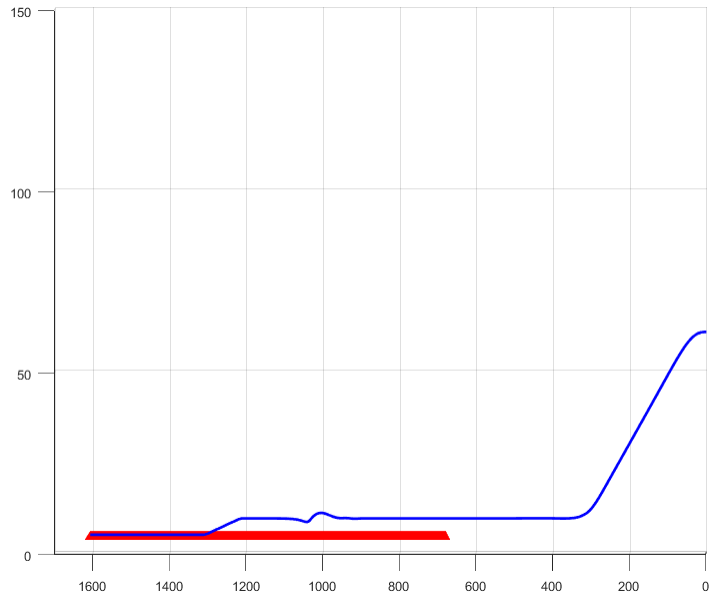

Figure 4.5: Entire Trajectory in side view

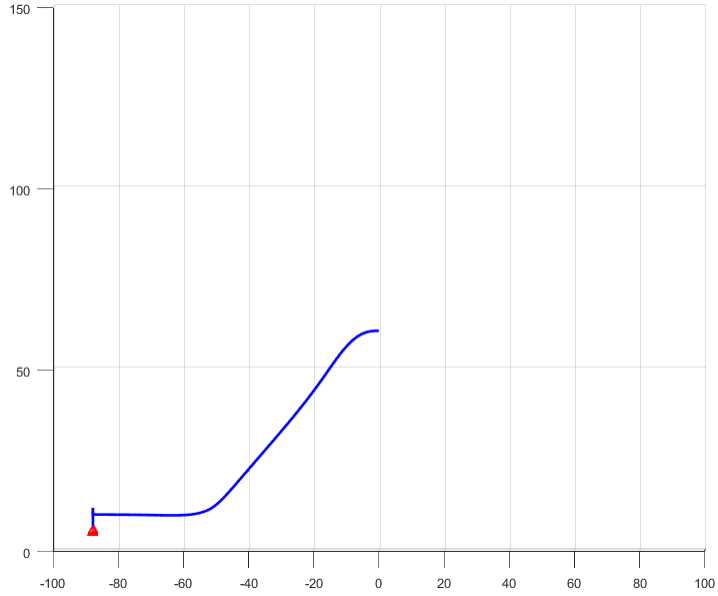

Figure 4.6: Entire Trajectory in rear view

In order to check the trajectory more specifically, relative distance in the earth-fixed frame is investigated and the final landing position is also plotted. The relative distance is calculated by "Ship position" - "Helicopter position" in the earth-fixed frame. ΔX, ΔY, and ΔZ are relative distance along the earth-fixed X, Y, Z-axis. In the following plots, the Z-axis component sign also follows re-defined direction(positive upwards). Final landing circle on a flight deck means that landing anywhere inside circle is safe. Thus, it can be considered an allowable error range. Final values of ΔX, ΔY are considered an error, but ΔZ is the summation of the distance from the landing gear to the CG (48.26 cm) and error. Hence, the final errors means the deviation from the center of the circle and are expressed along the each axis in meters (0.0353, 0.0728, 0.0037). Considering the circle boundary, it shows good enough result.

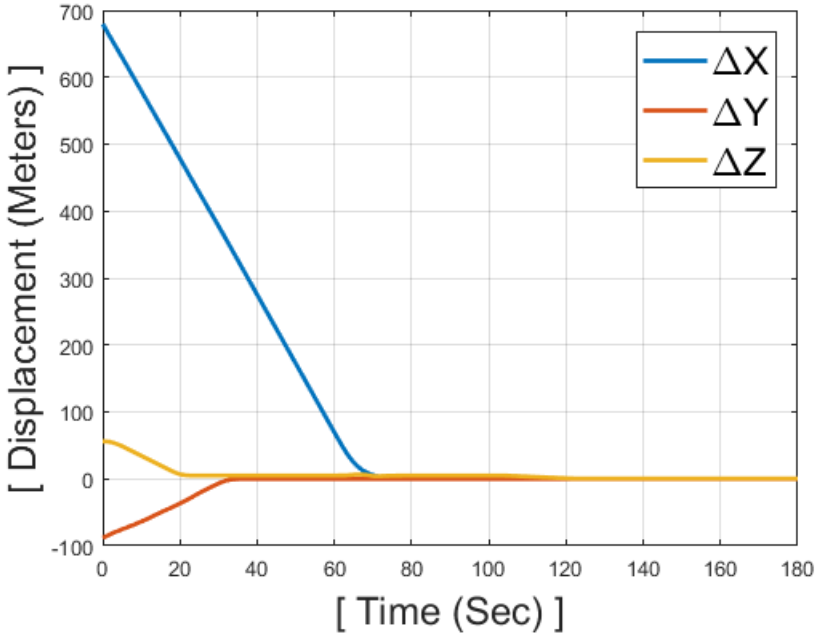

Figure 4.7: Relative Displacement in time

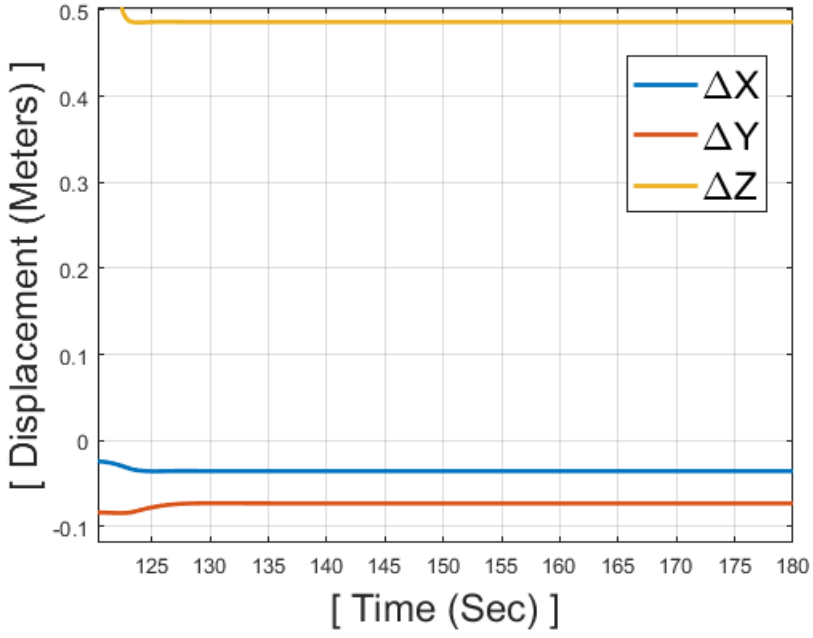

Figure 4.8: Final Relative Displacement

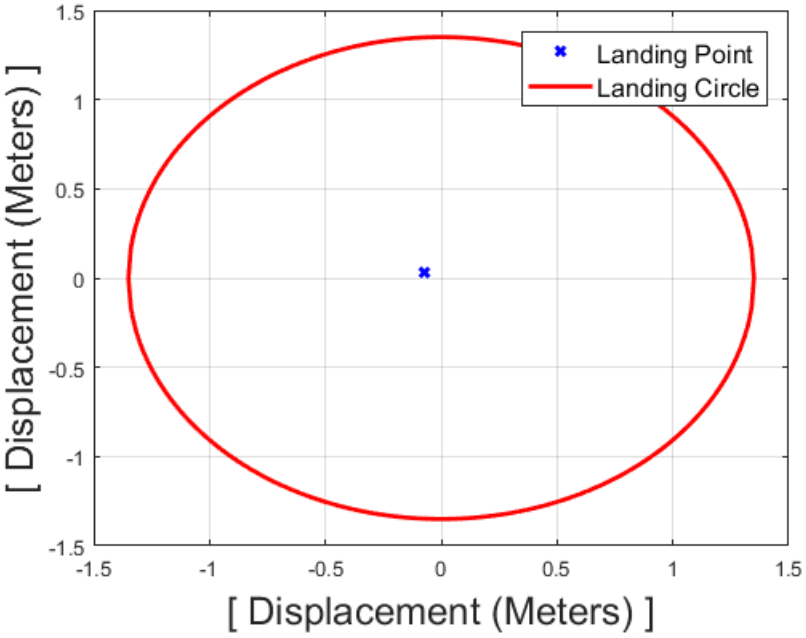

Figure 4.9: Final Landing Point

4.3.1 INITIAL DESCENT

For the initial descent maneuver, UH-60 linearized model which is extracted at forward speed of 30 knots is used. It is controlled by LQR for set-point tracking to achieve desired states. In order to descend, references to vertical speed w are assigned and the controller effectively regulates the new error which is the difference between the reference and current state. Gains for the controller are determined by changing weights on Q and R matrix. Weights are carefully chosen since there is a trade-off between transient responses and control efforts. Thus, it is required to check the control inputs are in the reasonable range. With the selected gains, it takes 41.68 seconds to regulate the errors in states less than $1e^{-05}$ and the corresponding final altitude deviation is 0.03 cm. Trajectory for descent, fuselage states in time, and relative control stick inputs (deviation from the trim control inputs) are identified as below.

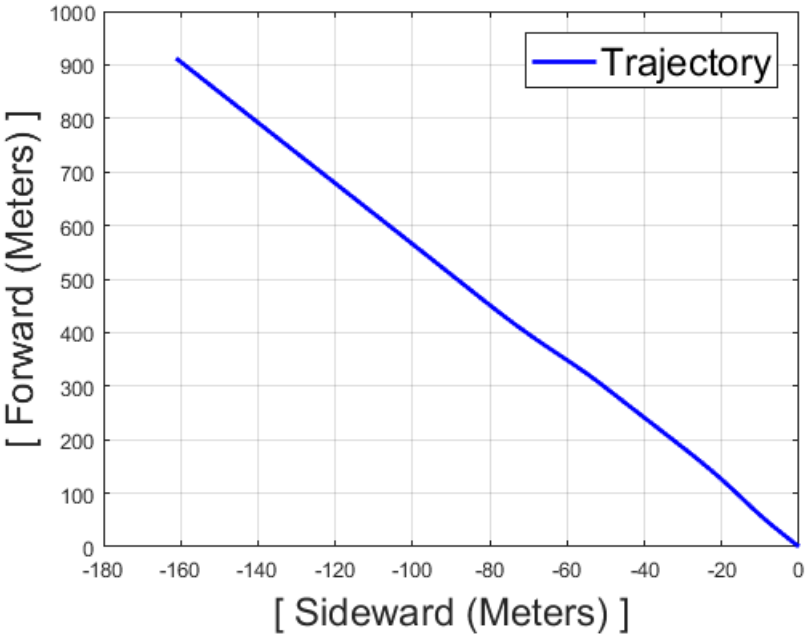

Figure 4.10: Descent Trajectory in top view

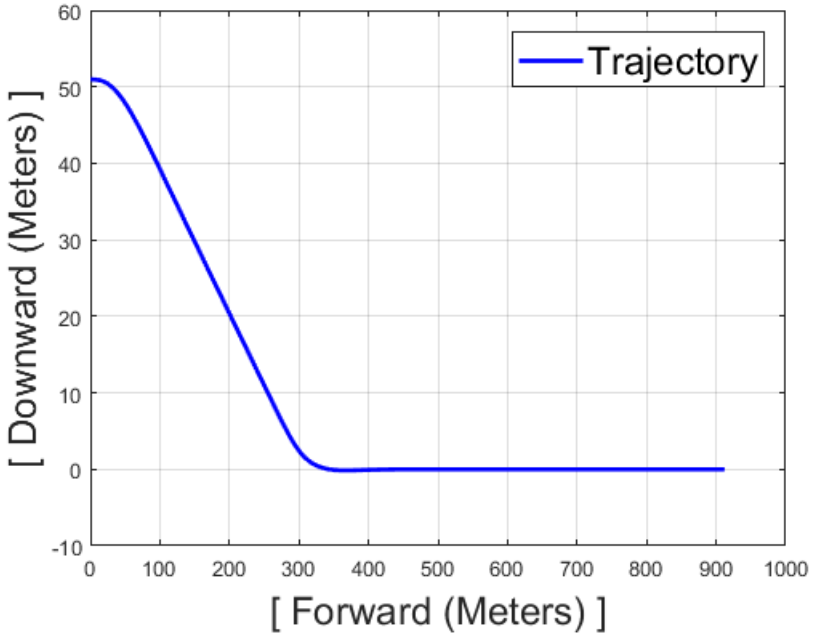

Figure 4.11: Descent Trajectory in side view

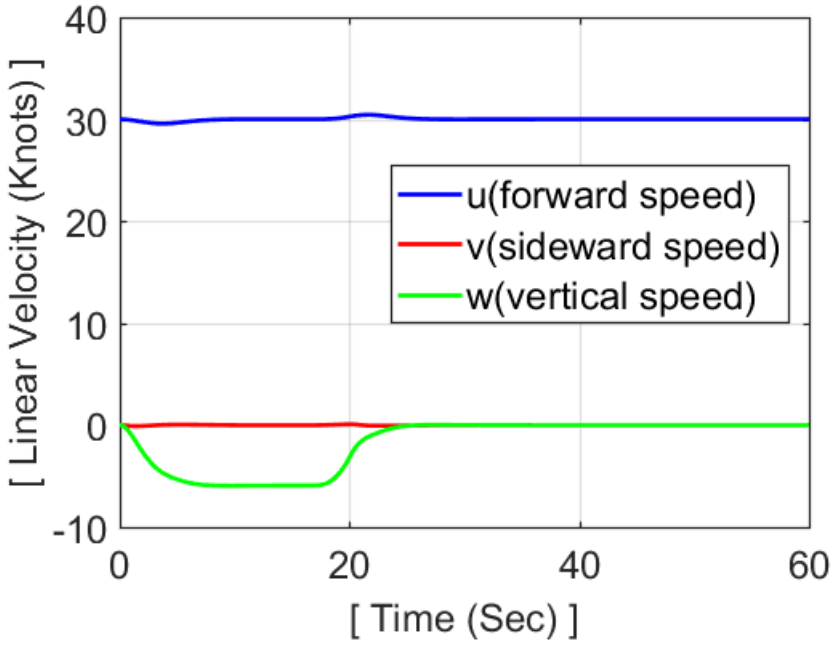

Figure 4.12: Body Axes Linear Velocity States in Descent

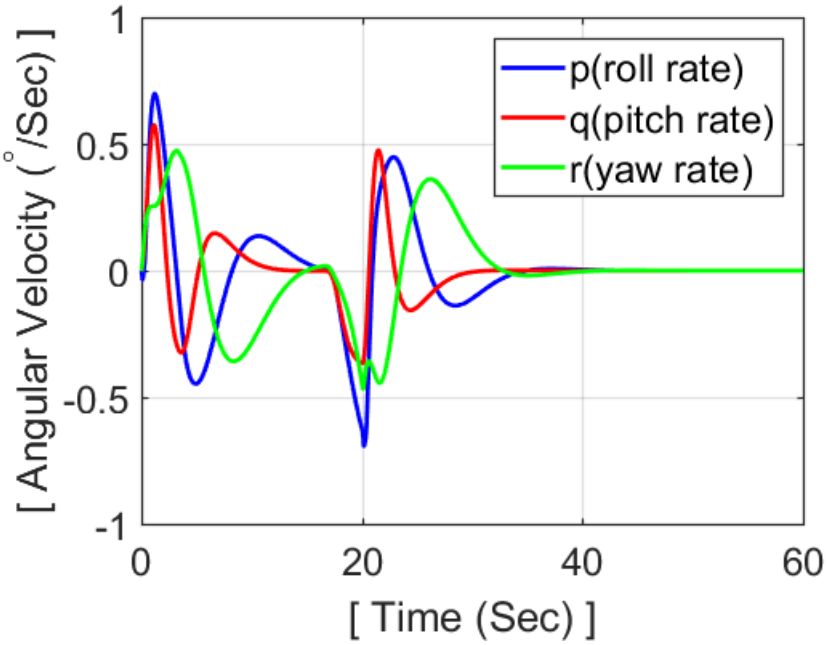

Figure 4.13: Body Axes Angular Velocity States in Descent

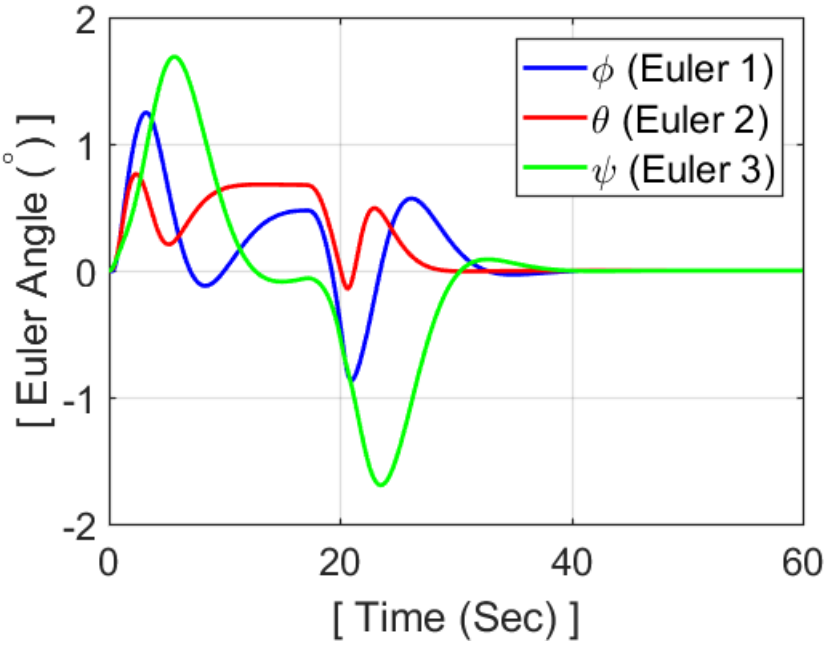

Figure 4.14: Body Axes Angular Velocity States in Descent

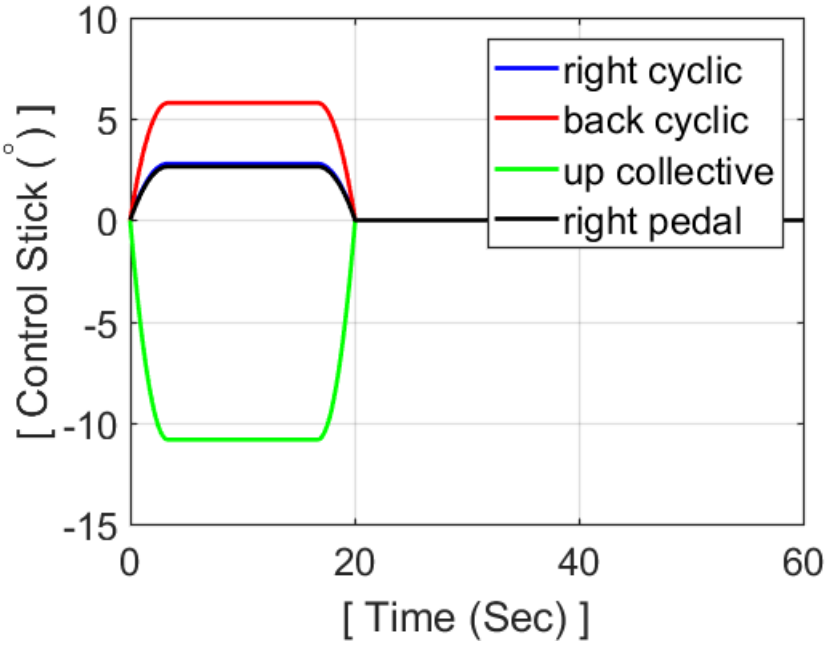

Figure 4.15: Relative Control Inputs in Descent

Considering a helicopter relative position, it starts next maneuver before it reaches the perfect settlement of states. In this case, it requires to begin the next maneuver (steady turn) at 30.14 seconds. Thus, the state values at 30.14 seconds are used as initial values for the next maneuver.

u = 15.4295 (m/s)	v = 0.0029 (m/s)	w = -0.0060 (m/s)
p = -0.0018 ($^\circ/s$)	q = -8.2214 ($^\circ/s$)	r = 0.0019 ($^\circ/s$)
ϕ = 0.0028 ($^\circ$)	θ = -9.0965 ($^\circ$)	ψ = -0.0005 ($^\circ$)

Table 4.1: State Values at 30.14 seconds

4.3.2 STEADY TURN

For the steady turn maneuver, UH-60 linearized model which is extracted at forward speed of 30 knots is used. It is controlled by LQR for set-point tracking to achieve desired states. In order to turn, references to euler angle ψ are assigned and the controller effectively regulates the new error which is the difference between the reference and current state. It takes 17.71 seconds to regulate the errors in states less than $1e^{-05}$ and the corresponding final euler angle deviation is $8.45e^{-07}(^{\circ})$ which is near zero. According to this simulation, the displacement along the earth-fixed Y-axis is computed by -6.6817 meters. From this, the lead time to start the steady turn maneuver can be calculated. Considering the lead time, the turning maneuver begins 30.14 seconds after the start of descent. Corresponding steady turn trajectory, fuselage states in time, and relative control stick inputs are identified as below.

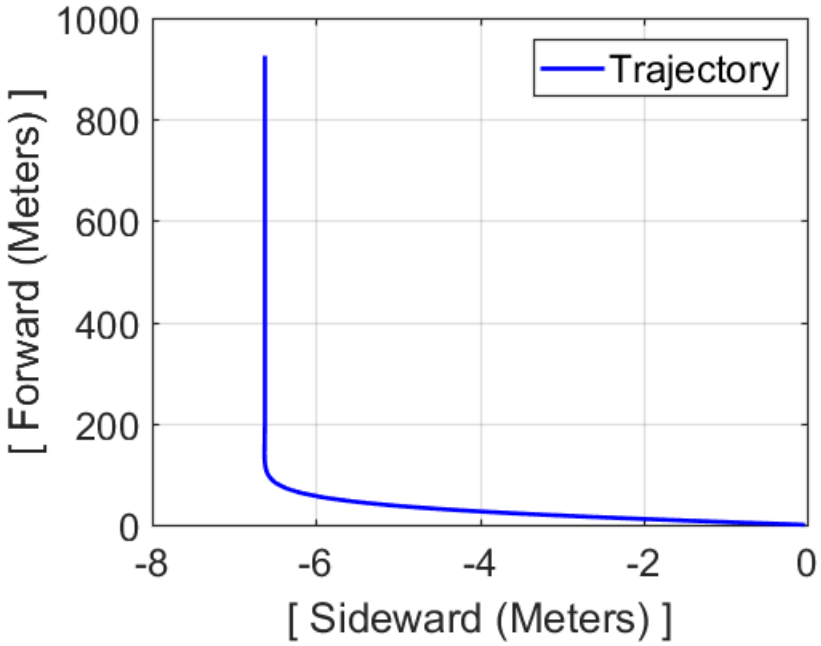

Figure 4.16: Steady Turn Trajectory in top view

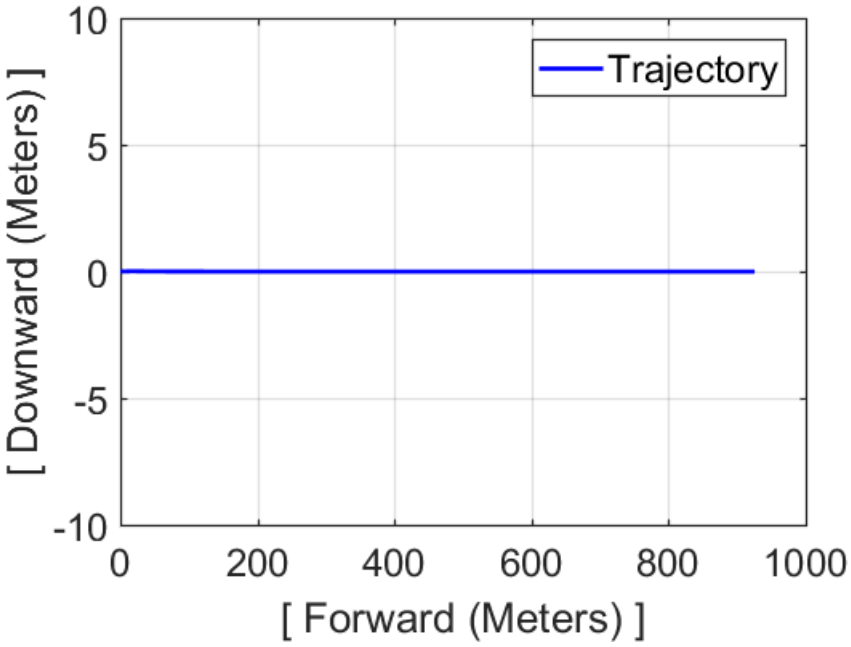

Figure 4.17: Steady Turn Trajectory in side view

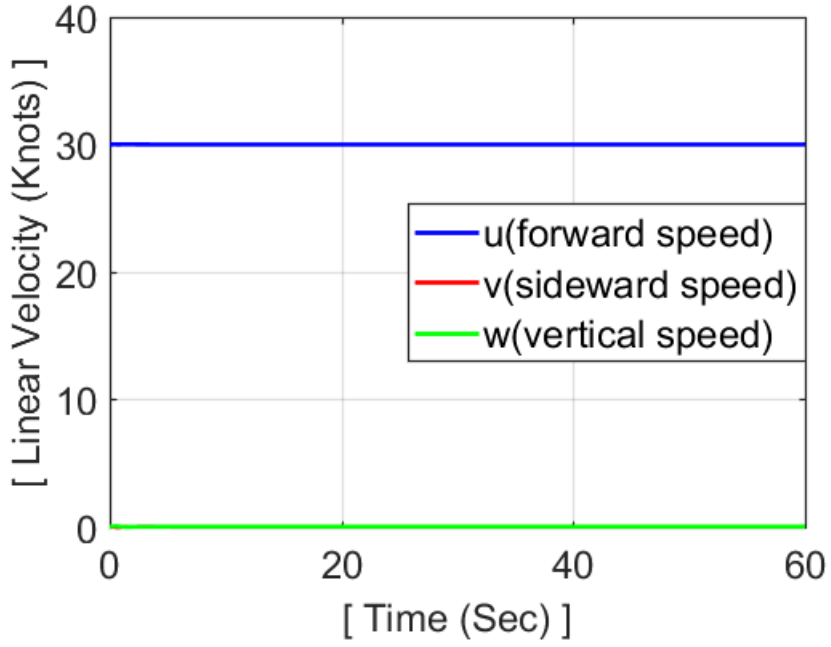

Figure 4.18: Body Axes Linear Velocity States in Steady Turn

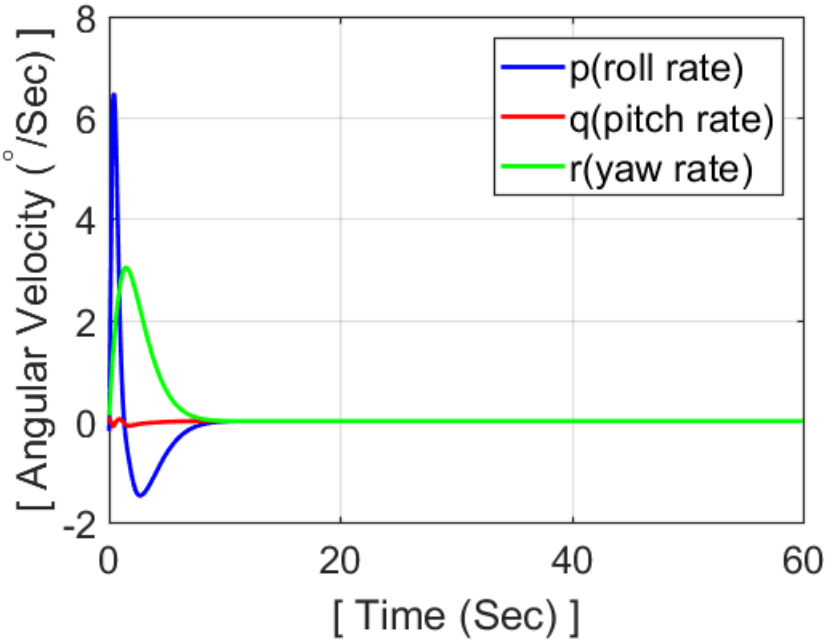

Figure 4.19: Body Axes Angular Velocity States in Steady Turn

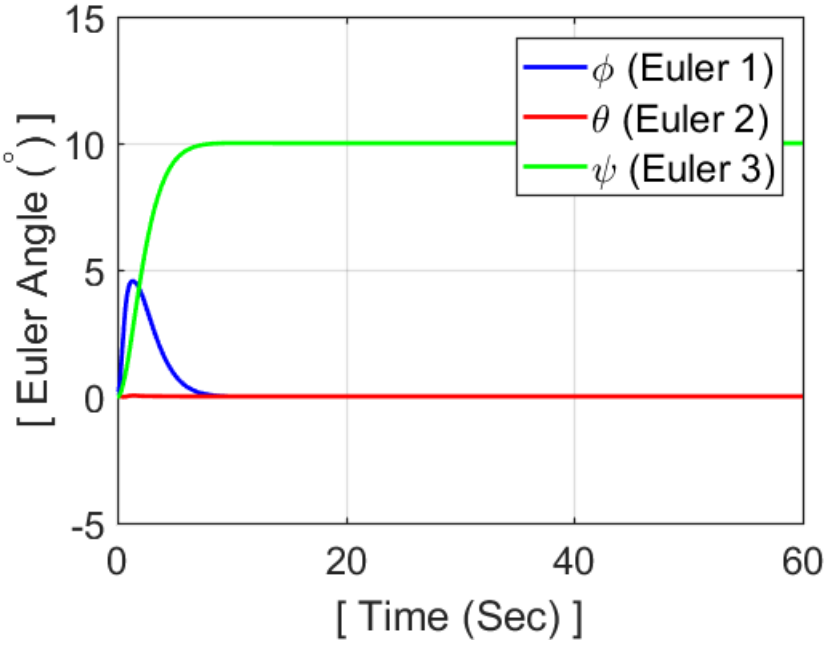

Figure 4.20: Euler Angle States in Steady Turn

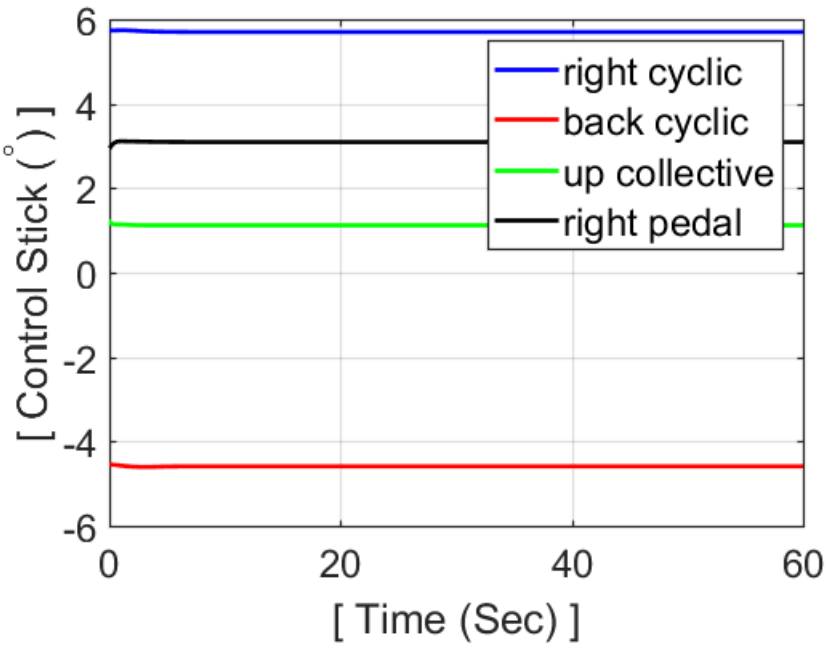

Figure 4.21: Relative Control Inputs in Steady Turn

4.3.3 DECELERATION

For the deceleration maneuver, UH-60 linearized model which is extracted at forward speed of 10 knots is used. First, initial 20 knots headwind is applied to simulate the deceleration from 30 knots to 10 knots. Although it has no problem to regulate all states, a helicopter gains undesired altitude which is 14.78 meters. It occurs due to the typical way that a helicopter decelerates. In order to decelerate a forward speed, a helicopter has to change its pitch (nose up). By doing so, the thrust vector which is perpendicular to TPP tilts back, and it decreases the forward direction component of the thrust vector, which leads to the deceleration in forward speed. Hence, beside the assigning an initial value for forward speed *u*, additional references which can control the vertical displacement (altitude) is required.

In order to minimize the undesired altitude gain, references to vertical speed w are assigned in this simulation. It is controlled by LQR for set-point tracking to regulate the new errors which are the differences between references to w and the value of w at each time step. It takes 37.08 seconds to regulate the errors in states less than $1e^{-05}$. The final deviation in altitude is 0.024 cm and lateral deviation 1.691 cm. During this deceleration maneuver, maximum altitude gain is 1.5189 meters and maximum altitude loss is 0.9705 meters. References to vertical speed *w* and LQR gains are selected carefully, and realistically to minimize this variation in altitude. To locate a helicopter at desired position when it completes deceleration, this deceleration maneuver begins 28.43 seconds after the start of steady turn. Since the previous maneuver steady turn takes 17.71 seconds to achieve settlement in states, initial values for deceleration maneuver set to zero other than forward speed *u* (which simulates decelerating from 30 knots to 10 knots). Corresponding deceleration trajectory, fuselage states in time, and relative control stick inputs are identified in the following plots.

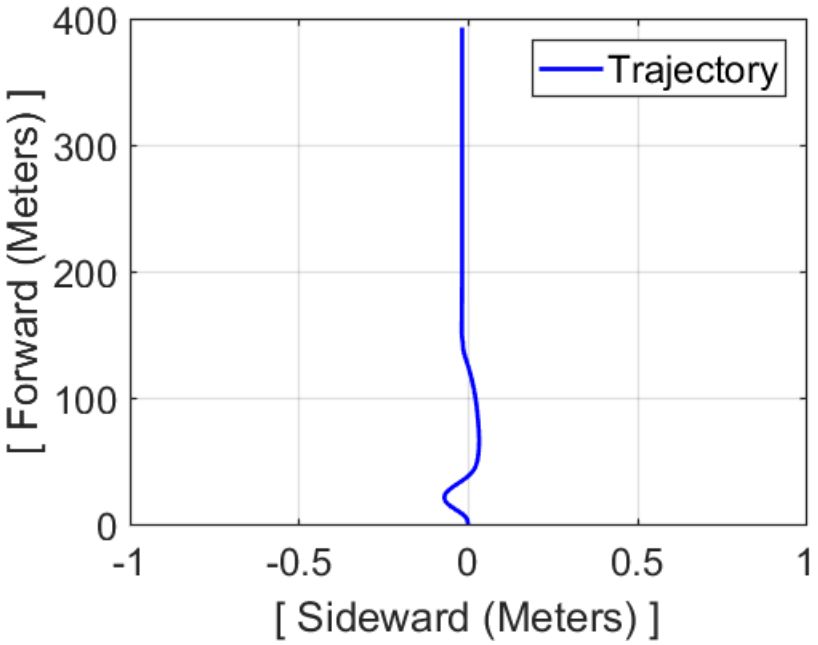

Figure 4.22: Deceleration Trajectory in top view

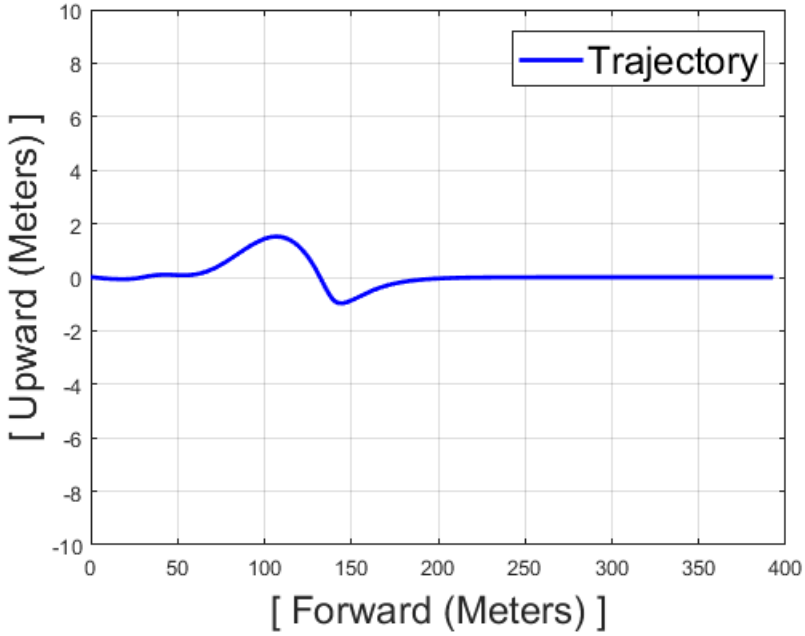

Figure 4.23: Deceleration Trajectory in side view

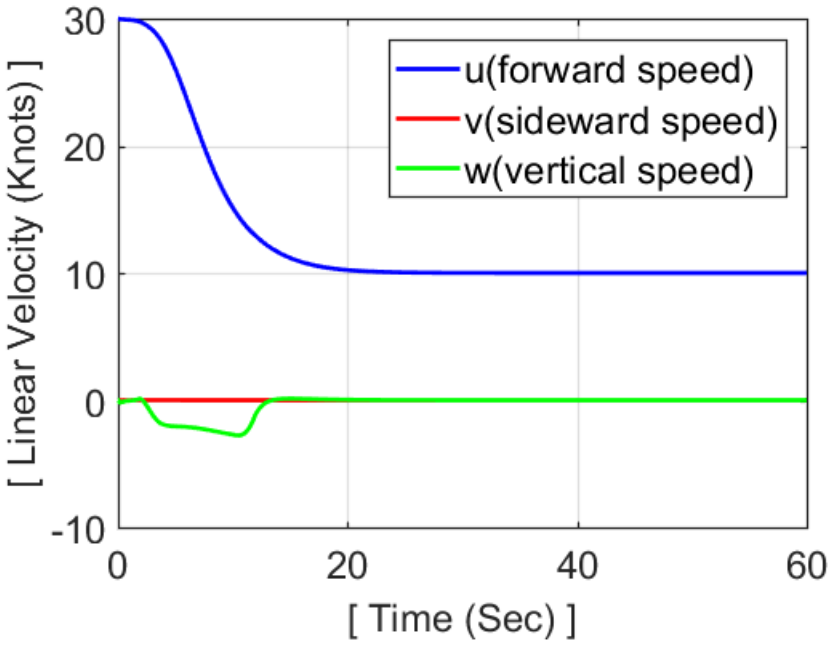

Figure 4.24: Body Axes Linear Velocity States in Deceleration

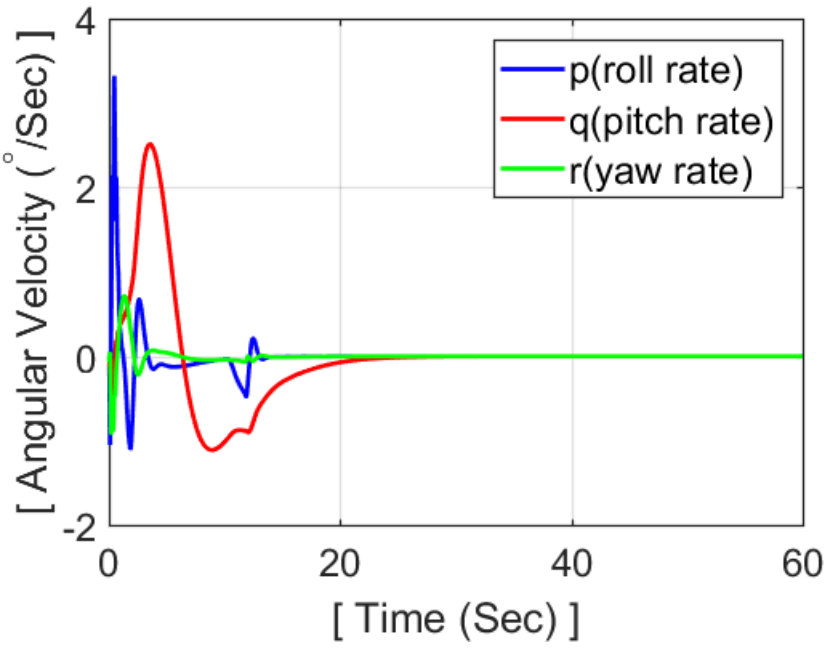

Figure 4.25: Body Axes Angular Velocity States in Deceleration

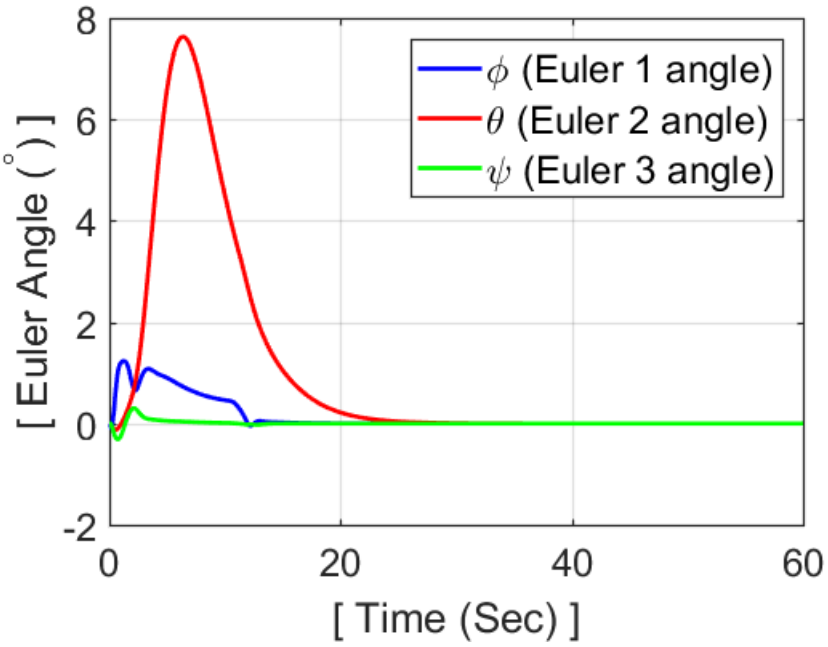

Figure 4.26: Euler Angle States in Deceleration

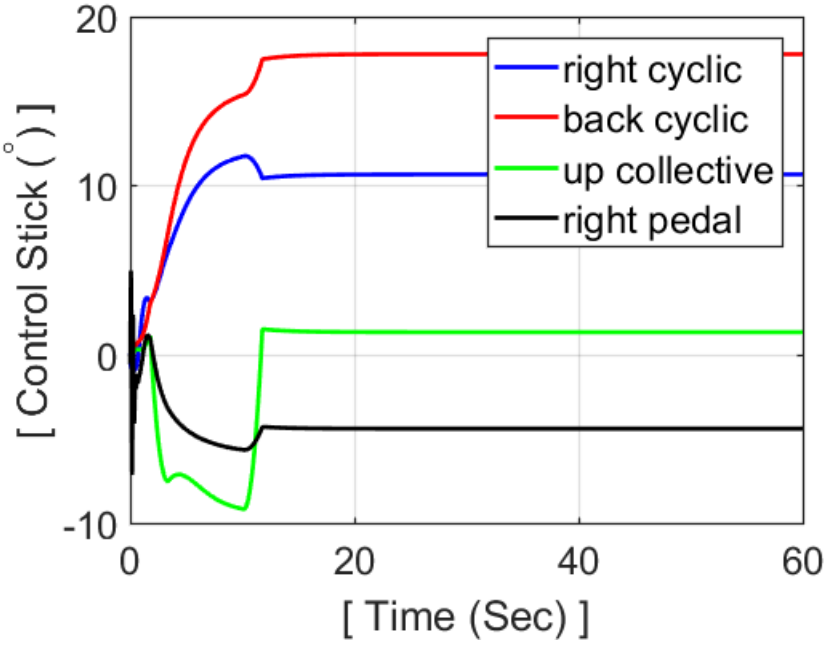

Figure 4.27: Relative Control Inputs in Deceleration

4.3.4 LANDING

For the landing maneuver, UH-60 linearized model which is extracted at forward speed of 10 knots is used. It is controlled by LQR for set-point tracking to achieve desired states. In order to land vertically, references to vertical speed w are assigned and the controller effectively regulates the new error which is the difference between the reference and current state. Although it takes 28.34 seconds to regulate the errors in states less than $1e^{-05}$, state responses after 20.41 seconds are meaningless since it touches down the deck at 20.41 seconds. In this simulation, the final landing maneuver begins 48.87 seconds after the start of deceleration. Landing gear position from the CG is considered and the final landing point deviation from the center of the landing circle is 0.0353 meters along the earth-fixed X-axis, and is 0.0728 meters along the earth-fixed Y-axis. Corresponding landing trajectory, fuselage states in time, and relative control stick inputs are identified as follows.

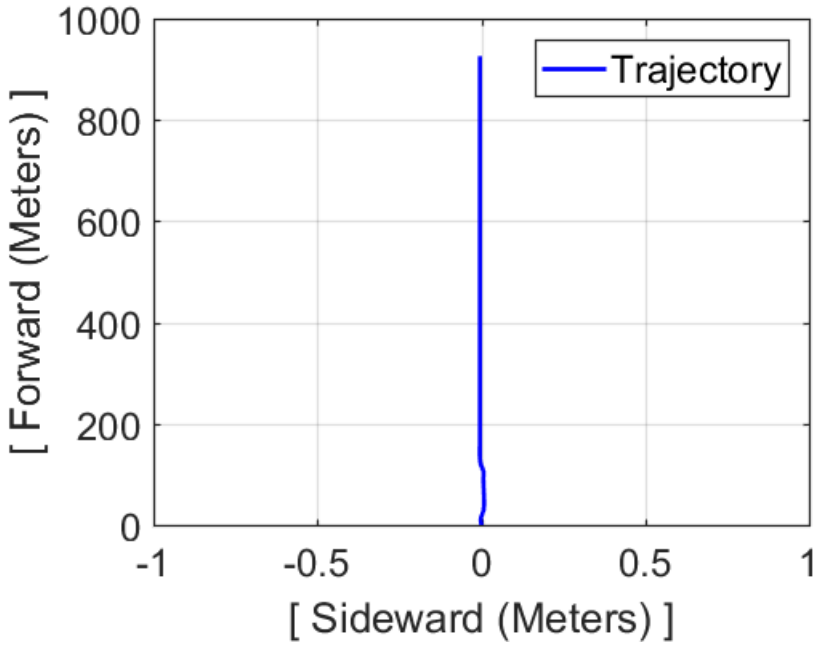

Figure 4.28: Landing Trajectory in top view

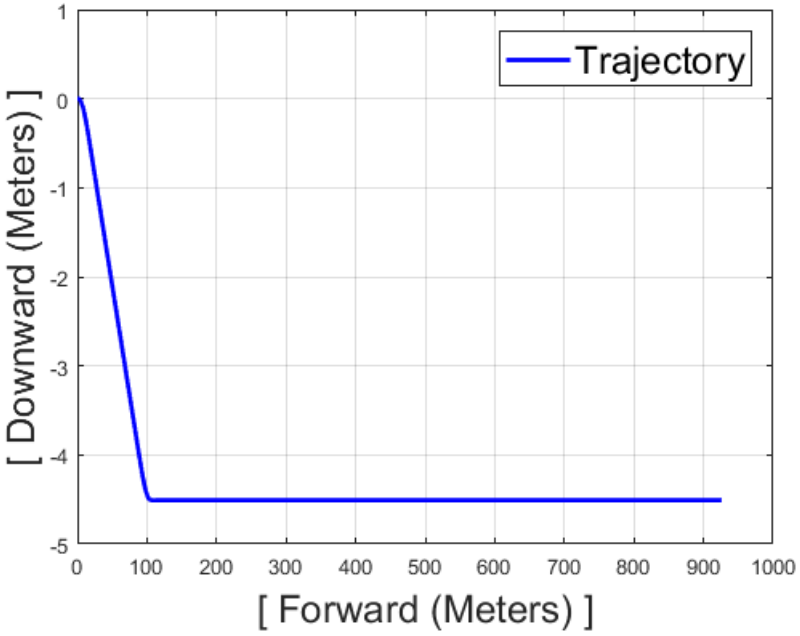

Figure 4.29: Landing Trajectory in side view

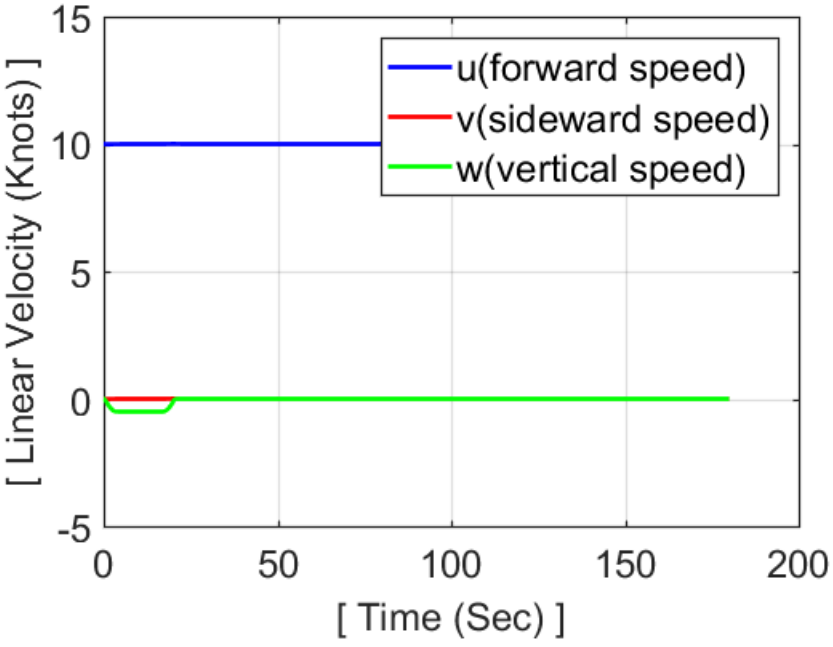

Figure 4.30: Body Axes Linear Velocity States in Landing

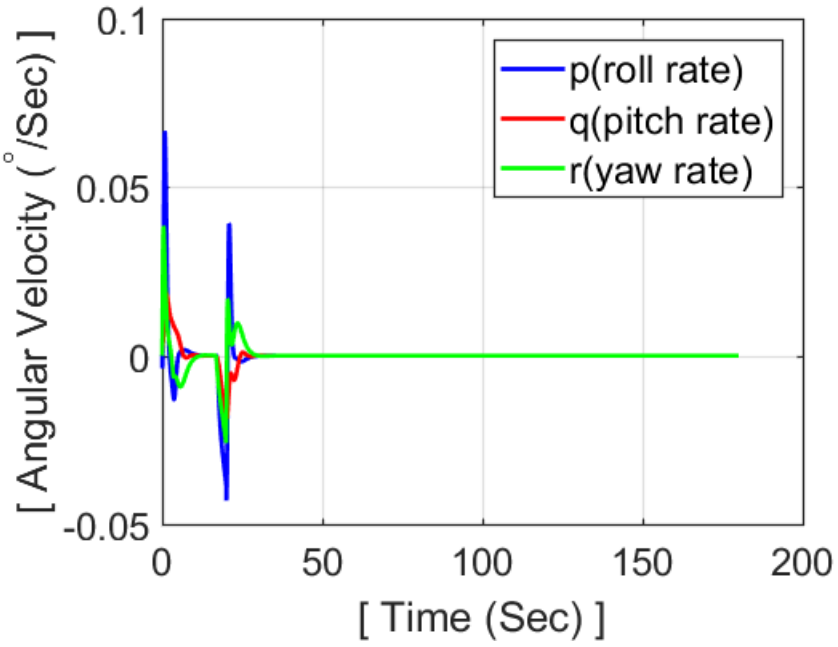

Figure 4.31: Body Axes Angular Velocity States in Landing

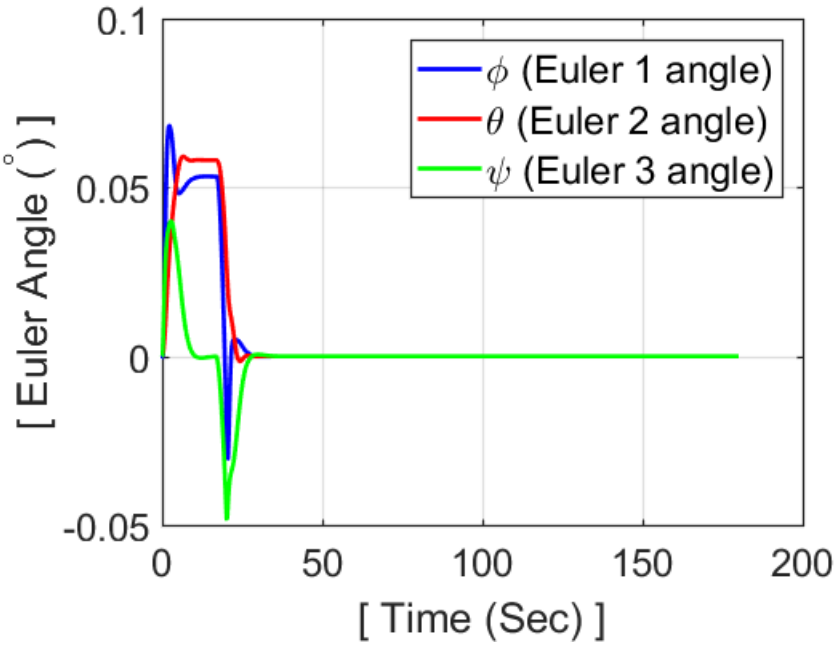

Figure 4.32: Euler Angle States in Landing

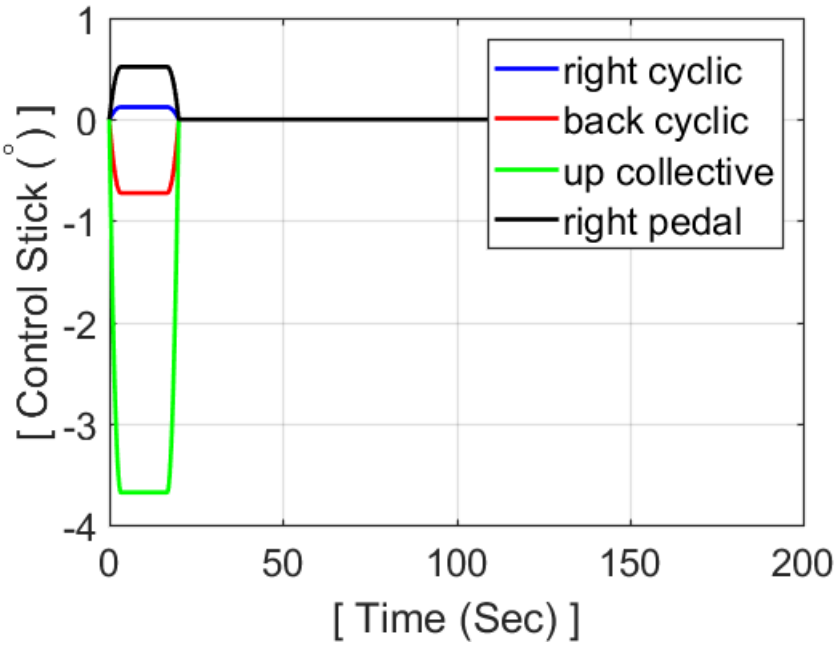

Figure 4.33: Relative Control Inputs in Landing

4.4 VISUALIZATION

Simulation results are visualized by using X-Plane 11 flight simulator software due to its excellent graphic quality and capability to implement a flight data recorder (FDR) file. It visualizes a UH-60 helicopter and a Navy ship realistically. Visualization through a FDR file is useful primarily in accident investigation and re-creation. In that case, it can be done by taking the data from the "black box" of an aircraft and put it in a format that X-Plane can load.

In this visualization, the simulation results are re-written in a FDR format. It visualizes the values of fuselage attitude (roll, pitch, yaw) at each time step by taking those values directly from the simulation results. However, the helicopter inertial position at each time step must be converted to latitude and longitude value. Based on this data, it visualizes the entire helicopter ship landing.

Figure 4.34: Visualized Ship Landing at initial position in Cockpit View

Figure 4.35: Visualized Ship Landing at flight deck in Outside View

Figure 4.36: Visualized Ship Landing under bad weather in Tail View

Figure 4.37: Visualized Ship Landing with night vision goggle (NVG) at night in Cockpit View

5. SUMMARY, CONCLUSIONS AND FUTURE WORK

In this chapter, what has been done in the research is briefly summarized. It also highlights the lessons learned from this work, and discusses the future work including practical applications.

5.1 SUMMARY

Developing a novel shipboard VTOL UAV autonomous landing system is composed of two main parts : 1. Modeling a high-fidelity UH-60 helicopter model as a representative aircraft, and 2. Implementing a combined vision-based navigation and LQR for set-point tracking control system.

For modeling a UH-60 helicopter, a coupled rotor-fuselage flight dynamic model has been developed that includes a linear dynamic inflow model, a rigid blade model with a flap and lag hinge, and an empennage model. The integrated model has been used to calculate trim equilibrium values. This model has been analyzed with flight test data at various flight conditions, which are forward flight, steady turn, and climb/descent.

After the model is validated, a linearized model is extracted based on a first-order Taylor series expansion of the nonlinear system about an equilibrium point. The extracted linearized model is used for a combined vision-based navigation and Linear Quadratic Regulator (LQR) for set-point tracking control system. To implement this method, it is required to have a rotatable camera attached to the nose of the helicopter, and a horizon bar on a ship. A vision-based algorithm is developed, which can detect a bar from an image, compute the relative distance and trajectory to fly. Based on the generated trajectory by using visual data, a helicopter flies autonomously along the trajectory. To make it fly realistically, gains for the controller have been selected carefully. Also, different linearized models are used to simulate flight conditions closely. A full autonomous flight is simulated from approach to landing on a ship and it is visualized by using X-Plane flight simulator program. It shows that the method, which is based on a real helicopter landing procedure, can be implemented effectively.

5.2 CONCLUSIONS

5.2.1 MATHEMATICAL MODELING OF A HELICOPTER

In this research, it targets to model a UH-60 helicopter by taking into account its several sub-dynamics. Based on the power curve analysis with the flight test data, it is noticed that it shows good validations at higher speeds, however, it under-predicts the power at low speeds. Some other previous comparison results by Ananth Sridharan [36] and Maria Ribera [37] show better results at low speeds range (below 30 knots). The key difference between their works and this study is the inflow model. They use free-vortex wake models to capture the behavior of inflows, but the Pitt-Peters linear inflow model is used in this research. Although it closely predicts power at lower speeds, it does not always guarantee better predictions in other trim values such as fuselage angles and control angles. For example, in spite of the fact that free-vortex wake model is more sophisticated, pitch angle predictions along the forward speed by using a UH-60 model with the Pitt-Peters linear inflow model has better agreement than the others. It is because the horizontal stabilator dynamic model has main influence on the fuselage pitch angle. Throughout this study, it convinces that a UH-60 model with the Pitt-Peters linear inflow model can also predict the behavior of the real helicopter, and yield valid results.

In addition, since helicopter responses are very coupled motions, each sectional dynamic model is also important to predict the helicopter responses. Also, the model selection can be different according to the particular point of interest.

5.2.2 DEVELOPING VISION-BASED ALGORITHM

In this research, it utilizes a single image to compute the relative distance. Usually, measuring an object size by using a camera is done by comparing images which are captured from different angles. However, in this particular case, the object length and the camera specifications are already known. Thus, the vision-based algorithm which calculates the relative distance from a single camera image is developed. Relative distance along the earth-fixed X-axis and Y-axis are computed based on data obtained from the image. Vertical distance is computed from a radar altimeter sensor.

Once the relative distance is identified, the desired trajectory to fly can be computed. It assumes no disturbances in the sensors, and the linear view mode actually makes the algorithm simple by correcting fisheye distortion automatically.

5.2.3 DESIGNING CONTROL SYSTEM

LQR controller is used for tracking a trajectory which is computed by vision-based algorithm. It regulates the error between the references and states. Choosing gains are based on trial and error due to the trade-off between transient responses and control efforts. In addition, As it requires the constructed matrix be invertible, the number of references have to be the same as the number of control inputs. Thus, this method can assign 4 references at the same time since the number of control inputs is 4. Even if it can give 4 references at once, assigning one reference at a time can give more satisfying results in practice. This is because helicopter responses are very coupled, so it is convenient to check control inputs and responses by assigning one reference at a time. By doing so, helicopter responses and control inputs can be more realistic.

5.3 FUTURE WORK

The limitations, assumptions, and approximations in the present research are possible areas for further study. Since the main goal of the present work is to propose a method which has not been done before, there are many things to enhance the quality.

First, modeling a UH-60 helicopter can be improved by using more flight test data and advanced inflow model. Flight test data can improve empennage models, fuselage drag estimation, and free-vortex wake model can improve predictions especially at lower air speed.

Second, vision-based navigation method needs to be enhanced in many ways since the current method consists of basic algorithm with no disturbance assumptions. Current RGB filter can be disturbed by strong lights which can affect the color of the bar, so it should be developed to operate in unfavorable situations. Although the method, which is to update the trajectory periodically, has been developed, simulations in this research are conducted without any disturbances. Thus, it does not simulate the flight conditions which require up-to-date image for positioning and guidance. In

order to ensure the robustness of the method, more simulations have to be conducted under various situations with disturbances.

Third, LQR control system is very useful to figure out gains based on prescribed weights for states and control inputs. However, it requires the trial and error process. It means if the results are not satisfying, weights are going to be adjusted based on guess. Hence, even if the results are very good, it is hard to say that the results are the best. If the ample simulation data are accumulated, It can be also developed to select the best gains based on previously investigated data other than guessing better weights.

Fourth, to improve fidelity of the simulations, additional considerations need to be applied such as wake caused by ship structure, ground effect caused by a ship deck, robust control architecture, and sensor noise. It allows to simulate ship landings more realistically.

Last but not least, the application of this method is not limited to a certain type of ship or aircraft. Thus, it can conduct flight experiments to demonstrate fesibility of this technique by using a small scale UAV and a moving platform. If a horizon bar is installed on a truck which is towing a platform and servos are added to simulate rolling and pitching ship motions, ship landing environments are successfully implemented. The experiment results will prove that this method allows an aircraft to land on a ship autonomously while maintaining high level of safety and accuracy. Consequently, it can be used as a primary landing method for VTOL UAV and it can also be used for manned VTOL aircraft to reduce pilot work load and enhance the level of safety in landing maneuver.

REFERENCES

[1] Johnson G, Waid J, Primm M, Aggerwal R, *"Ship attitude accuracy trade study for aircraft approach and landing operations,"* In: IEEE/ION Position location and navigation symposium (PLANS), pp. 783-790, 2012.

[2] Department of the Navy, *"Draft System Requirements Document for Joint Precision Approach and Landing System (JPALS) Increment 1,"* PMA2135-0100/R-5, Jun 1, 2007.

[3] Rife, J., Khanafseh, S., Pullen, S., De Lorenzo, D., Kim, U. S., et al., *"Navigation, interference suppression, and fault monitoring in the seabased joint precision approach and landing system,"* Proceedings of the IEEE, Vol. 96, pp. 1958-1975, Dec 2008.

[4] Charles C. Counselman, *"Method and system for determining position on a moving platform, such as a ship, using signals from GPS satellites,"* U.S. Patent 4 894 662, Jan. 16, 1990.

[5] Pervan, B., Chan, F. C., Gebre-Egziabher, D., Pullen, S., Enge, P., Colby, G., *"Performance Analysis of Carrier-Phase DGPS Navigation for Shipboard Landing of Aircraft,"* Navigation: Journal of the Institute of Navigation, Vol. 50, No. 3, pp. 181-191, 2003.

[6] Stephen J. Comstock, *"Development of a Low-Latency, High Data Rate, Differential GPS Relative Positioning System for UAV Formation Flight control,"* Master of Science Thesis, Air Force Institute of Technology, USA, 2006.

[7] M. Hardesty, S. Kennedy, S. Dixon, T. Berka, J. Graham, D. Caldwell, *"Development of navigation and automated flight control system solutions for maritime vtol uas operations,"* in AUVSI 2012, 2012

[8] Wulan, B., Jizhong, H., Yuanming, X., *"Vision-Based Unmanned Helicopter Ship Board Landing System,"* Second International Congress on Image and Signal Processing (CISP), IEEE Publ., Piscataway, NJ, pp. 1-5, 2009.

[9] C. S. Sharp, O. Shakernia, S. Sastry, *"A vision system for landing an unmanned aerial vehicle,"* Proc. IEEE Int. Conf. Robotics and Automation, pp. 1720-1728, 2001.

[10] J. L. Sanchez-Lopez, J. Pestana, S. Saripalli, P. Campoy, *"An Approach Toward Visual Autonomous Ship Board Landing of a VTOL UAV,"* Journal of Intelligent & Robotic System, vol. 74, no. 1-2, pp. 113-127, April 2014.

[11] Daewon Lee, Tyler Ryan, H Jin Kim, *"Autonomous landing of a VTOL UAV on a moving platform using image-based visual servoing,"* 2012 IEEE International Conference on Robotics and Automation, pp. 971-976, May 2012.

[12] G.Xu, Y.Zhang, S.Ji, Y.Cheng, Y.Tian, *"Research on computer vision-based for uav autonomous landing on a ship,"* Pattern Recogn.Lett., vol.30, no.6, pp.600-605, April 2009.

[13] B. Erginer, E. Altug, *"Modeling and pd control of a quadrotor vtol vehicle,"* in Intelligent Vehicles Symposium, IEEE, pp.894-899, 2007.

[14] K. Nho, R. K. Agarwal, *"Automatic landing system design using fuzzy logic,"* Journal of Guidance, Control, and Dynamics, vol. 23, no. 2, pp. 298-304, 2000.

[15] B. Prasad B, S. Pradeep, *"Automatic landing system design using feedback linearization method,"* in AIAA Infotech at Aerospace 2007 Conference and Exhibit, 2007.

[16] H. Voos, B. Nourghassemi, *"Nonlinear control of stabilized flight and landing for quadrotor uavs,"* in 7th Workshop on Advanced Control and Diagnosis, Zielona Gora, Poland, 2009.

[17] B. T. Burchett, *"Feedback linearization guidance for approach and landing of reusable launch vehicles,"* in American Control Conference, IEEE, pp. 2093-2097, 2005.

[18] D. Venkateswara Rao, T. H. Go, *"Automatic landing system design using sliding mode control,"* Aerospace Science and Technology, vol. 32, no. 1, pp. 180-187, 2014.

[19] T. Lee, Y. Kim, *"Nonlinear adaptive flight control using backstepping and neural networks controller,"* Journal of Guidance, Control, and Dynamics, vol. 24, no. 4, pp. 675-682, 2001.

[20] B. Ahmed, H. R. Pota, *"Backstepping-based landing control of a ruav using tether incorporating flapping correction dynamics,"* in American Control Conference, IEEE, pp. 2728-2733, 2008.

[21] B. Ahmed, H. R. Pota, M. Garratt, *"Flight control of a rotary wing uav using backstepping,"* International Journal of Robust and Nonlinear Control, vol. 20, no. 6, pp. 639-658, 2010.

[22] T. J. Koo, S. Sastry, *"Hybrid control of unmanned aerial vehicles for autonomous landing,"* in Proceedings of 2nd AIAA Unmanned Unlimited, AIAA, systems, technologies, and operations aerospace, land, and sea conference, 2003.

[23] S. Saripalli, J. F. Montgomery, G. S. Sukhatme, *"Visually guided landing of an unmanned aerial vehicle,"* Robotics and Automation, IEEE Transactions on, vol. 19, no. 3, pp. 371-380, 2003.

[24] S. Saripalli, G. S. Sukhatme, *"Landing on a moving target using an autonomous helicopter,"* in Field and Service Robotics. Springer, pp. 277-286, 2006.

[25] D. B. Barber, S. R. Griffiths, T. W. McLain, R. W. Beard, *"Autonomous landing of miniature aerial vehicles,"* Journal of Aerospace Computing, Information, and Communication, vol. 4, no. 5, pp. 770-784, 2007.

[26] B. Herisse, T. Hamel, R. Mahony, F. X. Russotto, *"Landing a vtol unmanned aerial vehicle on a moving platform using optical flow,"* Robotics, IEEE Transactions on, vol. 28, no. 1, pp. 77-89, 2012.

[27] T. Merz, S. Duranti, G. Conte, *"Autonomous landing of an unmanned helicopter based on vision and inertial sensing,"* in Experimental Robotics IX. Springer, pp. 343-352, 2006.

[28] G. Xu, Y. Zhang, S. Ji, Y. Cheng, Y. Tian, *"Research on computer vision-based for uav autonomous landing on a ship,"* Pattern Recognition Letters, vol. 30, no. 6, pp. 600-605, 2009.

[29] X. Pan, D.q. Ma, L.l. Jin, Z.s. Jiang, *"Vision-based approach angle and height estimation for uav landing,"* in Image and Signal Processing, IEEE, vol. 3., pp.801-805, 2008.

[30] M. Sereewattana, M. Ruchanurucks, S. Siddhichai, *"Depth estimation of markers for UAV automatic landing control using stereo vision with a single camera,"* Int. Conf. Information and Communication Technology for Embedded System., Jan 2014.

[31] T. Daquan, Z. Hongyue, *"Vision based navigation algorithm for autonomic landing of uav without heading & attitude sensors,"* in Signal Image Technologies and Internet-Based System, 2007. SITIS'07. Third International IEEE Conference on. IEEE, pp. 972-978, 2007.

[32] A. Miller, M. Shah, D. Harper, *"Landing a uav on a runway using image registration,"* in Robotics and Automation, 2008. ICRA 2008. IEEE International Conference on. IEEE, pp. 182âĂŞ187, 2008.

[33] Alvika Gautam, PB Sujit, Srikanth Saripalli, *"A survey of autonomous landing techniques for uavs,"* Unmanned Aircraft Systems (ICUAS) 2014 International Conference on, pp. 1210-1218, 2014.

[34] F. J. Bailey, *"A Simplified Theoretical Method of Determining the Characteristics of a Lifting Rotor in Forward Flight,"* Tech. Rep. 716, NACA, 1941.

[35] Kevin W. Williams, *"A Summary of Unmanned Aircraft Accident/Incident Data: Human Factors Implications,"* FAA Civil Aerospace Medical Institute, Oklahoma City, 2004. http://www.hf.faa.gov/docs/508/docs/uavFY04Mishaprpt.pdf. Accessed : Jan 30, 2005.

[36] Maria Ribera, *"Helicopter Flight Dynamics Simulation With a Time-accurate Free-vortex Wake Model,"* Doctor of Philosophy Dissertation, University of Maryland, USA, 2007.

[37] Ananth Sridharan, *"Simulation Modeling of Fight Dynamics, Control and Trajectory Optimization of Rotorcraft Towing Submerged Loads,"* Doctor of Philosophy Dissertation, University of Maryland, USA, 2014.

[38] Colin Rhys Theodore, *"Helicopter Flight Dynamics Simulation with Refined Aerodynamic Modeling,"* Doctor of Philosophy Dissertation, University of Maryland, USA, 2000.

[39] Moble Benedict, *"Fundamental Understanding of The Cycloidal-Rotor Concept For Micro Air Vehicle Applications,"* Doctor of Philosophy Dissertation, University of Maryland, USA, 2010.

[40] W. Johnson, *"Rotorcraft Aerodynamics Models for a Comprehensive Analysis,"* in 54th Annual National Forum of the American Helicopter Society, AHS, May 1998.

[41] R. Sopher, D. W. Hallock, *"Time-History Analysis for Rotorcraft Dynamics Based on a Component Approach,"* Journal of the American Helicopter Society, vol. 31, no. 1, 1986.

[42] J. J. Howlett, *"UH-60A Black Hawk Engineering Simulation Program: Volume I - Mathematical Model,"* Tech. Rep. CR 166309, NASA, Dec 1981.

[43] J. G. Leishman, *UH-60A Black Hawk Engineering Simulation Program: Volume I - Mathematical Model.* Cambridge University Press, 2002.

[44] D. M. Pitt, D. A. Peters, *"Theoretical Prediction of Dynamic Inflow Derivatives,"* Vertica, vol. 5, pp. 21-34, 1987.

[45] C. He, D. A. Peters, *"Comparison of Measured Induced Velocities with Results from a Closed-form Finite State Wake Model in Forward Flight,"* in 45th Annual National Forum of the American Helicopter Society, AHS, May 1989.

[46] F. Kim, *"Formulation and Validation of High-Order Mathematical Models of Helicopter Flight Dynamics,"* Doctor of Philosophy Dissertation, University of Maryland, USA, 1991.

[47] W. Johnson, *Helicopter Theory.* Dover Books on Aeronautical Engineering Series, Dover Publications, 1994.

[48] R. T. N. Chen, *"A Survey of Nonuniform Inflow Models for Rotorcraft Flight Dynamics and Control Applications,"* Tech. Rep. Technical Memorandum 102219, NASA, November 1989.

[49] F. J. Bailey, *"A Simplified Theoretical Method of Determining the Characteristics of a Lifting Rotor in Forward Flight,"* Tech. Rep. 716, NACA, 1941.

[50] R. Celi, *"Implementation of Rotary-Wing Aeromechanical Problems Using Differential-Algebraic Equation Solvers,"* Journal of the American Helicopter Society, vol. 45, no. 4, pp. 253-262, Oct 2000.

[51] R. Celi, *"Helicopter Rotor Dynamics in Coordinated Turns,"* Journal of the American Helicopter Society, vol. 36, no. 4, pp. 39-47, Oct 1991.

[52] D. E. Kirk, *Optimal Control Theory : An Introduction.* Prentice-Hall, USA, 1970.

[53] H. Yeo, W. G. Bousman, W. Johnson, *"Performance Analysis of a Utility Helicopter with Standard and Advanced Rotors,"* Journal of the American Helicopter Society, vol. 49, no. 3, pp. 250-270, 2004.

[54] G. Franklin, J. Powell, A. Emami-Naeini, *Feedback Control of Dynamic Systems.* Boston, MA: Addison-Wesley, 2nd ed., 1991.

APPENDIX A

UH-60 HELICOPTER CONFIGURATION

Main Rotor	
Number of blades	4
Radius R, ft	26.83
Blade chord c, ft	1.75
Rotational speed, rad/sec	27.0
Tip speed, ft/sec	724.41
Longitudinal mast tilt, deg	-3.0
Airfoil section	SC 1095
First airfoil section, ft	5.08
Blade precone, deg	0.0
Linear blade twist, deg	-18.0
Solidity	0.083
Lock number	5.11
Control phase shift	-9.7
Tail Rotor	
Number of blades	4
Radius, ft	5.5
Blade chord, ft	0.81
Rotational speed, rad/sec	124.62
Tip speed, ft/sec	685.41
Rotor shaft cant angle, deg	20.0
Fuselage	
Gross weight, lbs	16000.00
Pitch inertia I_{yy}, lbs$\cdot ft^2$	38512.0
Roll inertia I_{xx}, lbs$\cdot ft^2$	4659.0
Yaw inertia I_{zz}, lbs$\cdot ft^2$	36796.0
I_{xz}, lbs$\cdot ft^2$	1882.0
Horizontal tail surface area, ft^2	45.00

Table A.1: Main Parameter of the UH-60 helicopter configuration